Dissertations, Theses, and Masters Projects   Theses, Dissertations, & Master Projects

2004

Ultraviolet sources for advanced applications in the vacuum UV and near UV

Sheng Peng

College of William & Mary - Arts & Sciences

Follow this and additional works at: https://scholarworks.wm.edu/etd

Part of the Atomic, Molecular and Optical Physics Commons, Nuclear Commons, and the Plasma and Beam Physics Commons

NOTE TO USERS

This reproduction is the best copy available.

UMI®

ULTRAVIOLET SOURCES FOR ADVANCED

APPLICATIONS IN THE VACUUM UV AND NEAR UV

A Dissertation

Presented to

The Faculty of the Department of Physics

The College of William & Mary in Virginia

In Partial Fulfillment

Of the Requirements for the Degree of

Doctor of Philosophy

by
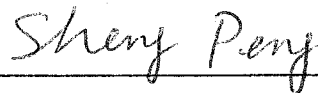
Sheng Peng

2004

APPROVAL SHEET

This dissertation is submitted in partial fulfillment of

the requirements for the degree of

Doctor of Philosophy

_____
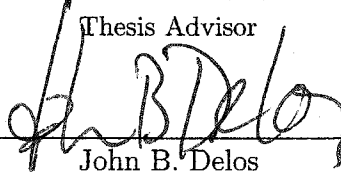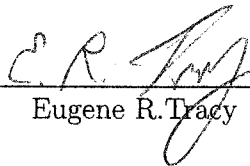
Sheng Peng

Approved, December 2004

_____

Dennis M. Manos

Thesis Advisor

_____

John B. Delos

_____

Eugene R. Tracy

_____

Robert E. Welsh

_____

Mark K. Hinders

Department of Applied Science

ii

To my parents...

Table of Contents

ACKNOWLEDGEMENTS

I would like to thank my parents, whom I am indebted for. They have given me everything I need for living, learning, and working. I dedicate this work to my mother, Yuluan Li, and my father, Feng Peng. If I should be honored for any piece of this work, I want to pass this honor to them.

My most special thanks go to Professor Dennis M. Manos. As my advisor, he led me all the way through my PhD study. He provides me the opportunity to learn, to ask and to prospect. What I have learned from him are not only the experimental skills and keen sensitivity for new ideas, but more valuable are the attitudes to my life. It is my honor to work with him.

Professor John B. Delos served as an unofficial co-mentor on this work; his advice and efforts were essential to my success in developing the analytical model. I am indebted for the valuable time Professor Delos spent with me, which was fruitful and full of fun. I wish to thank my other committee members, Professor Eugene R. Tracy, Professor Mark Hinders and Professor Robert Welsh. They supervised my progress and gave me valuable suggestions.

Like Professor Delos, in addition to being a good friend and valued collaborator, Dr. Joseph D. Ametepe (Hollins University) has been an unofficial member of my committee. He has collaborated with us on the important work of KrI and the work on E. coli. I would like to thank him for his generous help and for reading and correcting my dissertation manuscripts. I would like to thank Dr. John C. Poutsma from Chemistry Department for the stimulating discussions about Gaussian simulation. I would also like to express my appreciations to Dr. Lars D. Ludeking (Mission Research Corporation) for giving me constant support on PIC simulations in MAGIC and to Dr. Erik Schoeffel (McPherson, Inc.) for helping me setup our optical characterization system. My thanks also go to Richard Proper from Applied Science department who helped me build the vent system to handle toxic gases.

I am also grateful for our Applied Research Center business manager Kathee Card, program director Bernadette A. Kulas and research specialist Amy Wilkerson who always stand on my side and offer me their supports on any favor I asked. It has always been a pleasure to work with Mingyao Zhu, Dr. Jianjun Wang, Nimel Theodore, Zhengmao Zhu and Hui Tian. Discussions with Dr. Wei Yang, Haijian Chen, Xin Zhao, and many other friends have always been useful.

All of my successes were based on the support of my family. I would like to thank my wonderful wife, Ping Tang, and my daughter, Eleanor. They are the driving force of my life.

List of Tables

ix

List of Figures

x

xi

xiii

ABSTRACT

This dissertation documents a systematic study consisting of experimental investigations and theoretical analyses of intense ultraviolet sources in VUV and near-UV. Some engineering issues regarding two prototypes of electrodeless lamps using rf and microwave are discussed.

Various excimers that produce intense UV light are investigated, including: (1) A benchmark Xe_2 excimer which has been proven to be very efficient in our novel rf capacitively coupled discharge lamp; (2) A rarely studied excimer, KrI, which suffers from predissociation and was reported to be very weak or invisible by most of other studies; (3) XeI excimer whose emission dominates around 253 nm and is promising as a mercury-free lamp for antibacterial applications. In the above studies, discharge temperatures are estimated from the emission band width. An elaborate kinetic model is developed for KrI to account for the KrI^* and I_2^* intensities as a function of pressure. It was found that Kr_2^* plays the rule for energy transfer instead of Kr^* in the pressure of interest. The electromagnetic wave interaction with charge particles is studied in our 2D and 3D EM-PIC simulations for both the rf and microwave lamps. Important plasma parameters, such as the electron density and temperature are obtained for various pressures. The electron energy distribution function that is important to account for excimer excitation is obtained.

We also performed a high-level ab initio calculation in Gaussian to produce the ground state potential curve for KrI, which agrees with previous scattering experiments and is necessary for predicting spectral emissions. As a systematic study to account for the KrI emission spectra at high pressure, we use a semiclassical model to account for emissions between a bound excited state and an unbound ground state. An explicit expression is obtained to represent the observed spectral intensity. Important molecular constants are obtained for KrI and compared with previous results.

ULTRAVIOLET SOURCES FOR ADVANCED APPLICATIONS IN THE VACUUM UV AND NEAR UV

Chapter 1

Introduction

1.1 Outline

The outline for this dissertation (see Fig. 1.1) is as follows:

Chapter 1 is an introduction of this work. This includes a historic review of light sources, their applications, and motivations of this work.

Chapter 2 presents a background to the fundamental physics involved in lamp development. This includes plasma physics, gas flow, and plasma excitation of gases. I present a brief review of excimer physics and diatomic molecular spectroscopy. There is also a description of lamp design issues.

Chapter 3 describes our experimental apparatus, concentrating on our novel rf and microwave lamps, discussing the vacuum system, optical characterization system, and data acquisition. This chapter also briefly describes some of the engineering considerations of the lamp.

Chapter 4 presents the results for high pressure gases excited in the rf lamp. I present benchmarking studies of Xe (Xe_2), for which extensive prior microwave re-

2

Level of View

Chapter 1
Introduction

history, applications, and motivation

Fundamentals

Chapter 2
Excimer lamp basis

Plasma basis

Methods to excite plasma

Review of excimer lamps

Microwave lamp

Engineering

Rf lamp

Chapter 3
Experimental setup

Vacuum system

Optical characterization

Data acquisition

Chapter 4
Results

Xe_2^*

KrI^*

XeI^*

Classical Physics

Chapter 5
MAGIC simulation

Quantum Mechanics

Chapter 6
Gaussian simulation

Semiclassical

Chapter 7
Semiclassical line shape simulation

Chapter 8
Summary

Figure 1.1: Dissertation content flowchart

sults exist, followed by a detailed study of KrI, a relatively unstudied, and interesting, excimer species. The pressure dependence of emission intensity for this species is described and modeled. Spectral emission from other rare gas halogen (Rg-X) mixtures such as XeI are presented. The Lamp efficiency is described.

Chapter 5 discusses our use of a large-scale particle-in-cell code known as "MAGIC" to simulate the plasma physics of the lamp in order to estimate the parameters governing the electron impact dynamics and governing the light-producing processes described in the earlier chapters. These parameters are also necessary as part of our modeling of the spectra which follows in later chapters. The computed electromagnetic field distribution for both rf and microwave lamps is described and compared. The interactions of charged particles in these fields are discussed in order to account in part for the observed spectral output differences we observe.

Chapter 6 discusses the problems arising in conventional simulation of spectral emission for KrI, emphasizing that potential curves are not available from which to extract the necessary parameters to simulate the spectrum using high-order numerical methods. In this chapter we present a preliminary Density Functional Theory calculation on the KrI system using an ab initio simulation program known as "Gaussian". The output of this calculation gives estimates for the electron densities associated with the molecular orbitals resulting from bonding in the excimer. The results also include a good estimate for the potential curve of lower state of KrI, which agrees with the result from atom scattering experiment.

Chapter 7 presents a discussion of spectral simulation. We discuss numerical sim-

ulation and reiterate the difficulties specific to computational modeling of KrI. These difficulties in conventional simulation have led us to develop a simple semiclassical approach similar to the Stueckelberg's model from which we have derived an analytical expression for the KrI excimer spectral line shape. This calculation is compared with our experimental data in an effort to assess the necessary details of the interatomic potentials consistent with the observed spectra.

Chapter 8 summarizes this project and presents some future work including lamp characterization, modeling and antibacterial applications.

1.2 History

Light is the most common form of electromagnetic radiation (EMR) and the only form that humans can routinely sense. Archeologist have uncovered evidence that lamps were in use at least as early as 70,000 BC [1]. These ancient lamps consisted of hollow rocks, shells, or other natural objects filled with moss, or other porous material that was soaked with animal fat and ignited. These kinds of light sources evolved into oil lanterns and candles, and have been in continuous use up to modern times. The evolution of lamps, linked closely to the evolution of human society, had the same set of drivers for millennia. These were to seek improvements leading to brighter sources, lower maintenance, lower operating costs, and higher reliability. Thus the main improvements were to provide for the use of alternate fuels and adjustable burn rates. The largest leaps forward improvements came with the introduction of gas,

as opposed, to liquid fueled, lamps (1784), followed by electrically powered lamps, which began when Sir Humphrey Davy of England invented the first electric carbon arc lamp in 1801 [2]. Around 1879, Thomas Edison invented the first commercially successful electric incandescent lamp.

These three styles of lamp, gas fired, incandescent, and arc were augmented by plasma-driven lamps in the form of fluorescent tubes, introduced in 1856 by Michael Faraday (England) [3]. Throughout the 20th century enormous progress occurred in improving brightness, reliability, and cost in all of the electrically powered styles of lamps. Advanced work on gas mixtures for lamps appeared relatively early, though the use of halogens in lamps did not become widespread until 1960, when brighter halogen-filled incandescent lamps were introduced. Halogen gas slows the filament evaporation rate allowing it to be operated at higher temperatures and for longer periods [4]. Improvements to plasma-driven lamps also occurred rapidly over this same period, driven mainly by the need for reliable, low-maintenance sources for industrial and home lighting. In 1991, Philips, developed a light bulb that uses magnetic induction to excite a gas to emit light. There are no parts to wear out in this design, so the expected lifetime for a bulb is 60,000 hours [5].

Light sources were prevalently used as manufacturing tools in industry after the invention of the laser, which can be dated to 1958 with the publication of the scientific paper, by Arthur L. Schawlow and Charles H. Townes [6]. That paper launched a new scientific field and opened the door to multibillion-dollar optics, opto-electronics, and photonic manufacturing industries.

During the years 1975 to 1979 many scientists at various institutions worked in the initial development of a family of gas lasers/lamps known as the "excimer", which stands for a contraction of "Excited Dimer". These important gas molecules are rare gas and rare gas halides. Because of their short wavelengths and reliable performance, these excimer sources have been developed into powerful manufacturing tools.

1.3 Background

Light is only a very small band within the electromagnetic spectrum. Visible light is the spectrum band (400 nm - 760 nm) to which the human retina is sensitive. On the short wavelength side of this spectrum is the ultraviolet (UV) band.

The UV band is divided into extreme UV (EUV 10 nm - 100 nm), vacuum UV (VUV 100 nm - 200 nm), UVC (200 nm - 280 nm), UVB (280 nm - 315 nm) and UVA (315 nm - 400 nm). UVA radiation elicits a tanning response of skin. It is also thought to contribute to increased susceptibility to skin carcinogenesis. It may also produce hyperkeratosis. UVB radiation occurs at a shorter wavelength than UVA and thus more energetic. It produces erythema, sunburn, and delayed tanning. In some cases, UVB radiation can produce more serious effects such as cutaneous carcinoma and non-melanoma skin cancer. This radiation has sufficient energy to do rapid photochemistry on heteroatomic organic chemicals, including biochemicals, so it is used extensively for sterilization and germicidal applications. UVC radiation from the sun is completely absorbed by the ozone layer so sunlight is not used for

process applications in this region. VUV radiation has wavelengths shorter than 200 nm and cannot transmit in air because of strong absorption of oxygen and water. Nevertheless its very energetic nature makes it useful for various process applications, some of which will be discussed below. EUV radiation has the shortest wavelength and highest energy in UV region. The optical lithograph technology using EUV will will open a new chapter in semiconductor technology to produce next generation chips. Commercial applications for UV technology include commodity chemicals, processes, public service utilities, and medical and pharmaceutical treatments. Thus, research on this subject is aggressively pursued all over the world and artificial sources are supplied by numerous UV light companies.

1.4 Applications

Because UV photons are strongly absorbed by most materials, photon-induced processing has become an important technology in industries such as automobile manufacturing, textiles, water and food treatment, electronics, chemicals, and medical treatment. Fig. 1.2 summarizes the range of excimer (Rg and Rg-X) wavelengths available and compares them with the bond dissociation energies of various common molecules. Excimer lamps or lasers emitting photons at these wavelengths can excite and dissociate many types of materials.

In recent years, UV curing has emerged as perhaps the most exciting and versatile material technology. This process refers to the use of UV radiation energy to "dry
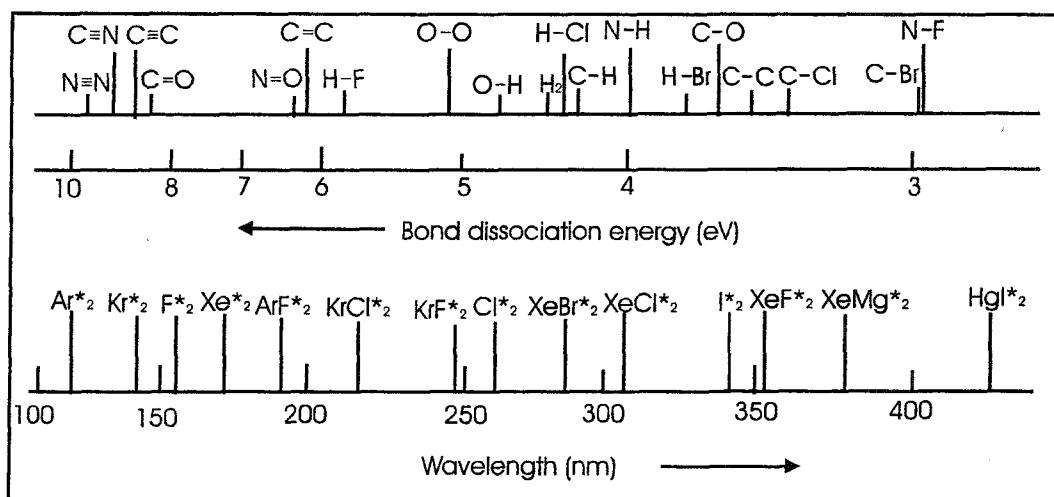
Figure 1.2: Spread of wavelength available with excimer sources, compared with a selection of bond-strengths of common molecules

out" and harden a coating material or adhesive. UV curing mainly works by activating the polymerization of monomeric species which form the basis of special paints, vanishes, adhesives and sealing or casting compounds. Compared to traditional solvent evaporation, thermal curing, or air curing, polymerization by UV curing is completed almost instantaneously on exposure to the appropriate wavelength of light, usually in the wavelength region from 200 nm to 400 nm. This permits a number of medical, dental, and industrial applications where critical material or parts layout is required prior to solidifying a configuration. This form of curing also allows extremely efficient use of external energy, so long as the conversion from electrical to photon energy is also efficient. Different UV light sources are employed depending upon the type of material to be processed. The high energy UV radiation causes chemical bonds to break so that film polymerization can start. Applicable materials include adhesives,

resins, coatings and inks.

UVC is the most effective part of the UV spectrum for germicidal applications. UVC deactivates the DNA of bacteria, viruses and destroys their ability to multiply. Specifically, UVC light causes damage to the nucleic acid of microorganisms by forming covalent bonds between certain adjacent bases in the DNA and prevents the DNA from being unzipped during replication. This process is a non-chemical approach to disinfection, which is simple, inexpensive, and environmentally benign. UVC in the range from 250 nm to 260 nm can be used for treating drinking water, processing food, sterilizing hospital equipment, disinfecting surfaces, and for many other germicidal applications.

UV light has also become critically important for increasingly small feature production in integrated circuit manufacturing. Moore's Law [7] predicted that the number of components on the most complex chips would double every two years. Higher storage capacity of memory devices (DRAMs) and ever-faster clock speeds of microprocessors demand such small circuit features, which must be transferred in the lithography steps. Better feature resolution can be achieved by a variety of techniques, but the most direct means is to use shorter wavelength (< 200 nm) radiation in deep UV lithography. Currently we are advancing into an age with sub-100 nm technologies (see Table 1.1), so lithography technologies with UV sources producing light with wavelengths of 193nm, and below, are in demand (see Fig. 1.3).

Polymeric materials have many applications, therefore there is the need to tailor the surfaces of polymers to provide more flexibility in their uses. UV treatments
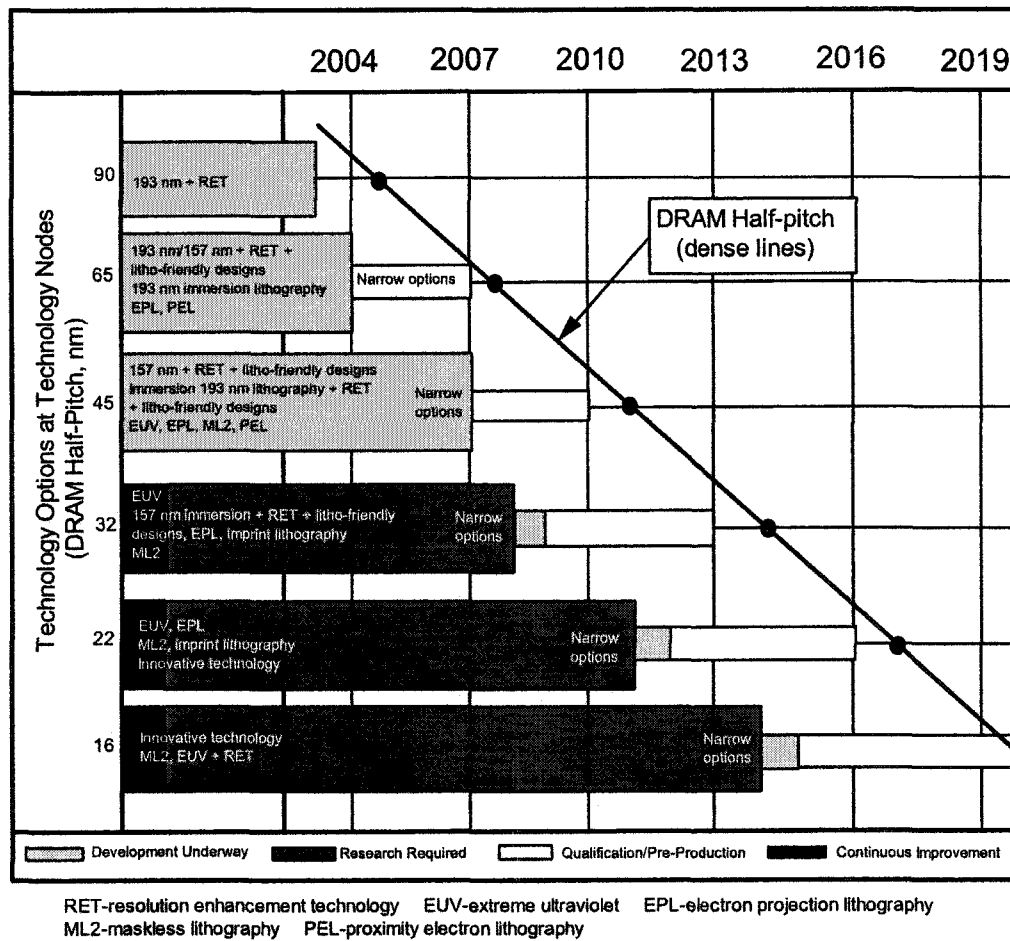
Figure 1.3: Potential Solutions of Lithography Exposure Tools (ITRS 2003)

YEAR OF PRODUCTION	1995	1998	2000	2002	2003	2004	2006	2007	2009	2010	2012	2013	2015	2016	2018
FEATURE WIDTH (nm)	360	255	180	127	101	90	71	64	51	45	36	32	25	23	18

Table 1.1: VLSI trend numbers (ITRS 2003)

offer an unprecedented spectrum of possible surface modifications to enhance polymers, ranging from simple topographical changes to creation of surface chemistries and coatings that are different from the bulk polymer. Photon treatments are fast, environmentally friendly, and economical in their use of materials.

UV (so-called "black light") fluorescent inspection has been employed in quality control , forensics, and contamination control. Many, or even most, large organic materials, especially biochemicals, will glow when illuminated with UV light [8, 9].

1.5 KrI as an Excimer

The rare gas monohalides (RgX) have been a group of interesting diatomic molecules since lasing [10, 11] was achieved in the seventies of the last century. Both experimental and theoretical efforts have been devoted to studying such excimers. As a result, spontaneous emission spectra have been recorded for many of these excimers. [12, 13, 14, 15, 16]

Although many of the RgX systems have been generally well studied, experimental and theoretical information on the interaction between iodine and the rare gas atoms is still quite limited. This is especially true for KrI. Previous studies [17, 18] indicate that KrI has two observable emission bands at 191 nm ($B^2\Sigma_{1/2} \rightarrow X^2\Sigma_{1/2}$) and

225 nm ($\mathbf{B}^2\Sigma_{1/2} \rightarrow \mathbf{A}^2\Pi_{1/2}$). This system provides an opportunity to investigate the fundamental physics of interactions between iodine and krypton, both relatively heavy atoms and therefore presenting interesting and difficult quantum mechanical issues. This system also provides a possible avenue to develop a new and interesting range of VUV bands available in a novel, low-maintenance light source, which is much safer than fluorine based sources which are presently the dominant sources in this wavelength range.

Previous spectroscopic studies of KrI have been mainly confined to the regime of low pressures (<100 torr) [17, 19, 20]. At low pressures, the inert gas halides suffer very few, if any, collisions during the excited state lifetime, which is of the order of 10-50 ns. In this work, we provide a detailed study of KrI at high pressure (>100 torr). In the high pressure regime, collisions alter the nascent distribution of internal states, yielding completely different spectra, which are generally of narrower line width than their low-pressure analogs. We will have more to say on the physics of this process later, but narrow line-width, the limit of which is monochromaticity, is of great value in high-value applications like lithography.

In previous work, KrI emissions were entirely uncalibrated as to their intensity relative to the electrical inputs. In addition, from those studies, when compared to nearby atomic iodine lines, at 206 nm, we can infer that the KrI emissions were reported to be very weak [17, 19]. This work is novel in presenting a strong source that has been quantitatively calibrated.

For these studies, our group designed two prototypes of excimer lamps. These

electrodeless lamps offer high-power, large area photons from deep UV to infrared, and lamp efficiency was carefully considered. They not only can be utilized to study weak emissions and lasing, but also provide new and interesting techniques to excite plasmas whose characteristic parameters may be optimized to enhance emission from these systems.

The current literature does not provide a theoretical study of the KrI spectrum to disclose the fundamental physics involved in the production of these photon emissions. Although spectroscopy is a mature subject, theoretical methods to predict emission has not been well developed for all excimers, especially for such heavy molecules like KrI, which has the angular momentum coupling lying intermediate between Hund's case (b) and case (c), and probably much closer to case (c). This dissertation will provide a simple semiclassical model wherein I derive an explicit expression for the excimer spectral line shape. The model and calculations are applied to KrI* emission studies and this model is universally applicable to systems where the upper excited electronic state is only weakly bound (binding energy less than an eV) and the lower state is unbound, or nearly so. Results of the analysis include estimates of upper state vibrational frequencies and shapes of the lower state potential curves in Franck-Condon region.

Chapter 2

Plasma Fundamentals

2.1 Plasma

The name "plasma" was introduced into physics in 1929 by Langmuir [21] to describe a conducting gas. Because of their distinctive physical properties (from solids, liquids, and gases), the plasma state is sometimes referred to as the fourth state of matter. When an atom or molecule in a gas absorbs sufficient energy, charged particles (electrons, positive and/or negative ions) are formed by various ionization processes. These have been thoroughly described in a number of excellent texts [22, 23, 24, 25]; for the purposes of this brief review we draw heavily on the text of Lieberman and Lichtenberg [24] and an earlier monograph by von Engel [23]. When the gas becomes sufficiently highly ionized, it becomes conductive. The standard model of a simple glow discharge (von Engel) is to consider a gas-filled cylindrical column with electrodes at either side onto which external voltages are applied to create an electric (E) field. If the gas is not ionized, the E-field is uniform in the gap. As the degree of ionization increases, the column undergoes a complex set of changes which lead

15

to a set of well-described regimes in which the longitudinal structure demonstrates various dark and light bands of emission associated with electron impact processes whose energy derives from a rearrangement of the electric field governed by the mobility of the charged species in the column. Most elementary textbooks concentrate on weakly-ionized, low-pressure plasma in electropositive gases, such as inert gases or hydrogen, where electron impact processes lead to an equal local density of positive charges, as ions, and negative charges, as electrons in a situation therefore called "quasi-neutral plasma". Some texts erroneously list quasi-neutrality as a hallmark of plasmas and a necessary attribute for their existence. This is not the case, single species, or "non-neutral" plasmas exist and are the subject of interesting studies [26]. The true hallmark of plasma, and a necessary condition for its existence is the presence of collective effects that reach over distance that are long compared to the Debye length, which we describe in some detail below.

Below, we will briefly sketch the evolutionary behavior of the simplest form of DC glow discharge, We will not give a detailed review of the entire, well-known evolution from the early stages, known as the "Townsend regime", to the terminal stages associated with a filamentary arc discharge at higher densities or neutral pressures. However, later in this dissertation, we will develop in detail the equations for the so-called "Debye sheath", and its concomitant shielding behavior, which are necessary to appreciate the large differences that occur in the behavior of the microwave lamp and the rf lamp systems. The relevant (small) length parameter associated with discharges, called the Debye length, is the most fundamental aspect of quasi-neutral

plasmas. When the working gas is such that the one carrier, such as electrons in an electropositive gas, has a much greater mobility than the ions, the Debye length is a function of the electron density and electron temperature. In some cases, such as halogen gases, the mobility difference may be negligible. It represents the distance over which the charged species will rearrange to cancel the local electric field in order to minimize the energy density of the system. This attempt at cancellation gives rise to numerous phenomena that dictate the static structure and the dynamic response of the system to various forms of external fields.

By some estimates, 99% of the observable universe is in the plasma state. But apart from lightning, and particle-driven phenomena in the upper atmosphere, there is little naturally-occuring plasma on Earth. Persistent high temperatures are not necessary for a plasma to exist. A plasma can exist at relatively low temperatures provided there is a source of energy to ionize the gas and means to suppress the rate of keeping recombination of the charged species. This is easily done in laboratory plasmas such as our lamps.

Table 2.1 gives some examples of real plasmas in laboratory and nature, where N_e and N are the number densities of electrons and neutrals respectively, and T_e and T are the temperatures (or the average energy) of electrons and the neutral gas.

T_e is not often equal to T. When T_e and T are identical, the plasma is said to be in complete thermal equilibrium. More commonly, a form of "quasi-equilibrium" wherein an approximately Boltzmann distribution of velocities attains for each species, but the parameters of these distributions are unequal, as seen in the table above. The

Type of plasma	$N_e(cm^{-3})$	$N(cm^{-3})$	$T_e(K)$	$T(K)$
Sun's photosphere	10^{13}	10^{17}	6000	6000
ionosphere (at 60km, daytime)	10^5	10^{13}	250	250
He-Ne laser	3×10^{11}	2×10^{16}	3×10^4	400
Argon laser	10^{13}	10^{14}	10^5	10^3

Table 2.1: Characteristic parameters of some plasmas

notion of quasi-equilibrium also extends to the necessity that time derivatives of the distributions are zero, so, for example, the rate of charge production by ionization must equal the rate of losses by all processes, including diffusion, convection, and internal recombination.

2.2 Sheaths

Plasmas are joined to a boundary surface across thin positively charged layers called sheaths. The bulk plasma region is quasi-neutral, and both instantaneous and time-averaged fields are low. In the sheath region, high fields lead to dynamics that are described by various ion space charge sheath laws, including low-voltage sheaths and various high-voltage sheath models, such as collisionless and collisional Child laws. Here, and in Sec. 2.3, 2.4 to follows, we present standard treatments of various important attributes of plasmas that can be found in texts like Lieberman and Lichtenberg [24].

In thermal equilibrium, the Boltzmann's relation can be derived for the density of electrons in a plasma under the action of a spatially varying potential. In the absence of electron drift, the inertial, magnetic, and frictional forces are zero, and the force
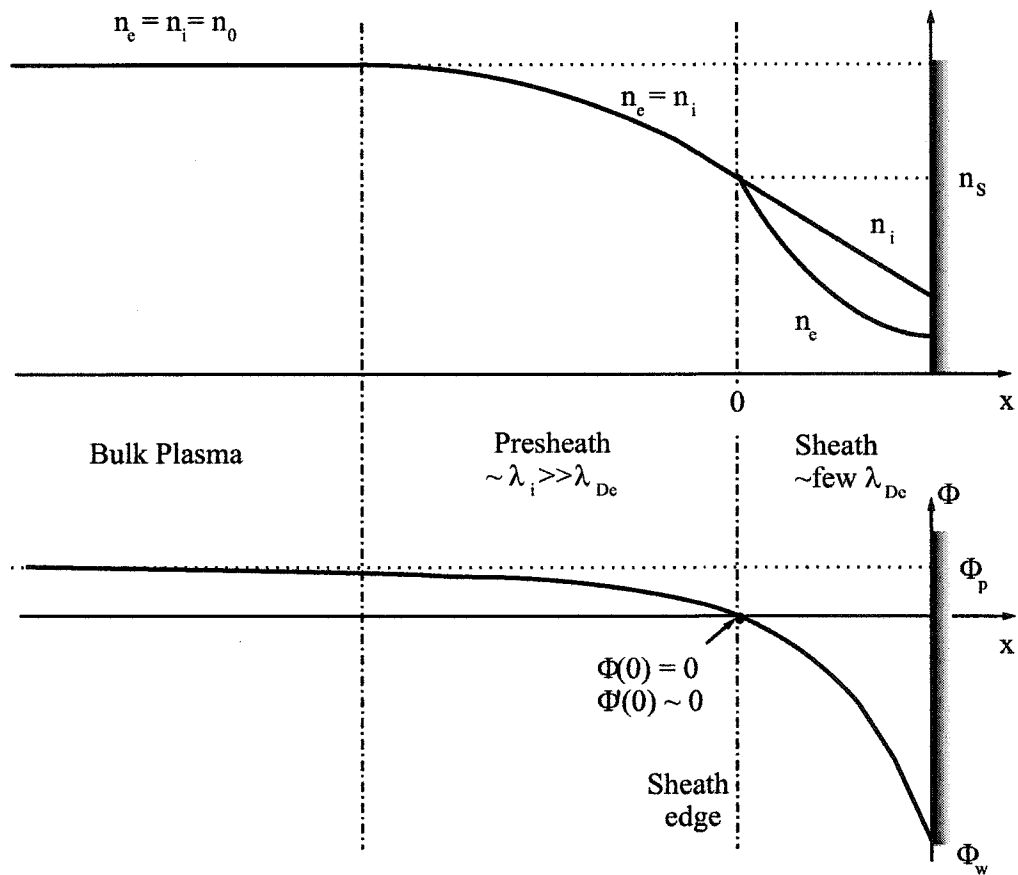
Figure 2.1: Qualitative behavior of sheath and presheath in contact with a wall

balance equation is,

$$en_e\mathbf{E} + \nabla p_e = 0 \tag{2.1}$$

Setting $\mathbf{E} = -\nabla\Phi$ and assuming $p_e = n_e k T_e$, Eq. (2.1) becomes

$$-en_e\nabla\Phi + kT_e\nabla n_e = 0$$

Integrating, we have

$$n_e(r) = n_0 e^{e\Phi(r)/kT_e}$$

or

$$n_e = n_0 e^{\Phi/T_e} \tag{2.2}$$

when we use more convenient units where T_e is expressed in volts, as is Φ.

A similar relation can be obtained for positive ions in the thermal equilibrium at T_i.

$$n_i = n_0 e^{-\Phi/T_i} \tag{2.3}$$

The characteristic length scale in a plasma is called Debye length. It is described to be the length over which the plasma electrons screen an applied potential. Low-voltage sheaths are typically a few Debye lengths wide. To determine the Debye length, let us introduce a sheet of negative charge into an infinitely extended plasma having equilibrium densities $n_e = n_i = n_0$. For simplicity, we assume immobile ions,

through out the plasma, such that $n_i = n_0$. We use Poisson's equation to determine the potential and density variation in one dimension.

$$\frac{d^2\Phi}{dx^2} = -\frac{e}{\epsilon_0}(n_i - n_e) \qquad (2.4)$$

Using the Boltzmann relation for electrons from Eq. (2.2), and taking $n_i = n_0$, Poisson's equation becomes,

$$\frac{d^2\Phi}{dx^2} = \frac{en_0}{\epsilon_0}(e^{\Phi/T_e} - 1)$$

Expanding e^{Φ/T_e} in a Taylor series for $\Phi << T_e$ to lowest order,

$$\frac{d^2\Phi}{dx^2} = \frac{en_0}{\epsilon_0}\frac{\Phi}{T_e}$$

The symmetric solution that vanishes at infinity distance is

$$\Phi = \Phi_0 e^{-|x|/\lambda_{De}}$$

where the Debye length is

$$\lambda_{De} = \left(\frac{\epsilon_0 T_e}{en_0}\right)^{1/2} \qquad (2.5)$$

In practical units,

$$\lambda_{De}(cm) \approx 743\sqrt{T_e/n_e} \qquad (2.6)$$

with T_e in volts and n_e in cm^{-3}.

2.3 Diffusion and Mobility

Diffusion and mobility are characteristic behaviors within the plasma bulk. Suppose the plasma density in the bulk plasma is higher near the center vessel than it is near the sheath edges. Ions and electrons will collide with each other and with neutral particles and diffuse outwards. If there is an external E-field, the ions and electrons will move but the neutral particles will not. Diffusion and mobility in the plasma bulk lead to the loss of ions and electrons from the plasma. We can derive some basic relations from the steady-state macroscopic force equation as follows.

$$qn\mathbf{E} - \nabla p - mn\nu_m \mathbf{u} = 0 \tag{2.7}$$

The three terms in the above equation represent E-field, pressure gradient and frictional force. n is the particle density, ν_m is the momentum transfer frequency which is a constant and independent of the drift velocity $\mathbf{u}$. Taking an isothermal plasma, such that $\nabla p = kT\nabla n$, and solving Eq. (2.7) for the particle flux $\Gamma = n\mathbf{u}$, we obtain

$$\Gamma = \pm \mu n \mathbf{E} - D\nabla n \tag{2.8}$$

where

$$\mu = \frac{|q|}{m\nu_m} \tag{2.9}$$

$$D = \frac{kT}{m\nu_m} \qquad (2.10)$$

are the macroscopic mobility and diffusion constants. In Eq. (2.8), the positive sign is for q positive and the negative sign is for q negative. The diffusion constant D has a unit of m^2s^{-1}. In terms of a scale length L, any initial non-uniformity is smoothed out in a time $T \approx L^2/D$. Using the definition of the mean speed $\bar{v} = (8kT/\pi m)^{1/2}$ and a mean free path (for hard-sphere scattering) $\lambda = \bar{v}/\nu_m$, we can write D as $\frac{\pi}{8}\lambda^2\nu_m$, which is in the form of $(\triangle x)^2/\tau$, i.e., the diffusion coefficient is based on a random walk with a step equal to the mean free path between collisions.

From Eq. (2.7), in the absence of an E-field, there will be a steady flow or flux of particles. The diffusion law takes the simple form

$$\Gamma = -D\nabla n \qquad (2.11)$$

known as *Fick's Law*.

The units of the mobility constant μ are $m^2V^{-1}s^{-1}$. These drift velocities are much less than the random velocities of the particles. μ and D are known as transport coefficients. Free diffusion is driven by the density gradient and drift is driven by the E-field.

In a plasma, the electrons tend to diffuse more rapidly than the heavier ions. If this results in n_e being different from n_i, an E-field is established, which accelerates the ions and slows down the electrons. We assume the flux of electrons and ions out

of any region to be equal such that charge does not build up. This is called ambipolar

diffusion. Using Eq. (2.7) for both species, with $\Gamma_e = \Gamma_i = \Gamma$ and $n_e \approx n_i = n$, we

have

$$\mu_i n \mathbf{E} - D_i \nabla n = -\mu_e n \mathbf{E} - D_e \nabla n \tag{2.12}$$

from which we can solve for $\mathbf{E}$ in terms of ∇n, and substitute the value of $\mathbf{E}$ into the

common flux relation.

$$\Gamma = -D_a \nabla n \tag{2.13}$$

where D_a is the ambipolar diffusion coefficient

$$D_a = \frac{\mu_i D_e + \mu_e D_i}{\mu_i + \mu_e} \tag{2.14}$$

2.4   Plasmas Parameters in Capacitive Discharges

One of the most widely used types of discharges is sustained by radio-frequency

(rf) currents and voltages, introduced through a capacitive sheath. A complete de-

scription of a plasma discharge with quantitative parameters is very complex. Here

we will simply demonstrate a self-consistent model summarized by Lieberman and

Lichtenberg [24]. This model is only qualitatively correct and describes the under-

lying physics for the analysis of real discharges. In order to compare with our PIC

simulation results in chapter 5, we describe a more realistic inhomogeneous model in this section.

A basic setup includes a gas between two large plates and a sinusoidal current flows across the discharge plates. For the inhomogeneous model, we allow the plasma and the sheath to be inhomogeneous, but assume the following to derive the discharge parameters n_e, n_i, and T_e, which are usually complicated functions of position and time.

- The ions respond only to the time-averaged potentials. This is a good approximation provided

$$\omega_{pi}^2 \ll \omega^2$$

where ω_{pi} is the ion plasma frequency and ω is frequency of rf supply.

- The electrons respond to the instantaneous potentials and carry the rf discharge current. This is a good approximation provided

$$\omega_{pe}^2 \gg \omega^2 \left(1 + \frac{\nu_m^2}{\omega^2} \right)^{1/2}$$

where ω_{pe} is the electron plasma frequency and ν_m is the electron-neutral collision frequency for momentum transfer.

- The electron density is zero within the sheath regions. This is a good approximation provided $\lambda_{De} \ll \bar{s}$, where $\bar{s}$ is the average sheath width. This holds if $T_e \ll \overline{V}$, where $\overline{V}$ is the dc voltage across the sheath.

- There is no transverse variation (along the plates).

The approximate self-consistent model equations are summarized here. We assume the width of the plasma bulk $d \approx l - 2s_m$, where l is the distance between two plane electrodes and s_m is the average sheath width.

Using a Maxwellian Distribution for integrating, we obtain the electron-atom collision rate constant associated with ionization

$$K_{iz}(T_e) = \sigma_0 \bar{\nu}_e \left(1 + \frac{2T_e}{\mathcal{E}_{iz}}\right) e^{-\mathcal{E}_{iz}/T_e} \tag{2.15}$$

where $\sigma_0 = \pi(e/4\pi\epsilon_0 \mathcal{E}_{iz})^2$, $\bar{\nu}_e = (8eT_e/\pi m)^{1/2}$, and $\mathcal{E}_{iz}$ is the ionization energy.

From particle conservation at low and intermediate pressures, we have

$$\frac{K_{iz}}{u_B} = \frac{1}{n_g d_{eff}} = \frac{2}{n_g d} \frac{n_s}{n_0}, \qquad \lambda_i \gtrsim \left(\frac{T_i}{T_e}\right) d \tag{2.16}$$

where λ_i is the ion mean free path, $u_B = (eT_e/M)^{1/2}$, and the ratio between the edge density and center density n_s/n_0 is given by Eq. (2.17).

$$\frac{n_s}{n_0} \approx 0.86 \left(3 + \frac{l}{2\lambda_i}\right)^{-\frac{1}{2}} \tag{2.17}$$

At higher pressures, we have

$$\frac{(K_{mi}K_{iz})^{1/2}}{u_B} = \frac{\pi}{n_g d}, \qquad \lambda_i \lesssim \left(\frac{T_i}{T_e}\right) d \tag{2.18}$$

where K_{mi} is the ion-neutral momentum transfer rate constant. For a given n_g and l, Eq. (2.16) and Eq. (2.18) determine T_e.

Internal heating in the plasma bulk is caused by collisional momentum transfer between the oscillating electrons and the neutrals. The time-average power per unit area, known as ohmic heating, $\overline{S}_{ohm}$ is given by

$$
\begin{aligned}
\overline{S}_{ohm} &\approx 1.73 \frac{m}{2e} \frac{n_s}{n_0} \epsilon_0 \omega^2 \nu_m T_e^{1/2} V_1^{1/2} d, &\lambda_i &\gtrsim \left(\frac{T_i}{T_e} \right) d \\
\overline{S}_{ohm} &\approx 1.73 \frac{m}{2e} \frac{n_s}{n_0} \epsilon_0 \omega^2 \nu_m T_e^{1/2} V_1^{1/2} \frac{2}{\beta} ln\, tan \left(\frac{\pi}{4} + \frac{\beta d}{4} \right), &\lambda_i &\lesssim \left(\frac{T_i}{T_e} \right) d \quad (2.19)
\end{aligned}
$$

where $cos(\beta d/2) = n_s/n_0$ and V_1 is the fundamental rf voltage amplitude across a single sheath.

The stochastic heating generated in the moving high-voltage sheath is due to elections reflecting from the large decelerating fields. For a single sheath in the slow sheath limit, we obtain

$$
\overline{S}_{stoc} \approx 0.45 \left(\frac{m}{e} \right)^{1/2} \epsilon_0 \omega^2 T_e^{1/2} V_1, \qquad \omega s_m \lesssim \overline{v}_e \qquad (2.20)
$$

2.5   Exciting Laboratory Plasmas

A sufficiently strong external E-field, produced by a DC or AC source, can cause electron impact ionization of the gas. The resulting electrons acquire energy from the field, are accelerated by the field, and contribute to further ionization, leading to a breakdown cascade. The mean electron energy, at least initially, must exceed the thermal energy of neutral particles of the gas. The resulting system of external fields

and charged particles must locally satisfy Maxwell's equation at all times. The full 3-d solutions of these equations for varying conditions of external field, plasma species densities and velocity distributions can be quite complex. The solutions, and even the compact description of the means to solve these problems, are the subject of numerous monographs, texts, and research papers [27, 28, 29, 30]. In a later section, we will discuss the limited set of issues necessary to describe our attempts at such solutions using high-order computational methods. For now, it is sufficient to know that the energy acquired from external field is either radiated, as photons, or transferred to the walls or internal components of the system via collisions. Obviously, when input powers exceed the level of tens-of-watts per cubic centimeter, releasing this energy as radiation is highly desirable to reduce the level of heroics needed to avoid melting the physical structures of the lamp.

Methods of plasma generation are many and varied. In general, the optimal means to excite gases depends a great deal on the species involved and on the pressures of operation. A widely used method of plasma generation for high pressure systems is to directly ejected electron beams (EB) into the gas. EB ionization has additional advantages for excimer and chemical lasers because the injection can be done using ultra-short pulses, allowing excellent control of the dynamics, and reducing heating issues which are important for maintaining the purity of optical modes in the cavity. In some excimer laser systems, secondary electrons are accelerated by an external E-field, and generate short-lifetime excited molecules with sufficient gain.

Resonant radiation whose wavelength corresponds to the energy of atomic transi-

tions in the gas atoms also can contribute to production of a high density plasma when subsequent collision of these atoms leads to ionization. This plasma is called a photoresonant plasma in which the temperature of the excited atoms can be somewhat in excess of the electron temperature T_e.

Plasmas can be created by laser irradiation of a surface. When a short laser pulse is focused onto a surface, material evaporates from the surface and forms a plasma. These plasmas often have sufficiently high density to illustrate another important fundamental parameter of plasmas, called the "cut-off" density, n_c. When n_e exceeds n_c, electromagnetic waves cannot propagate. This provides a natural upper limit to the density of the plasma that a given input laser frequency can sustain, making it possible to generate pulse plasmas and allows the study of fast plasma process.

2.6 Optical Emission in Plasma

When two atoms approach each other, their resonance lines are broadened because of the formation of molecular potentials perturbing the atomic states for which optical emission can occur. For diatomic molecules, the electronic states are specified first by the component Λ of the total orbital angular momentum along the internuclear axis with symbols Σ, Π, Δ, and Φ corresponding to $\Lambda = 0, \pm1, \pm2$, and ±3. All these states are doubly degenerate except for the Σ states. For Σ states, $+$ or $-$ signs are often used to denote a symmetric or antisymmetric wave function. The total electron spin angular momentum S is also specified, with the multiplicity $2S + 1$ written as

a prefixed superscript. For homonuclear molecules the subscripts g or u are written to denote whether the wave function is symmetric or antisymmetric with respect to interchange of the nuclei.

Molecular spectra result from the transitions between different molecular states. To describe these states, three kinds of motions are important: motion of electrons, vibrational motion of nuclei and rotational motion of nuclei. Simultaneous quantum-mechanical treatment of these three forms of motions is very difficult even for simple molecules such as H_2. However, since the nuclei are much heavier than electrons, each form of motion can be treated separately (see Appendix A). The complete wave function appears as the product of the wave functions of the three forms of motion and the total energy as the sum of the corresponding energies.

$$\psi = \psi_{el} \cdot \psi_{vib} \cdot \psi_{rot}$$

$$E = E_{el} + E_{vib} + E_{rot} \tag{2.21}$$

For a transition in which the states of all three forms of motion change, the emitted photon energy $(h\nu)$ is given by

$$h\nu = \Delta E = E' - E'' = (E'_{el} - E''_{el}) + (E'_{vib} - E''_{vib}) + (E'_{rot} - E''_{rot}) \tag{2.22}$$

The simplest (harmonic oscillator) model for the vibration of diatomic molecules

leads to equally spaced quantized, nondegenerate energy levels.

$$E_{vib} = \hbar\omega\left(\nu + \frac{1}{2}\right) \tag{2.23}$$

The selection rules for vibrational transitions are

$$\left(\frac{d\mu}{dR}\right)_{R=R_e} \neq 0$$

$$\Delta\nu = \nu' - \nu'' = \pm 1 \tag{2.24}$$

This means that for a transition restricted to a single electronic state, a vibrational

transition can occur only if the dipole moment changes during the vibration and

only between adjacent vibrational levels. For transitions between different electronic

states, this selection rule is no longer rigorous and $\Delta\nu$ can be any integer.

The simplest (dumbbell) model for the rotation of diatomic molecules leads to the

nonuniform quantized energy levels.

$$E_{rot} = \frac{\hbar^2}{2I_{mol}}J(J+1) \tag{2.25}$$

where $I_{mol} = m_R\overline{R}^2$ is the moment of inertial and $J = 0, 1, 2, \dots$ is the rotational

quantum number. These levels are degenerate, with $2J + 1$ states for the Jth level.

The spacing between rotational levels increase with J. Rotational transitions obey

the following rules.

permanent dipole moment $\mu \neq 0$

$$\Delta J = J' - J'' = 0, \pm 1$$

$$0 \nrightarrow 0 \tag{2.26}$$
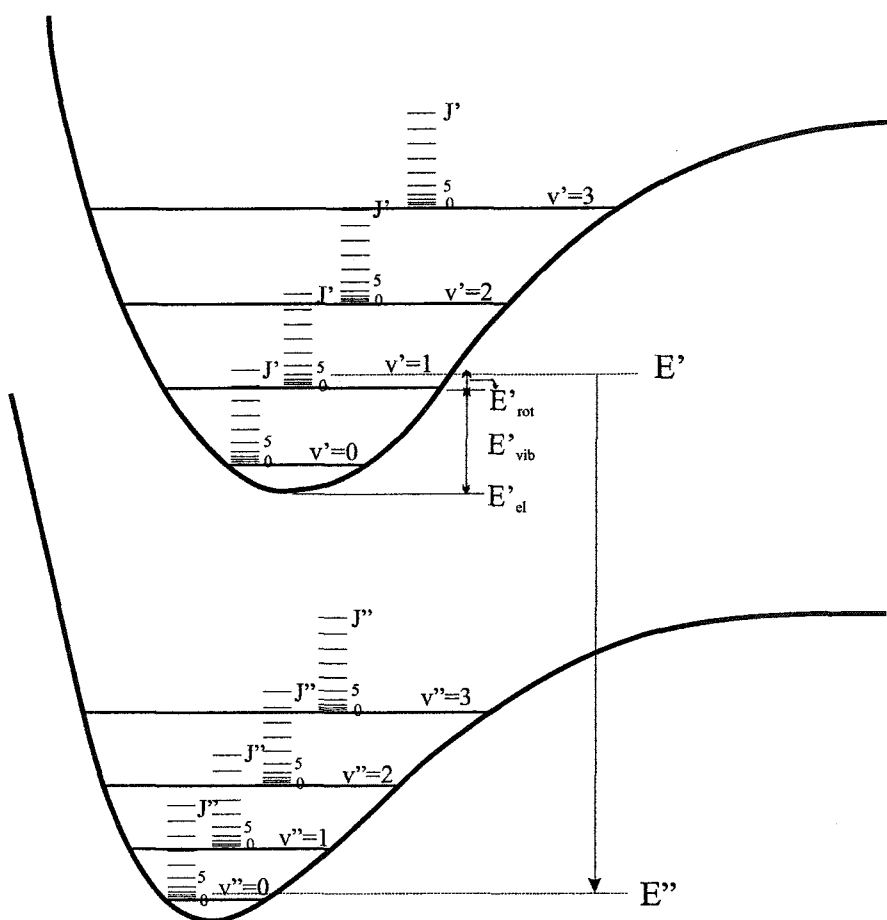
Figure 2.2: Potential energy curves for the electronic states of a diatomic molecule including vibrational and rotational levels of the two electronic states

A photon can be emitted by a transition between electronic levels, between vibrational levels of the same electronic state, or between rotational levels of the same

electronic and vibrational state. Fig. 2.2 demonstrates a transition from an excited molecular state to a lower energy state. Electric dipole radiation is the strongest mechanism for photon emission. The selection rules for electric dipole radiation are

$$\Delta \Lambda = 0, \pm 1$$

$$\Delta S = 0 \tag{2.27}$$

In addition, for transitions between Σ states the only allowed transitions are

$$\Sigma^+ \rightarrow \Sigma^+ \text{ and } \Sigma^- \rightarrow \Sigma^- \tag{2.28}$$

and for homonuclear molecules, the only allowed transitions are

$$g \rightarrow u \text{ and } u \rightarrow g \tag{2.29}$$

2.7 Excimer Lamps

<u>DC Excitation</u>

For dc glow discharge systems, the threshold electric field for electrical breakdown of gases is governed by the Paschen curve [23]. The threshold voltage needed to create breakdown in a given gas, when applied to electrodes of a given material is given by

$$V = \frac{B \cdot pd}{ln(A \cdot pd) - ln[ln(1 + \frac{1}{\gamma})]} \tag{2.30}$$
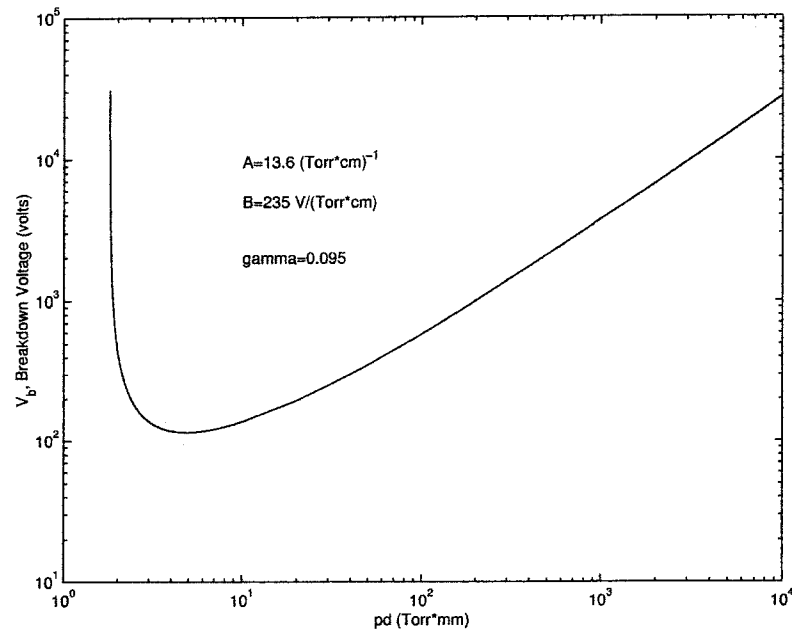
Figure 2.3: Paschen curve for argon gas between tungsten electrodes: a plot of breakdown voltage as a function of electrode separation times the pressure

where the secondary electron yield γ, the so-called second Townsend coefficient, is the yield of electrons coming from the cathode when bombarded by an ion. This parameter is a function of the material and is quite sensitive to gas-coverage and other contamination effects. In the expression above, p is the gas pressure, d is the electrode separation, and A, B are constants whose value also can depend on the choice of gas and electrode material.

Many different characteristics of DC discharges can be illustrated by the voltage-current relationship, as shown in Fig. 2.4. When the voltage across the two plane electrodes, 2 cm in diameter, with 50 cm separation, in neon at a pressure of 1 *torr*, is increased slowly, random current pulses will result initially. With the increase of the
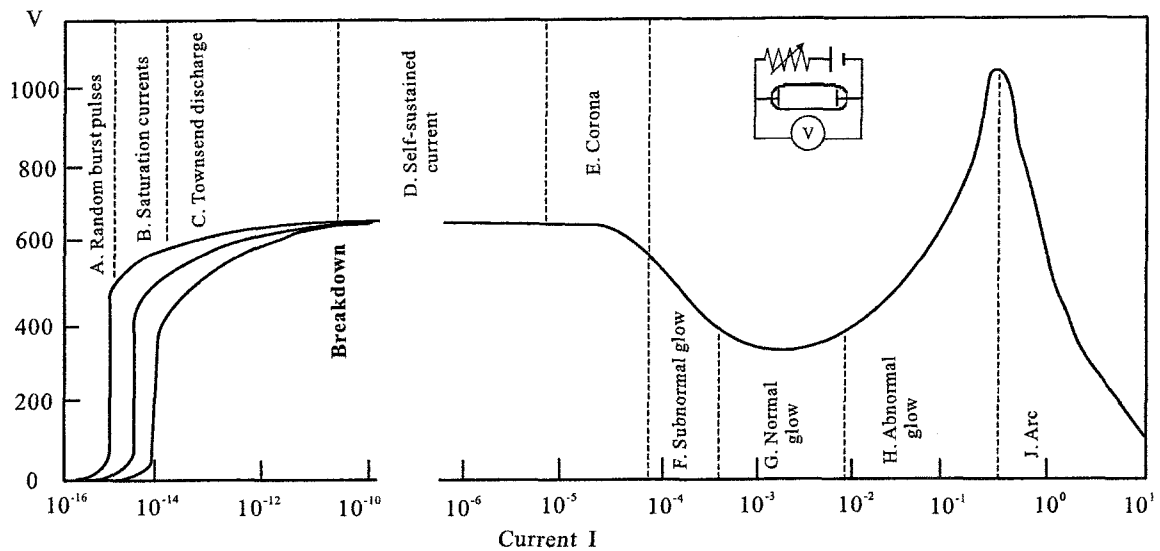
Source: H. V. BOENIG, *Plasma Science and Technology*, Cornell University Press Ltd, pp. 24, 1982

Figure 2.4: Voltage-current relationship in glow discharges with two plane electrodes of 2 cm diameter with 50 cm separation, in neon at a pressure of 1 torr

number of free electrons, a steady small current will be observed. This small current is almost independent of the increasing voltage below certain point. After that, the current will begin to rise in an exponential manner, which is called Townsend discharge. Further increase of the voltage will result in an extremely rapid increase of the current, followed by a collapse of the voltage across the gap, called breakdown. If the current is increased further by reducing the resistance of the external circuit, the voltage will drop to a low level to yield an exponential increase in current in the abnormal glow region.

The visible spatial structure of a glow discharge is illustrated in Fig. 2.5 in various distinctive regions between the cathode and the anode. Starting from the cathode, one
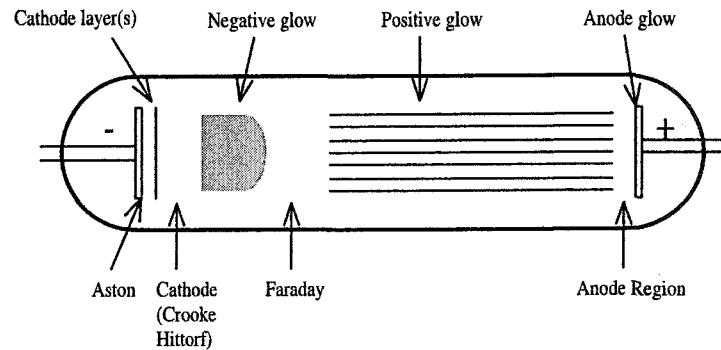
Figure 2.5: Regions in glow disorder [Boenig (1982)]

may occasionally observe a thin dark area called "Aston dark space". It is followed

by the cathode glow layers, and much more-easily seen dark spaces associated with

the sheath, the negative glow, the Faraday dark space, which is often also hard to see,

the positive column, the anode dark space, and the anode glow. The zone from the

cathode surface to the bright edge of the negative glow is of considerable importance

because in electropositive plasmas the spatial rearrangement of charge associated with

the solution of Maxwell's equation (Poisson's equation) causes most of the voltage

drop to appear across this zone. In this zone, electrons with low initial energy are

emitted from the cathode, by ion impact on the cathode as they fall across the high

sheath potential. The electrons have a surplus compared to the ion density in this

non-quasi-neutral region. This results from a necessary condition of equilibrating

fluxes across the sheath under the assumption that the electron speed is to low to

permit ionization in the zone. This is what forms a sheath in which current is carried

mainly by the positive ions moving toward the cathode. The mathematics of this

sheath is described in Sec. 2.2.

The negative glow is often, though not always, visually the brightest part of the glow discharge because of the energetic electrons arriving at the end of the cathode dark space where they have gained their maximum energy. At the boundary of the negative glow, electrons incur inelastic collisions and induce excitation and ionization. As the electrons are slowed down these reaction rates decrease and this reduces the brightness of the negative glow until it merges into the Faraday dark space. The positive column is in an ionized state with equal densities of positive and negative particles. It usually exhibits a steady and uniform luminosity and is used in many applications including light sources, commercial advertising signs, plasma sources, and plasma torches. A negative dark space charge exists in the anode glow region because it merely collects electrons. A voltage drop across this zone, called "anode" is on the order of the ionization potential of the gas. Electrons from the positive column gain energy in the anode fall and sometimes cause a faint glow at the anode surface. It is also possible that ions are generated in this region that enter the positive column.

The cathode region of a glow has a potential fall of about 100-400 *volts* and a low current density. Thermal effects do not contribute very much to the functioning of the cathode of a glow discharge, and the light emission near the cathode has the spectrum of the gas.

In strong contrast to glow discharges, when two carbon or metal electrodes are brought into contact, and then separated, in a circuit of capable of providing a high

current, a self-sustained arc discharge takes place. Fig. 2.5 illustrates a typical ar-
rangement for generating an arc discharge. In the arc region as shown in Fig. 2.4, the
current is about two orders of magnitude higher than in the glow, while the voltage
is about one order of magnitude lower. An arc has a characteristic voltage in cathode
region that is very low, of the order of 10-30 volts depending on material, compared
with a glow discharge. Light emission in arcs has the spectrum of the vapor of the
cathode material. As mentioned above, pushing glow discharges beyond an upper
current (or neutral pressure) limit can cause them to enter the arc regime.

AC Plasma excitation

(a)

(b)   (c)
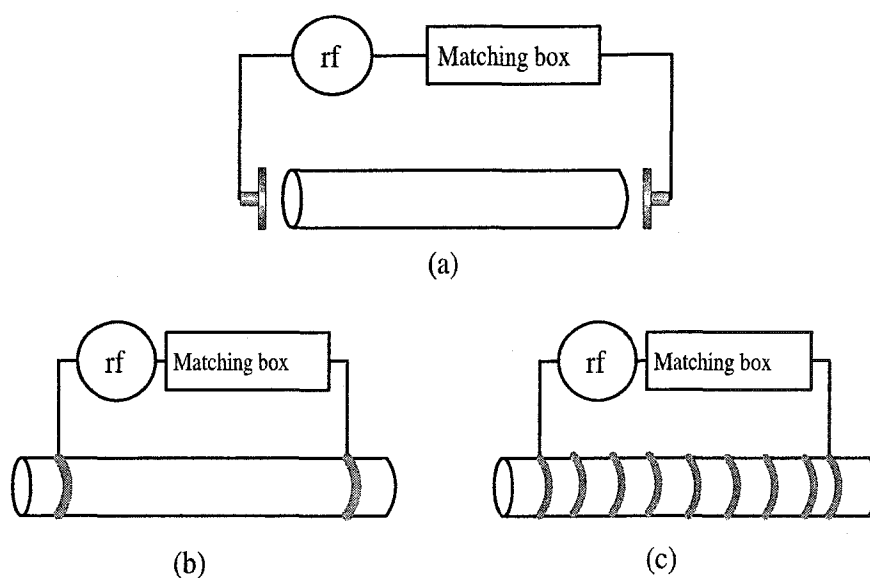
Figure 2.6: Typical arrangements for electrodeless rf discharges: (a) plates outside the
discharge zone, (b) rings, and (c) a coil around the reactor

Radio-frequency (10KHz - 300MHz) and microwave (>500MHz) discharges have
become particularly important in generation of UV sources because energy can be

coupled into the reactor with electrode-less arrangements. Chemical reactions, induced by electron-impact processes, which produce intense UV photons can last much longer for more stability and longer life time. Fig. 2.6 illustrates several techniques for capacitive or inductive coupling of radiowave power into a discharge.

The capacitively coupled designs can be easily changed to corresponding cylindrical arrangements as shown in Fig. 2.7. Such capacitively coupled rf systems are presently widely used for UV production [18]. These lamps typically have at least one piece of dielectric material between electrodes, so they are called dielectric barrier discharges (DBD); they are also known as silent discharges. Conventional DBD lamps can have maximum efficiencies near 20%, depending on the working gas. This discharge method has potential applications because of its simplicity, high efficiency, and low cost.
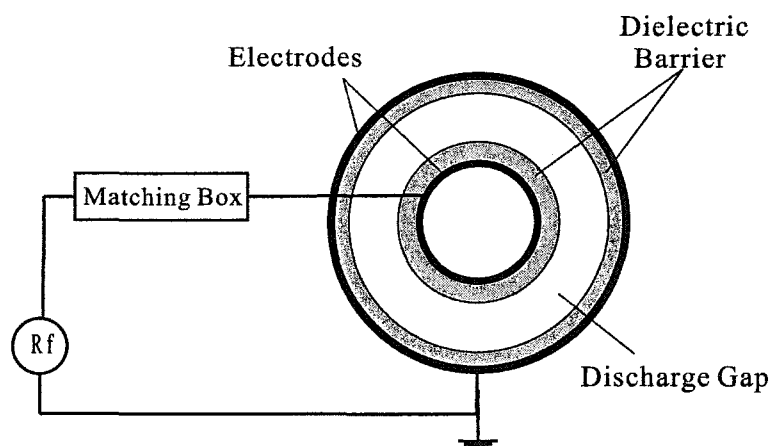
Figure 2.7: Cylindrical shell model of a rf discharge

Microwave lamps, which are much less common than DBD lamps in high-power

industrial use, are usually comprised of a resonant cavity, tuners, wave-guides, at least one magnetron, and a power supply (see Fig. 2.8). The combination of magnetron and power supply forms the heart of every microwave lamp. At microwave frequencies, energy coupling is obtained by passing the discharge tube directly through a section of wave-guide.
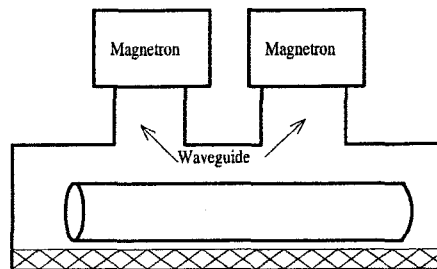
Figure 2.8: A schematic microwave lamp system

In these high-frequency (hf) discharges generated in rf and microwave systems, energy is transferred from external field to electrons. As for dc systems, excited atoms, molecules and ions are generated via collisions between energetic electrons and neutral gas molecules or atoms. The collisions tend to convert the oscillating motion of the electrons into a random motion. The average power, P, transferred per unit volume gas in this mechanism [31] is

$$P = \frac{n_e^2 E_0^2}{2m_e} \cdot \frac{\nu_c}{\nu_c^2 + \omega^2} \tag{2.31}$$

where E_0 is the amplitude of the h-f field strength, n_e and m_e are the electron density and mass, ν_c is the elastic collision frequency, and ω is the frequency of the applied

field. The magnitude of ν_c is between 10^9 and $10^{11}s^{-1}$. Thus for rf frequencies where ω is around $10^7 s^{-1}$, the effect of the driving frequency disappears. At microwave frequencies, $\omega \approx 10^{10}s^{-1}$, both terms in the denominator are important. This is one of the main differences among many others that yield interesting variance in the light output of these two styles of lamps working with the same gas mixtures at similar input power densities. We will have much more to say about this subject in the section on plasma simulations.

2.8   Commercially Available Lamps

Commercial UV lamps are mostly widely used in curing equipment since this is the largest and fastest growing market in the UV application industry. In the North American market the projected growth rate in 2004 for prototyping, ink jet, adhesives, medical, automotive applications of lamps is between 25% and 30% [32]. Many of these systems still use arc lamps for low cost. However, electrodeless lamps are becoming more prominent because of their numerous maintenance and reliability benefits. The typical performance of a lamp using electrodes for excitation drops to 60% of its initial output after 2000 hours, while an electrodeless lamp may operate without reduction for up to 8000 hours at high power outputs.

Most of the commercially available electrodeless lamps are based on microwave systems. The CoolWave Microwave-Powered UV system and ThruWave UV system made by Nordson (www.nordsonuv.com) have a typical running power of 160-240

watts per cm of bulb length. Fusion UV system (www.fusionuv.com) has a full series of systems, like their F series and their Light Hammer series, offering a power of 120-240 watts/cm. Other companies like Primarc UV Technology (www.primarcuv.com), Axcelis (www.axcelis.com), and JenAct Limited (UV)(www.jenact.co.uk) also manufacture electrodeless microwave lamps. RF powered UV lamps are not yet widely available as microwave lamps. In 2003, Fusion UV System announced their new PowerCure1, which is the smallest electrodeless RF lamp system in the world delivering high power UV.

Chapter 3

Experiment Setup

This chapter describes the apparatus of our experiments with emphasis on the engineering of building RF and microwave electrodeless lamps. Both the RF and microwave lamps have their electrodes outside the bulb and allow for large area, high power, and efficient discharges from UV to IR regions.

3.1 Capacitively Coupled RF Lamp

A typical RF lamp system includes an RF power supply (usually at the frequency of 13.56 MHz), a matching network, a means to couple RF energy into the discharge, a housing for shielding and cooling system. In our apparatus, we also have vacuum system, gas delivery system, optical characterization system, and data acquisition hardware and software. The gas used can be any gas that can break down under the h-f field and output photons at the desired wavelengths. So they can emit wide range of photons from UV to IR. The wavelength is tunable by changing gases.

3.1.1 Coupling Means
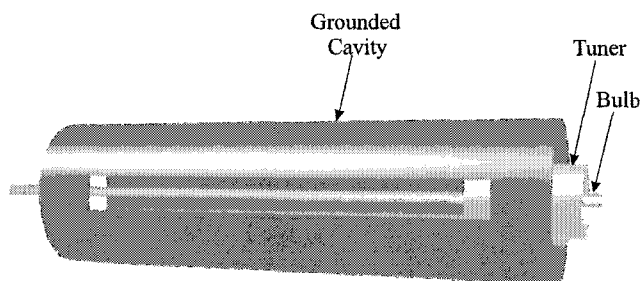
Figure 3.1: Schematics of the RF lamp: the tuner is placed concentric to the grounded cavity, and the bulb is in the center

Fig. 3.1 shows our RF lamp schematics. In this design, we aim at cost efficiency, simplicity, large area, and high input power. In its simplest form, the lamp consists of an rf generator (ENI Power System, Inc., Model ACG-10), an impedance matching network, external coupling electrode (tuner), and a lamp bulb in a grounded cylindrical cavity. The grounded cavity, made of stainless steel, is 500 mm long and 113 mm in inner diameter (ID). The external electrode (tuner), is a cylindrical aluminum conductor of length 75.3 mm and ID 73.2 mm. The bulb, external electrode, and grounded cylindrical cavity are arranged concentric to each other. This special tuner provides an adjustable capacitance between the center conductor (plasma) and ground. Thus the tuner forms both a part of the cabling to the power supply as well as an electrical high potential interior boundary, surrounding the plasma inner conductor, forming a short triaxial section of waveguide on one end of the cylindrical cavity. The entire lamp arrangement is housed in a Faraday cage to reduce RF leakage.

3.1.2 Matching Network

In discharges directly driven by RF generators, power is not transferred effectively from the source to the discharge; a matching network is usually required. Consider a discharge, which usually has a complex impedance $Z = R + jX$. In order to match the load with the source to allow maximum rf power transfer, one must have $X=0$ and $R=$the source resistance [24].
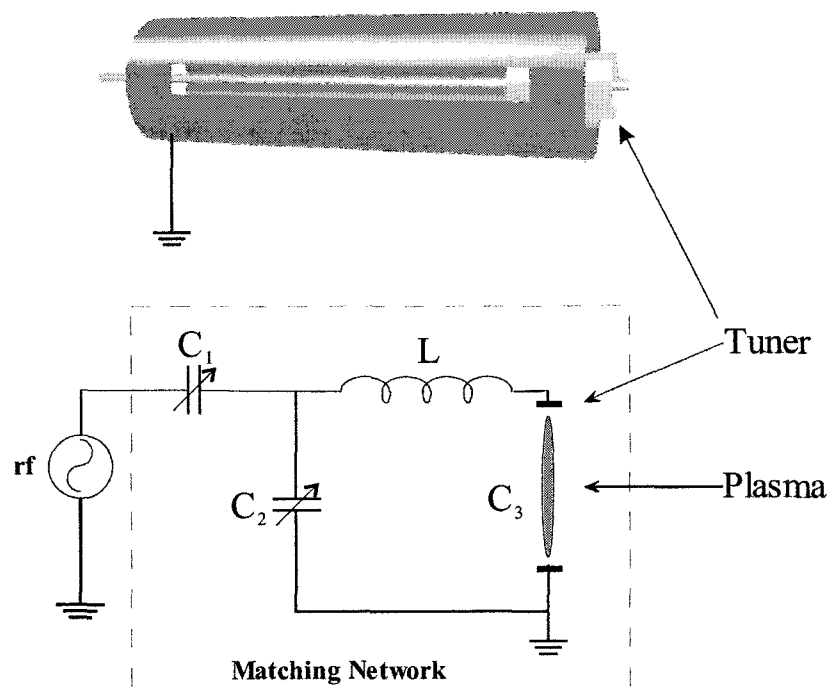
Figure 3.2: Matching network

Fig. 3.2 shows our matching network. It includes an inductor (L) and two variable capacitors (C1 and C2). This impedance matching network transforms the lamp impedance into a constant 50 Ω of pure resistance. A Smith chart [33] was used to

predetermine the values of the inductance (L) and capacitance (C) of the matching network components necessary for maximum power transfer between the generator and plasma. The total capacitance, C, and inductance, L, providing the best matching conditions, for this system, varied between 100pF - 150pF and 2μH - 4μH respectively.

A high voltage circuit, such as a variable vacuum capacitor is required because of the high RF power (up to 1 kW). For simplicity, we use only one variable capacitor at the position of C_2, which makes the system functional for our experiments. The one we use has a range of from 5 to 250pF and can withstand a voltage of up to 15kV.

The inductive coil used as the inductor has a radius of $R = 1.75$ inches, the length along the coil axis $l = 5.4$ inches, and a total of $N = 12$ turns. The inductance L of the coil was calculated to be between 2 μH and 5 μH. Using Grid-dip and $L - C$ meters, the above value of L was confirmed to be within $\pm 0.5\mu$H. These values of L and C, for the impedance matching network, allow for a maximum power transfer at 13.56 MHz into a reactive plasma load from a 50 Ω source impedance.

3.2 Microwave Lamp

Magnetrons are the most popular sources for generating microwave. Because of their low cost and compactness, some electrodeless UV lamp systems using microwave power are available commercially (see Sec. 2.8). Our microwave lamp system consists of a microwave cavity, a power supply (comprising of magnetrons and step-up transformer combination), cooling fans, and a lamp bulb. In this design, the probe of the

magnetron is directly coupled into the microwave cavity. The cavity is designed to be overmoded, that is, the dimensions of the cavity and the locations of the probe couplers are selected to allow multiple modes to simultaneously exist. Both cylindrical and flat panel versions of the microwave drive can be constructed with one to six (1kW to 2kW) magnetrons allowing for between 1 kW to 10 kW input powers. Fig. 3.3 shows the six magnetron microwave drive. The complete description of the one magnetron drive can be found in the dissertation work Joseph D. Ametepe [34].

3.2.1 Microwave Lamp with an Overmoded Cavity
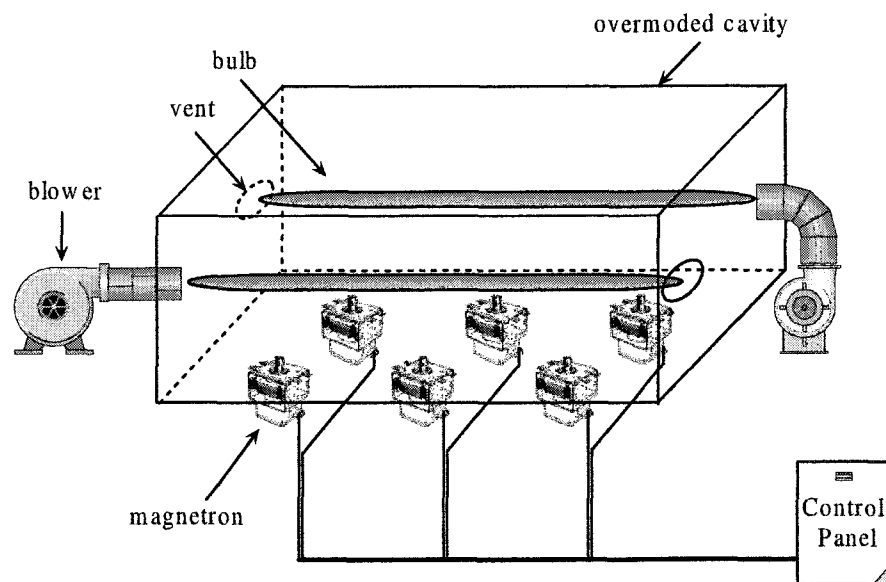
Figure 3.3: Schematics of the Microwave Lamp: six magnetrons directly couple to the overmoded cavity and two bulbs are put on top of them

The dimensions of the six magnetron cavity are $50.8 \times 35 \times 12.7$ cm. It is made of aluminum, because aluminum is light, easy to form, and it has high reflectivity and low

skin depth for microwaves. The coupling probes of the magnetrons are couple spaced 15.24 cm apart in the longitude direction and 12 cm apart in the transverse direction to avoid cross-talk between them. A high voltage step-up transformer was built for the magnetrons. The magnetrons and step-up transformer combination forms the heart of this microwave drive. In principle, this six magnetron arrangement permits operating the lamp up to 10 kW; in practice we have generally confined operations to less than 5 *kW*.

3.2.2 Magnetron and Step-Up Configuration

While the external configurations of different magnetrons vary, the basic internal structures are the same. The internal structure includes an anode, a filament or cathode, an antenna, and two high-field permanent magnets to provide the B field parallel to the cylinder axis (see Fig. 3.4). The anode (or plate) is a hollow metal cylinder, from which even number of anode vanes extend inward. To create an annular series of regular open galleries, these spaces form the resonant cavities that serve as distributed, tuned circuits that determine the output frequency of the tube. The anode operates in such a way that the segments alternate in polarity around the azimuth. In effect, the cavities are connected in parallel with regard to the output. The filament, also called the heater, serves as a cathode located in the center of the magnetron. The filaments, supported by the large and rigid leads, are vacuum sealed into the tube and electromagnetically shielded. The antenna is a probe or loop that

A

Cathode

Electron motion
in an electric field

B Magnet

N

S

Magnet

C Circular
motion of
electrons

Field around
electrons

Magnetic
field

Electron motion
on a magnetic field

D

The effect of combined
electric and magnetic
fields on electron travel
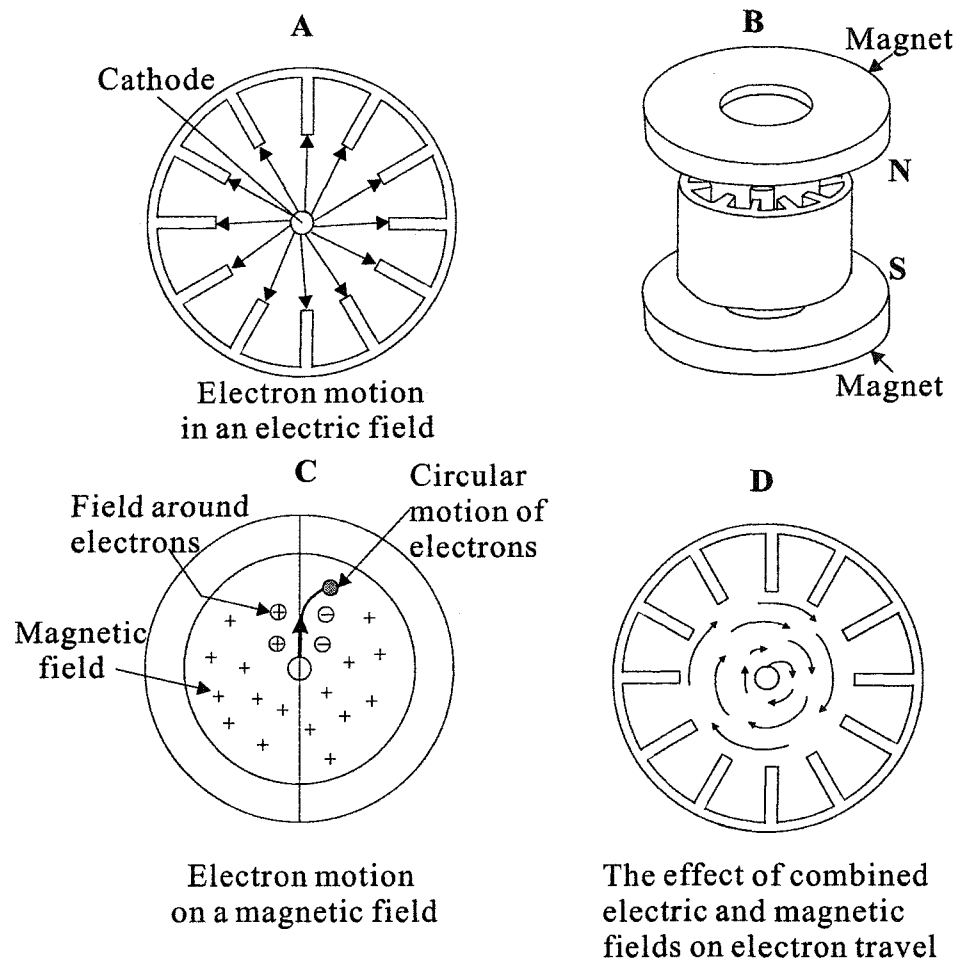
Figure 3.4: Electron motion in a magnetron tube (Michael S. Wagner)

is connected to the anode and extends into one of the tuned cavities.

3.3 Ultraviolet Transmitting Glasses (Bulbs)

Optical materials with good ultraviolet transmitting properties are required in spec-

troscopy as window materials for lamps, filters and lenses. Principal causes of optical

losses are: intrinsic absorption, absorption resulting from the presence of impurities

and light scattering within the bulk glass. In the UV spectral region, losses are mainly caused by electronic transitions, whereas in IR region atomic and molecular vibrations are responsible for absorption.

Pure silica (SiO_2) is a very good UV-transmitting material. The basic blocks in its structure are corner-sharing tetrahedral $[SiO_4]^{4-}$ units. Absorption is caused by the excitation of an electron from the valence band to unoccupied higher energy states. In SiO_2, the absorption corresponds to the transition of electrons belonging to tightly bound bridging oxygens [35]. Glasses containing weakly-bound oxygens are less transparent in the UV-region than vitreous SiO_2 [36].
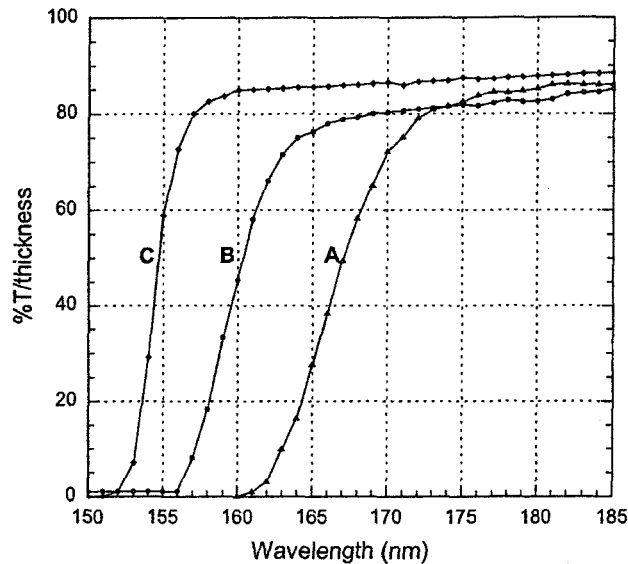
Figure 3.5: VUV transmission spectra of high OH in: (A) silica glass; (B) dry silica glass; (C) dry, fluorine-doped silica glass. Path length for samples A and B is 5 mm; sample C is 6.35 mm

High-purity silica glass is typically made by a flame hydrolysis or combustion

process, in which bulk glass can contain hydroxyl (or -SiOH). The amount of hydroxyl in pure silica is a major concern of the absorption around 157 nm. The electronic transition of hydroxyl resides in the VUV-region are due to the excitation from the oxygen $2p$ level to a SiO-H anti-bonding state [37]. For this reason, SiO_2 soot is chemically dried to remove hydroxyl ions before the glass formation. Alternatively, fluorine-doped silica glass has a better UV transmission rate [38] and can be used in various applications such as the photomask substrate. Fig. 3.5 compares the VUV spectra of: A, high OH containing silica glass ($\sim$900 ppm (wt.) of OH); B, dry silica glass (<0.5 ppm (wt.) of OH); and C, dry and fluorine-doped ($\sim$ 1% (wt.)) silica glass.

The bulb material we use is Type 021Al made by GE Quartz. This is a dry synthetic fused silica material providing high transmittance in the deep UV region. It combines the advantages of low hydroxyl content with ultra high purity to yield superior UV transmittance and resistance to solarization for our lamps. Fig. 3.6 is the transmission curve obtained from the manufacturer. Glasses with a thickness of 3 mm were measured to have transmission rate of 90% at 180 nm, 30% at 170 nm, and about 10% at 160 nm. The bulbs we made from this material are $\sim$120 cm long and have a wall-thickness of 1 mm. The (exponential) attenuation factor inferred from Fig. 3.6, means that our bulb jacket absorbs a factor $(2.72)^3$, or $\sim$20 times, less than the numbers indicated there. This agrees well with our measured values, derived in experimental calibrations.

* Data obtained from *Larry Zeng*, GE Quartz Inc. 12/05/2002
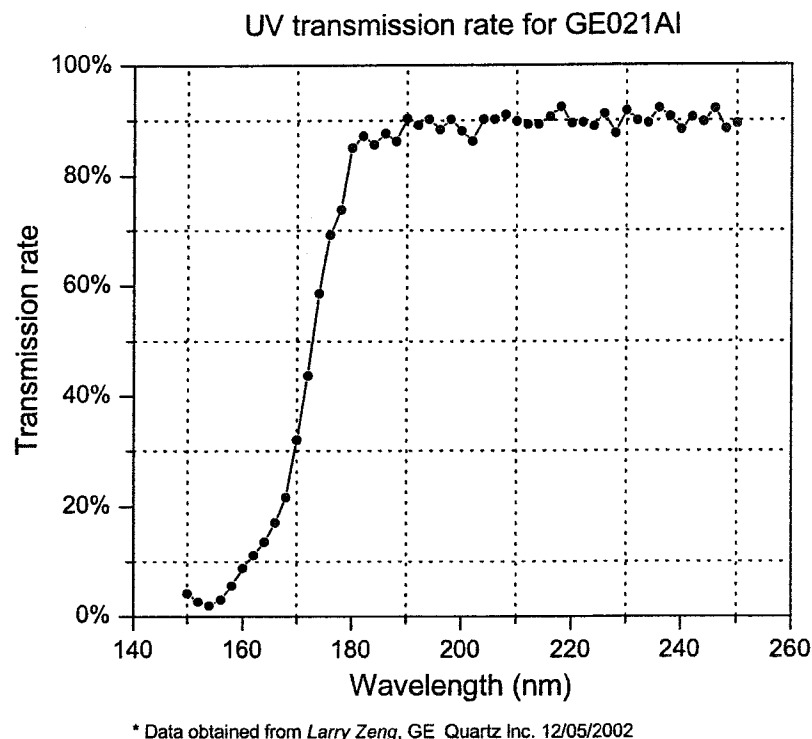
Figure 3.6: Measured VUV transmission rate for Type 021Al fused silica with a thickness of 3 mm

3.4 Vacuum System

Gaseous contaminations of the discharge may influence many interacting processes taking place in the discharge chamber, such as the generation of primaries, energy transfer and the formation of desired molecular orbits. It is very important to keep a clean environment, especially in spectroscopy. The detection limit using atomic spectroscopy is as low as 0.1 ppm [39]. Since we are interested in discharges in high pressure gases from 100 torr to over 1000 torr, a base pressure of less than 10^{-5} torr

is required.

Usually polymerized pump oil buildup from back streaming of the rough pump can be easily dissociated by discharges and leaves contaminations of carbide or carbon. It is very difficult to clean them up once they stick on the surface of the bulb. For this reason, we designed an oil free system which combines a turbo molecular pump and a dry pump with the gas delivery system. The backing pump is from LACO Technologies (Model: DRYTEL 31). It is composed of a molecular drag pump and a dry diaphragm pump, and can get down to $\sim 10^{-6}$ torr with a pumping speed of 7.5 l/s. The turbo molecular pump is from LEYBOLD (Turbovac 450), which features at a pumping speed of 450 l/s and an ultimate pressure of 10^{-8} torr. Our system can reach base pressure in the mid to high 10^{-7} torr range.

Fig. 3.7 describes a diagram of the vacuum system. The variable leak valve V6 (DUNIWAY VLVE-1000) has sapphire orifice, contained with vented threads to prevent trapped gas in the piston assembly. It has a controlled leak rate of 10^{-10} torr·l/s(minimum), and allows accurate adjustment of the fill-in gas pressure. G1 is a convectron gauge tube with the measuring range 10^{-3} torr to 1,000 torr. The ion gauge G2 has iridium filaments and a bulb coated with a platinum film allowing measurement from 10^{-4} torr to 10^{-10} torr. G1 and G2 work together to provide a full range pressure measurement of our system. Since convection gauges are usually calibrated with nitrogen and are sensitive to the type of gas being measured, we use G3 to measure the fill-in gas pressure. This MERIGAUGE digital pressure gauge (Meriam Instruments) features an accuracy of $\pm 0.25\%$ at full scale over a range 0 to
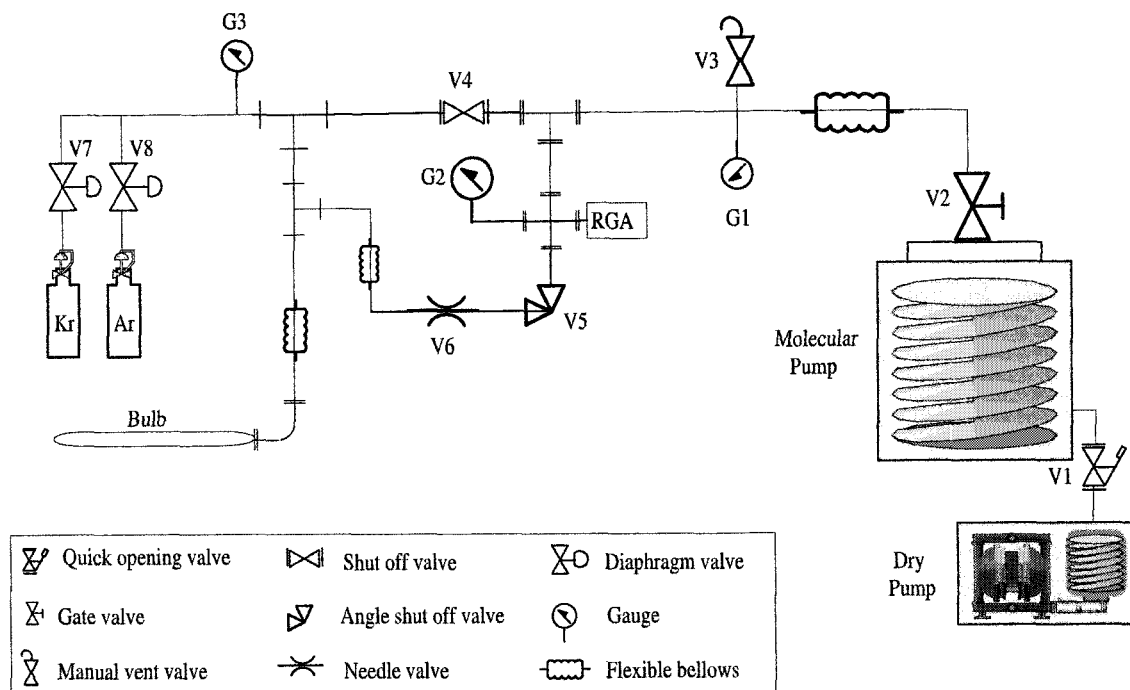
Figure 3.7: Diagram of the vacuum system and gas delivery system

100 PSI. This gauge does not depend on gas type.

3.5 Optical Characterization System

3.5.1 McPherson M218 System

To characterize the lamp's output, we constructed a spectrometer based on a 0.3

m McPherson Model 218 vacuum scanning monochromator, equipped with a 1200

line/mm plane grating blazed at 200 nm. A turbo pump, backed by a dry pump,

evacuates the system (see Fig. 3.8) to pressures $\sim 10^{-5}$ torr. Light from the lamp

reaches the spectrometer through an 8 mm ID suprasil tube evacuated to below
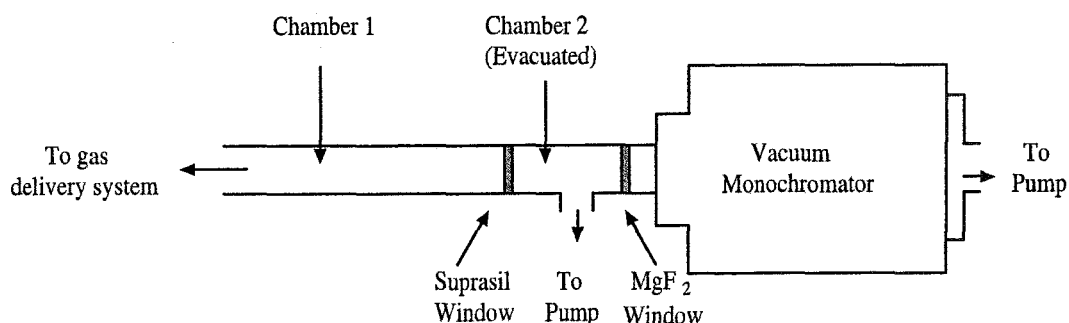
Figure 3.8: Schematic of light detecting system: the spectrometer and light path. Chamber 2 and the monochromator system are evacuated to 10^{-6} torr

10^{-5} torr to overcome the absorption of air below λ=200 nm. A commonly used detector for the VUV is a combination of a fluorescent material with a blue sensitive photomultiplier tube. What we use is a Hamamatsu R928 photomultiplier tube with a sodium salicylate scintillator.

Sodium salicylate has a constant and high fluorescent efficiency over a large range of UV [40], so it is the most commonly used phosphor for detection of UV radiation. For the best light conversion, the layer should be as smooth as possible, and the uniformity of the thickness must be well controlled. We used a spray technique similar to that used by Seedorf et al. [41]. A saturated solution of sodium salicylate was sprayed onto a piece of glass at a distance of 50 cm to form a thin layer between 10 and 14 mg/cm^2. The difference in our technique is that we used a heat gun to heat the deposit surface during spraying to prevent big islands that were observed by Seedorf *et al.* [41].

3.5.2 OceanOptics S1024DW System

We also built a very compact, portable VUV spectrometer based on an OceanOptics S1024DW. The S1024DW Deep Well Detector Spectrometer from OceanOptics features a 1024-element photodiode array (PDA) for applications requiring high signal-to-noise (S/N) measurements. To increase the VUV response, the window on the face of the PDA array was removed. With a 2400 line grating blazed at 150 nm and a 100 micron slit, this spectrometer provides a resolution of 1.12 nm at around 190 nm.

Port with flanged MgF_2 window

To pump Data port
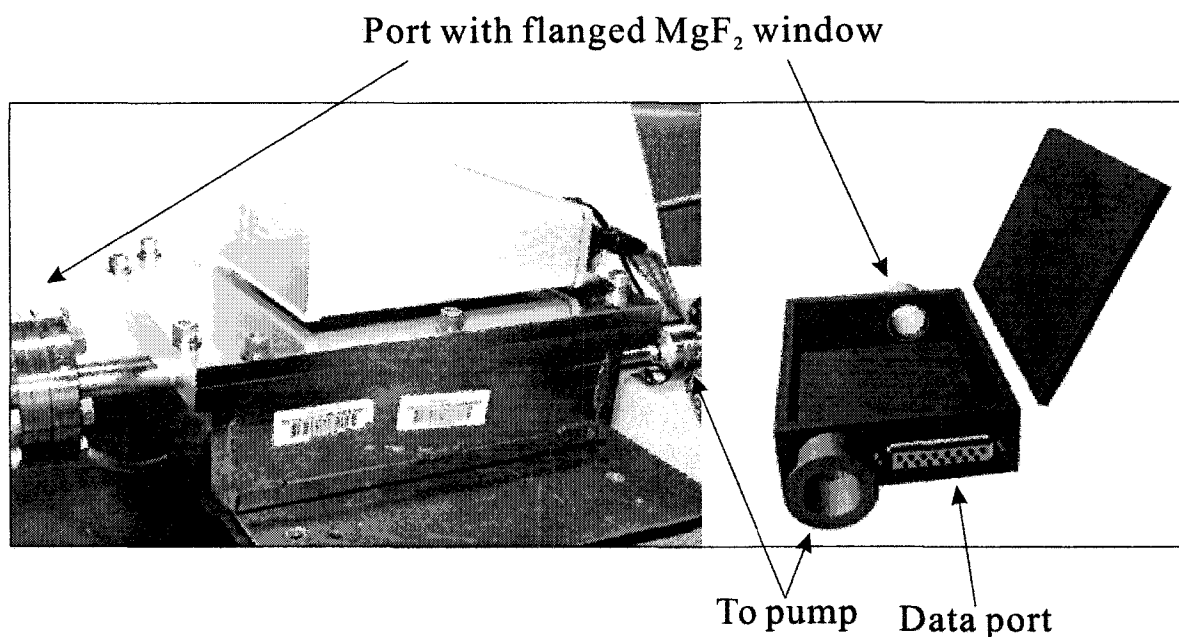
Figure 3.9: Portable VUV spectrometer based on OceanOptics S1024DW (160 nm to 300 nm). The spectrometer is put inside a stainless steel cavity, shown in the cartoon on right side. The unit on top of the cavity (SAD500) is the A/D converter that communicates between the spectrometer and a computer.The dimension of this unit are $22 \times 15 \times 10$ cm. Its total weight is 10.5 kg, including the power supply, making it suitable for airborne applications

Because UV is strongly absorbed by air below 200 nm, we built a vacuum cavity for

the spectrometer. Fig. 3.9 shows a cartoon for the stainless cavity and a photograph

of the system on site, excluding pumps. The white unit on top of the cavity is

the A/D converter installed between the spectrometer and a computer. It helps

digitize data and control the communications. Because most fiber optic cables do

not transmit below 190 nm, there must be a free-beam light delivery system. This

includes a flanged MgF_2 window right in front of the slit and an 8 mm ID suprasil

tube evacuated to $\sim 10^{-5}$ torr and connected to the lamp system.
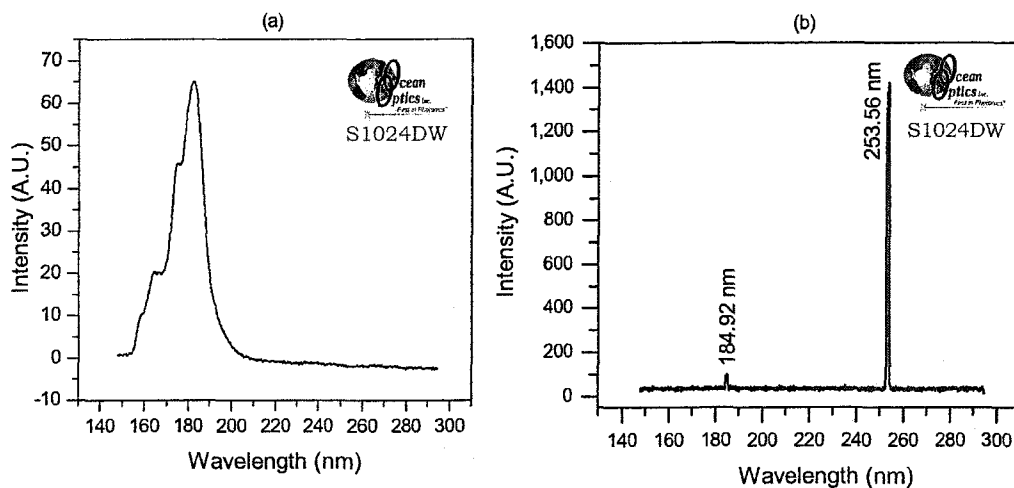
Figure 3.10: VUV response of the portable spectrometer based on OceanOptics S1024DW:
a. Xe second continuum with 700 torr and 180 watt rf; b. mercury calibration lamp

This system has been wavelength calibrated by an Hg-Ar wavelength calibration

lamp from Oriel Instruments. Fig. 3.10(a) is a spectrum of the Xe second continuum.

Although this spectrum shows that this portable system is responsive all the way down

to 155 nm, we see some evidence of absorption, possibly from air, the optical surface,

or both. We used a 4 foot long elbow (5/8 inch in diameter) to connect the vacuum chamber to the pumping system. For such long tube pumping, the conductance is

$$C = 3.81(T/M)^{1/2}\frac{D^3}{L} \; l/s \qquad (3.1)$$

where T is the temperature in Kelvin, M is average mass in AMU, D and L are measured in centimeters, representing the tube diameter and length respectively. For air at room temperature (20°C),

$$C = 12.12\frac{D^3}{L} \; l/s \qquad (3.2)$$

Using the size of the tube on above, we obtain a conductance $C = 0.74$ l/s. Assuming the pumping speed at the measuring point is the pumping speed of the pump (S_p=7.5 l/s), since they are very close, the pumping speed at the connecting port of the chamber can be estimated by the following formula,

$$\frac{1}{S_c} = \frac{1}{S_p} + \frac{1}{C} \qquad (3.3)$$

resulting in the pumping speed in the chamber S_c=0.67 l/s.

The throughput $Q = SP$ is conserved if no additional gas leaks into or is removed from the pipe between the points of interest, so we have

$$P_c = \frac{S_p}{S_c}P_p \qquad (3.4)$$

So, the pressure (P_p=10^{-5} torr) measured at the far end, results in a base pressure estimated to be 1.1×10^{-4} torr inside the vacuum chamber. C. M. Van Atta's book [42]

describes these relationships under various conditions in chapter 2 and the reader is directed to that source for further information.

This spectrometer was modified from a commercial version which has a wavelength cutoff at 200 nm. Although the window on top of the PDA was removed to improve UV sensitivity, the PDA itself is not calibrated below 200 nm. Taking the pointwise log of the ratio of this spectrum in Fig. 3.10(a) to that obtained in the larger system (McPherson 218) operating below 10^{-6} torr, fitting the long wavelength shoulder where no absorption is assumed, yields the absorption coefficient curve shown in Fig. 3.11. This curve is the characteristic curve of the unit's response in VUV, which can be used to calibrate the output intensity down to 155 nm.

$$\alpha = -\ln \frac{I_{OceanOptics}}{I_{Mcpherson}}$$
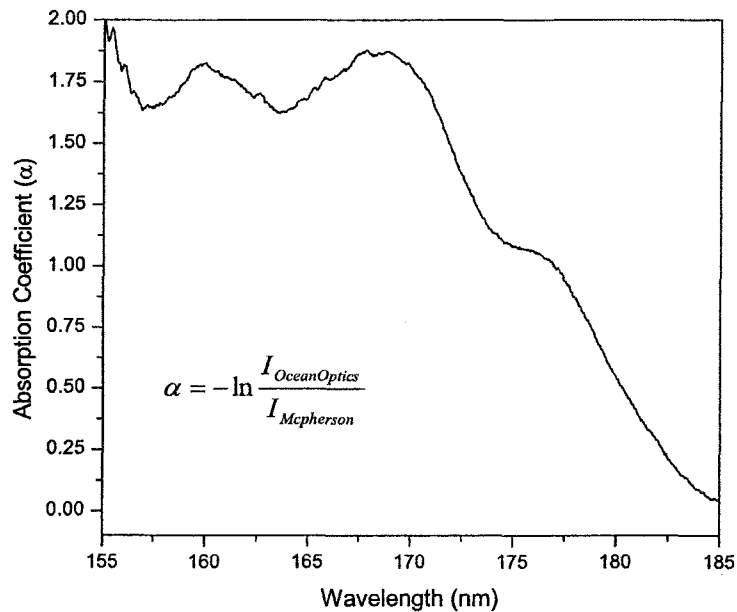
Figure 3.11: Characteristic curve for the absorption coefficient of the VUV compact spectrometer between 155 - 185 nm

Fig. 3.10(b) is a spectrum of an Hg-Ar calibration lamp taken in the compact system. The ratio of the two Hg I line intensities at 253.65 nm and 184.95 nm is 20:1, which is close to NIST traceable calibration data (15:1). This indicates that the absorption does not affect that line ratio very much at wavelengths where transitions were observed. The vacuum level of this system can be easily improved by improving the conductance of the external connections, and this problem can be easily overcomed for applications that require working below 185 nm.

3.6 Calibration

The larger spectrometer was very carefully intensity-calibrated from 200 nm to 320 nm with an deuterium lamp (Oriel Instruments model 63345) with a known spectral irradiance whose calibration is traceable to NIST secondary standards. We follow the prescription of Ametepe [34] to transfer the intensity calibration to the range 160 - 200 nm, where manufacturer's calibration data is not available, the extrapolation technique [43] of Saunders, Ott, and Bridges was employed. In this technique, the normalized spectral radiance (sum of all of the angular distribution of radiation over a specified solid angle) of the deuterium lamp was measured and compared to the normalized irradiance data (the radiant flux per unit area onto a specified surface) supplied by the factory from 200 to 320 nm. Plotting the two data sets on the same wavelength and intensity scale resulted in a root-mean-square deviation of about 1% in the overlap region. Since the wavelength distribution of the spectral radiance is

nearly the same as that of the spectral irradiance, extrapolation of the deuterium lamp spectral irradiance curve down to 160 nm is justified [43, 44, 45]. Saunders has shown that this procedure is in agreement with direct calibration using synchrotron, plasma blackbody, and wall-stabilized arc primary and secondary standards.
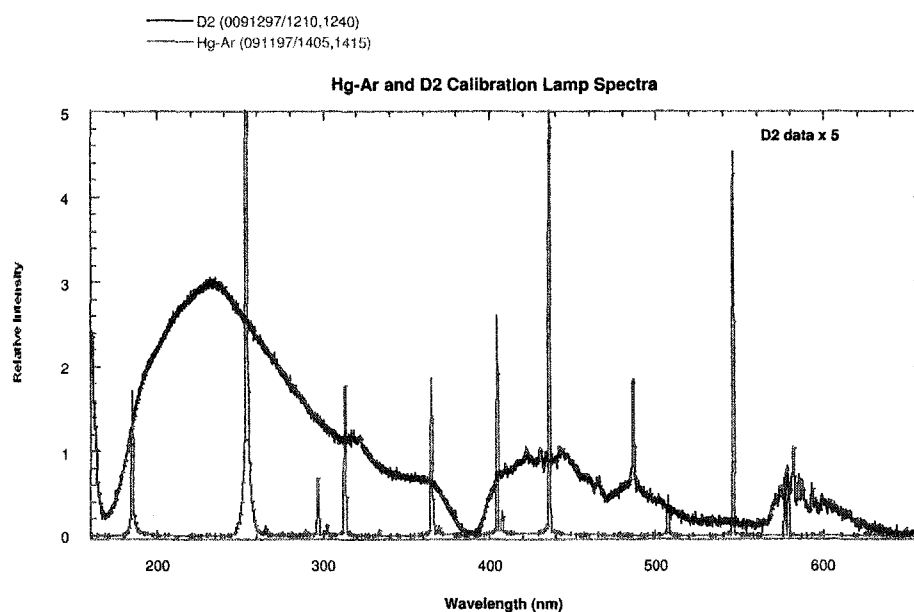
Figure 3.12: An Oriel Hg-Ar calibration lamp spectrum superposed on an Oriel D_2 calibration lamp over the wavelength range of 160 nm to 660 nm

As a secondary check, our calibration results were applied to data obtained from Hg-Ar wavelength calibration lamp yielding the expected line ratios for 185 and 253 nm Hg (see Fig. 3.12). We routinely wavelength calibrate our spectrometer for each group of spectra taken using Hg line radiation sources. Our λ values for the Hg-Ar lamp are consistent with data supplied by the factory. Both spectra of Fig. 3.12 indicate our spectrometer's sensitivity below 200 nm.

3.7 Data Acquisition
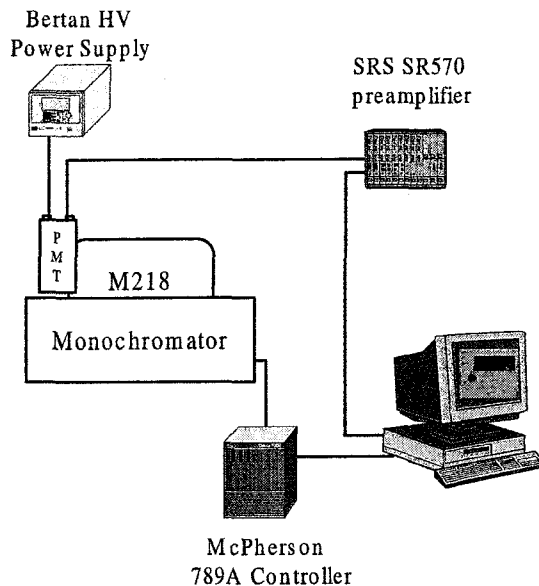
Figure 3.13: Diagram for the data acquisition system

The data acquisition and control system (Fig. 3.13) consists of a detector (PMT R928), a preamplifier, a spectrometer controller (McPherson 789A), and an analog-to-digital converter (ADC) with voltage reference. The PMT powered by a Bertan HV power supply at 900V has a typical gain of about 6×10^6. We use a current preamplifier (Stanford Research System SR570) to amplify the signal and send it to an ADC board (National Instruments PC-LPM-16). SR 570 has an excellent built-in filter, which greatly improves the signal to noise ratio (SNR).

The graphic oriented acquisition program was written in Labview based on the previous version. In order to increase SNR further, the new program averages every 50 data to get one point value. This is reasonable given careful consideration of the

sampling rate of the DAQ board, and the spectrometer system resolution, without losing the accuracy of data.

Chapter 4

Spectroscopic Analysis

Optical spectroscopy has been one of the most important techniques in plasma characterization. In this chapter, we start from spectroscopy of xenon excimers generated in our RF lamp. Some conditions that affect the total emission efficiency are discussed. As a core part of this study, we systematically studied KrI excimers in pressure range of 200 to 1500 torr with two different mixtures. The intensities of the 225 nm KrI* and 342 nm I_2* emissions increase with pressure in the range 200 to 800 torr, while the intensity of the 191 nm KrI* emission remain slightly decreases. We developed a simple kinetic model to explain the observed KrI* and I_2* pressure dependence. This work may provide valuable experimental information in the high pressure regime for obtaining accurate potential energy curves to determine the vibrational distribution in the emitting states for the rare gas halides. In addition, some other excimers which emit strongly in UV region are reported and discussed.

64

4.1 Emission Spectra of Xenon Excimers

4.1.1 Homonuclear Diatomic Molecule

Rare gas (Rg) homonuclear diatomic molecules have been a subject of interest since 1970's due to their importance as intense sources of UV radiation. Molecular potential curves for both neutrals [46, 47, 48] and ions [49] are well established. In general, the lowest excited molecular state is bound, while the ground electronic state is repulsive, or very weakly bound, with a shallow van der Waals minimum. We use xenon to demonstrate the general features of molecular potential curves for Rg homonuclear diatomic molecules. Potential curves for Ne_2, Ar_2, and Kr_2 and their ions formed in the presence of varying degrees of spin-orbit coupling are roughly similar to those shown below for Xe_2 and Xe_2^+ [50].

To the extent that the ground states of the Xe atom and ion can be described by single-electron-configuration wavefunctions, following the notation of C. E. Moore [51], the electron configuration of the ground and the ^3P excited states of the xenon atom are [52]

$$\cdots 5s^2 5p^6, (^1S_0)$$

and

$$\cdots 5s^2 5p^5 6s, (^2P_{2,1,0})$$

At relatively high pressure, when atoms are in proximity, their resonance lines
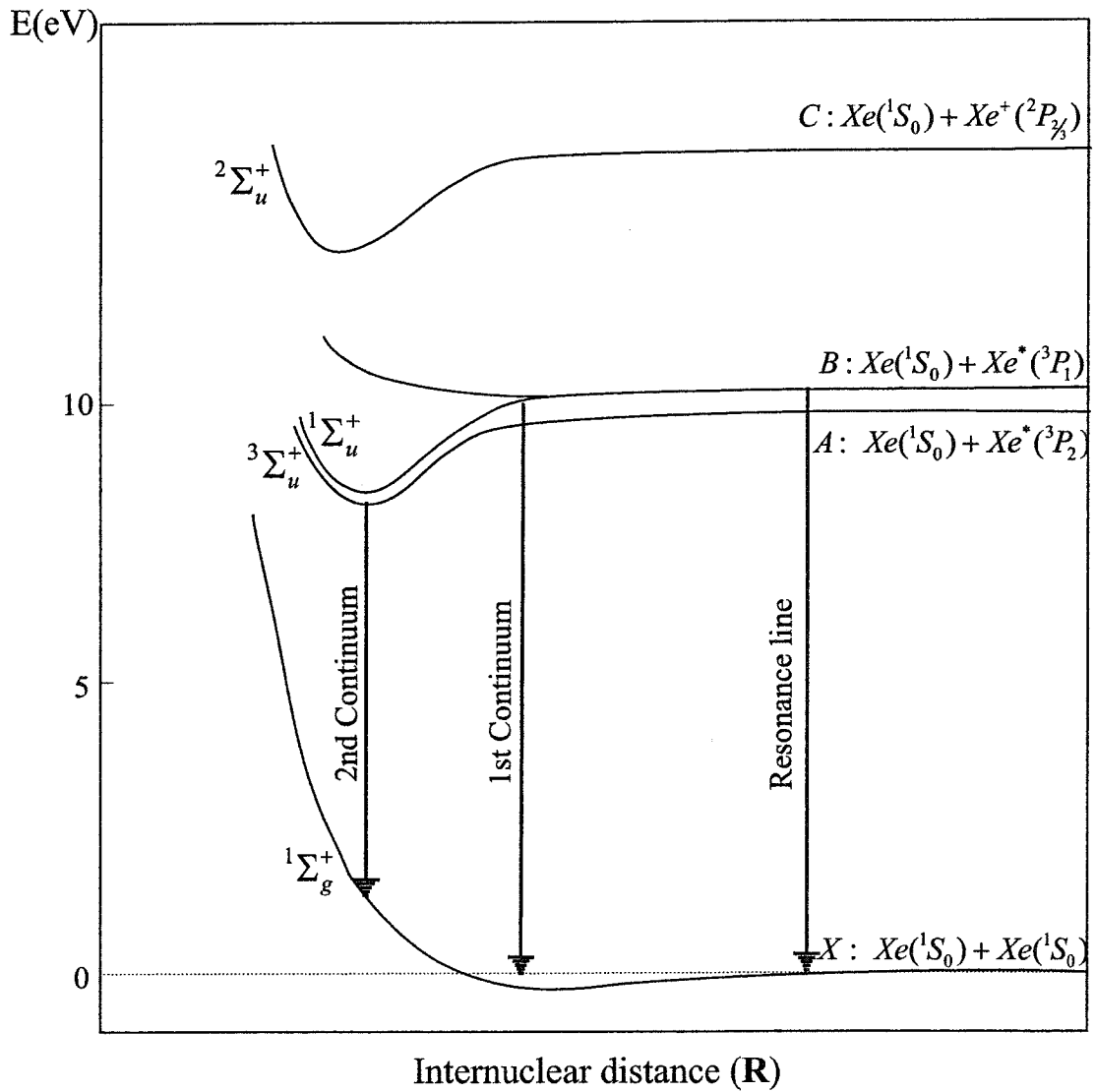
Figure 4.1: A simplified potential energy diagram identifying the excited atomic and molecular levels of xenon

are broadened by electronic interactions. In pure rare gases, continuous VUV emissions arise from transitions between the bound $^3\Sigma_u^+$ ($^3P_2+^1S_0$) and $^1\Sigma_u^+$ ($^3P_1+^1S_0$) molecular excited states and the dissociative ground state $^1\Sigma_g^+$ ($^1S_0+^1S_0$), generally repulsive [50, 53] (see Fig. 4.1). These interaction potentials are usually represented by Morse functions. By varying parameters in these functions, one can obtain a best fit between the experimental data and the integral of the transition dipole moment, which yields accurate potential curves for Ar_2^*, Kr_2^* and Xe_2^* in P. Dubé's work [54].

	Ar	**Kr**	**Xe**
Atomic ionization energy (eV)	15.755	13.996	12.127
2nd continuum (nm)	126	148	172
Photon energy (eV)	9.85	8.5	7.2
$^3\Sigma_u^+$ life time for $\nu=0$ at 300 K (ns)	3000	280	104
ω_e for $^3\Sigma_u^+$ (cm^{-1})	299	183	116
D_e for $^3\Sigma_u^+$ (cm^{-1})	6200	4950	3750
R_e for $^3\Sigma_u^+$ (Å)	2.35	2.61	3.00

Table 4.1: Peak wavelengths and energy for excimers generated by pure noble gases

For xenon, the second continuum is mainly produced by the transitions ($^1\Sigma_u^+$, $^3\Sigma_u^+$)$\rightarrow^1\Sigma_g^+$ of the Xe_2^* molecule. A triplet-to-singlet transition is prohibited by the intercombination selection rule which is quite strict for light atoms and molecules. This is consistent with the much longer lifetime ($\sim$100 ns) for $^3\Sigma_u^+$ compared to ($\sim$5 ns) for $^1\Sigma_u^+$ state [55, 56]. The resonance line from $^3P_1$ to $^1P_0$ usually marks the blue side edge of the first continuum, ie. 147 nm for xenon. At a pressure of 15 torr, the

first continuum for xenon extends to 146 nm, which implies that the ground state,

$^1\Sigma_g^+$, has a small van der Waals minimum at least 470 cm^{-1}(0.058 eV) [57] deep. In

the Ar_2^* simulation work of Dube $et\ al.$ [54], better agreement with observed emission

was obtained by incorporating a shallow van der Waals minimum of 100 cm^{-1}(0.012

eV) in the ground state.

4.1.2 Kinetic Reactions for Xenon

For pure rare gas excimer formation, electrons of at least 8 to 25 eV energy are needed

to create excited atoms (Rg*) and ions (Rg$^+$). Usually high pressures in the range of 1

bar are needed to prevent deactivation of these excited atoms and ions before excimer

formation can take place. The high operating pressure allows for some simplification

of the kinetic processes since collisions tend to vibrationally and electronically relax

to only a few states.

The mechanism for populating certain excimer states and emitting photons is

made by a sequence of elastic collisions with energy exchanges. The schematic di-

agram of this sequence is shown in Fig. 4.2. When external energy is applied, the

electrical power is coupled most efficiently to the plasma electrons and not to the

ions. These heavy particles gain energy from energetic electrons to populate their

excited states.

$$e^- + Xe \rightarrow Xe^* + e^- \tag{4.1}$$
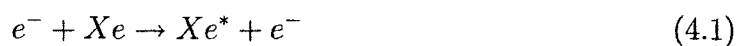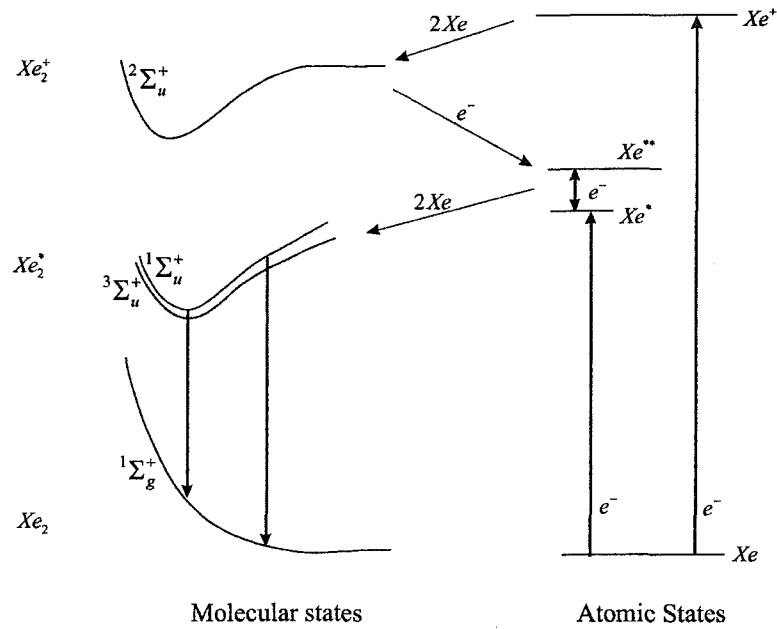
Figure 4.2: Simplifed mechanism for radiation from excimer states

$$e^- + Xe \rightarrow Xe^+ + 2e^- \tag{4.2}$$

The electrons have to be energetic enough, i.e. the collisional cross section ≥ 0, to excite atoms from their ground states. For Xe, the electron threshold energy is 8.32 eV [58]. The secondary electrons produced from Eq. 4.1 and 4.2 have a mean energy of 5 to 7 eV [55].

The atomic excited state $Xe^{**}(^1P)$ can be populated from $Xe^*(^3P)$ or from the ground state $Xe(^1S_0)$ directly.

$$Xe^* + e^- \rightarrow Xe^{**} + e^- \tag{4.3}$$

A deactivation process between these two resonant states will release a photon in

the infrared (IR) at 823 nm and 828 nm.

$$Xe^{**} \rightarrow Xe^{*} + h\nu \tag{4.4}$$

The excited molecular ion state Xe_2^{+} is populated by a rapid three body association.

$$Xe^{+} + 2Xe \rightarrow Xe_2^{+} + Xe \tag{4.5}$$
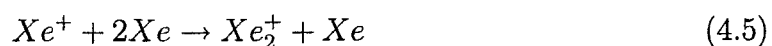
The rate constant for this reaction is usually greater than $10^{-31}\text{cm}^6\text{s}^{-1}$ [59], and it is generally followed by a quick dissociative recombination reaction, which forms an excited neutral dissociating state.

$$Xe_2^{+} + e^{-} \rightarrow Xe^{**} + Xe \tag{4.6}$$

The typical rate constants for this process are $10^{-6}\text{cm}^3\text{s}^{-1}$. It is assumed that the vibrational relaxation is rapid prior to recombination. Then at high pressure, rapid three-body reactions, typically at the rate of $10^{-32}\text{cm}^6\text{s}^{-1}$, lead to formation of bound molecular states $Xe_2^{*}({}^1\Sigma_u^{+}$ and ${}^3\Sigma_u^{+})$.

$$Xe^{**} + 2Xe \rightarrow Xe_2^{*} + Xe \tag{4.7}$$

In the radiative decay of noble gases, the two low-lying excimer states ${}^1\Sigma_u^{+}(0_u^{+})$ and ${}^3\Sigma_u^{+}(1_u, 0_u^{-})$ are responsible for radiations. Several studies have been made to study the decay rate of these two excimer states for xenon and other noble

gases [60, 61, 62, 63, 64]. But experiments have shown only one instead of two decay rates. Keto et al [65] carefully measured these rates, and indicated the mixture of the molecular states. The net effect of decay time in experiments is consistent with the calculation when one assumes the fractional populations of the triplet and singlet excited state are 3/4 and 1/4, which yields a decay time of 19 ns [55] for xenon.

Electrons are important in mixing these excimer states. When the electron density gets high, super-elastic electron collisions also enhance electronic relaxation. However, this process can deplete the population inversion by causing transitions to the ground state, which is one of the important mechanisms for electron heating.

4.1.3 Xenon Spectra and Lamp Efficiency

Visual observations of our xenon lamp show emission changes. At very low pressures, below several torr, the discharge displays a diffuse, "foggy" character. In this regime, the spectrum is dominated by atomic resonance lines. As pressure increases, molecular bands appear. In the VUV region, a band with the edge marked by the resonance line at 147 nm, so called the first continuum becomes dominant. As the pressure further increases we observe numerous irregular discharge filaments undulating within the foggy background. The second continuum, at around 172 nm, also arises. These filaments dominate the emission, causing the lamp to appear bright white. At pressures above 900 torr, the filaments coalesce into one or two thin super-bright filaments which appear to "stick" to the side of the bulb wall as stabilized arcs. Vibrational

structures are completely washed out in spectra taken above 900 torr.

Fig. 4.3 shows all the emissions observed between 150 nm and 900 nm from the pure xenon gas discharge. At this medium pressure, all the transitions observed are atomic transitions in the IR wavelength region. The two most intense lines, at 823 nm and 828 nm are identified as the transitions associated with $2p_6[6p(3/2)_2][^1D_2] \rightarrow 1s_5[6s(3/2)_2][^3P_2^0]$ and $2p_5[6p(1/2)_0][^1P_1] \rightarrow 1s_4[6s(3/2)_1][^3P_1^0]$ respectively.
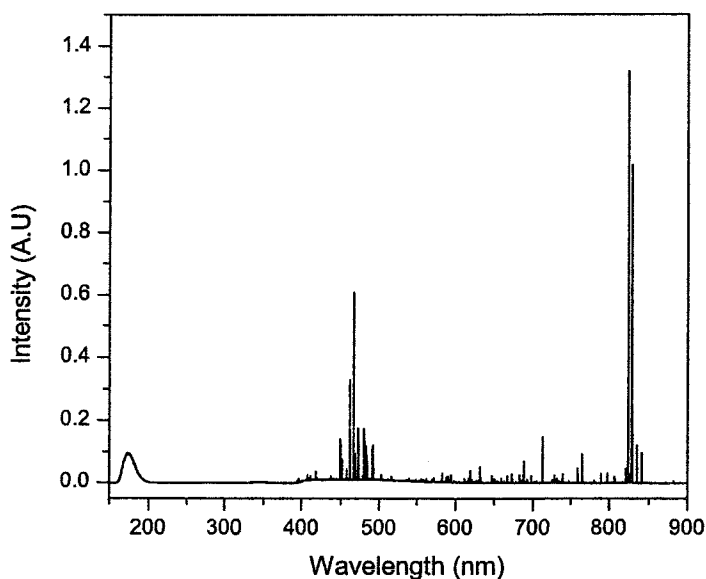
Figure 4.3: The full spectrum of a xenon discharge taken from the RF lamp with 90 watt RF power and at pressure 400 torr.

When either the input RF power or the gas pressure increases, a broad band from 400 nm to 700 nm appears with atomic lines sitting on top of it. Fig. 4.4 illustrates the effect of increasing RF power from 70 Watt to 230 Watt. When pressure increases, similar behaviors are observed.
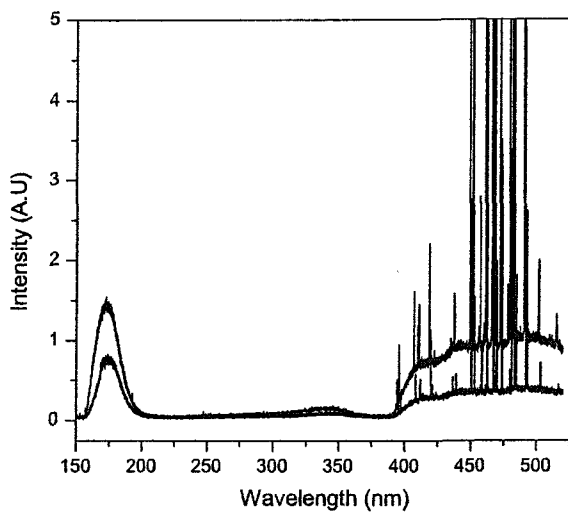
Figure 4.4: Emission spectrum of pure xenon at 850 torr in UV-Vis. When RF power increases from 70 watts to 230 watts, both intensities of the broad band in VUV and visible are more than doubled

Much attention has been paid to the study of the VUV continua for xenon [66, 67]. The Xe 147 nm first continuum dominates the emission spectrum at low pressures (<100 torr). The second continuum, peaking at 172 nm, dominates the spectrum at pressures higher than 300 torr.

A typical xenon VUV spectrum obtained in our RF capacitively coupled lamp is shown in Fig. 4.5. A deuterium lamp (Oriel BJ2775, NIST-traceable, secondary calibration source) was used for intensity calibration according to the procedure detailed in appendix C. Integrating the total light output from 150 nm to 220 nm, and comparing the power emitted to the input rf power, we obtain a lamp efficiency of about 33% for xenon excimer at 600 torr and 140 watt RF input power. The lamp efficiency varies with gas pressure and RF power. However, in most of our xenon experiments,
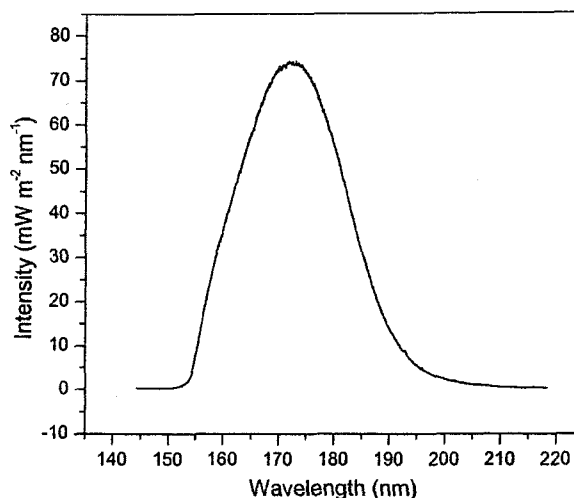
Figure 4.5: Xenon excimer second continuum at 600 torr in the RF lamp with 140 watt input power

we obtained lamp efficiencies between 20% and 40%, which compares favorably to the 40% efficiency (close to the theoretical maximum) reported by Ametepe et. al. [68] for our high-pressure microwave lamp.

These excimer emissions strongly depend on gas pressures. This follows from collisional relaxation since high vibrational states of the 0_u^+ and 1_u bound states lead to the first continuum emission around 147 nm, whereas the low vibrational states lead to the second continuum emission at 172 nm [66]. The second continuum is thus favored at high pressures due to the fast vibrational relaxation [69] compared to the rate of radiative decay.

We carefully studied the pressure and temperature dependence of peak intensities of the xenon lamp. The monochromator was set to accept only emission at around 172
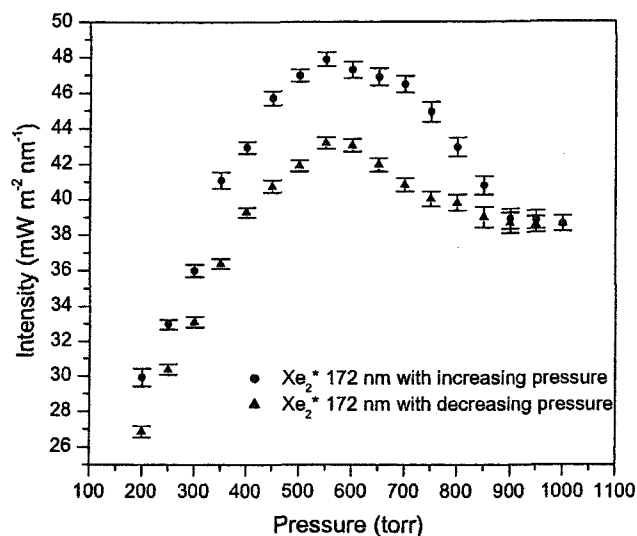
Figure 4.6: The peak intensity of xenon excimer emission at 172 nm vs. gas pressure with 100 watt RF input

nm. After each pressure change, a sufficient number of data points were recorded to get an average value of the intensity. As shown in Fig. 4.6, the second continuum peak intensity increased rapidly with increases in lamp plenum pressure. This increase does not continue indefinitely, however, because at extremely high pressure electron-neutral collisions sufficiently cool the electron temperature, depleting the population of the excimer upper states $^1\Sigma_u^+(0_u^+)$ and $^3\Sigma_u^+(1_u, 0_u^-)$. The peak intensity will drop and reach an asymptotic value. Thus there is a maximum in the observed intensity, which occurs around 600 torr. The dependence on neutral species density is confirmed by our studies of the temperature dependence, and on our model for the emission which we will discuss later in this chapter.

As seen in Fig. 4.6, the intensity does not retrace the same curve observed for in-
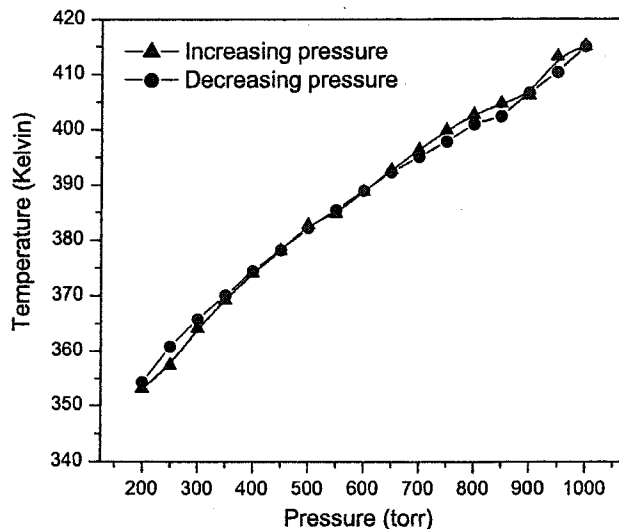
Figure 4.7: The pressure dependence of the temperature measured from the outside of the xenon lamp with 100 watt RF power

creasing pressure that we observe when decreasing the pressure. Initially, we thought this might be simply the result of a persistent difference in gas temperature in the bulb, reducing the effective particle density for a given measured pressure. To test this, we monitored the temperature of the suprasil bulb jacket at the longitudinal position of the observed light emission for each value of operating pressure. Fig. 4.7 indicates: (1) the temperature is the same for each value of the pressure (within the limits of error of our measurements), independent of the direction of change; (2) beyond the maximum in emission vs. pressure, the temperature continuously increases with pressure. This would lead us to expect a maximum lamp efficiency near the maximum of the I vs. p curve, that is, near 600 torr for pure xenon. Thus, 100 watt xenon lamps operating at pressures greater than 600 torr are generally less efficient,

with much more heat released. We are left to speculate that the observed hysteresis might result from slow changes resulting from photochemistry on the interior of the suprasil bulb jacket during lamp operation. Such "conditioning" effects are rarely explained in detail, although they are very common observed in many plasma-driven systems.
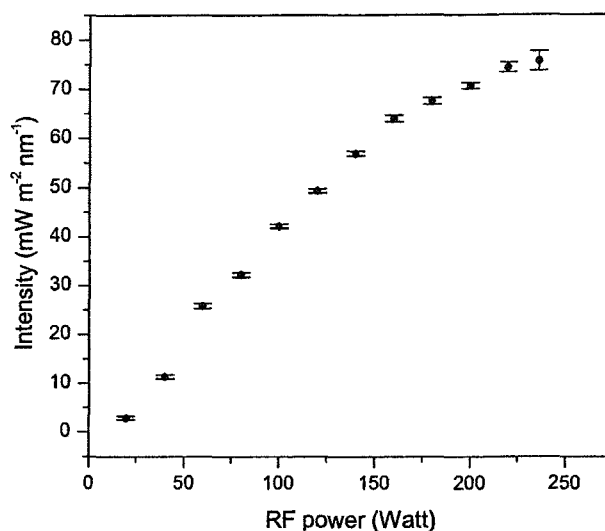
Figure 4.8: The peak intensity of xenon excimer emission at 172 nm vs RF power at 800 torr

The peak intensity increases with the input RF power. At a pressure of 800 torr, the dependence is slightly non-linear, as seen in Fig. 4.8. The bulb temperature, however, changes more linearly with the RF power as seen in Fig. 4.9. The nearly-linear behavior of intensity and temperature implies that changing RF power will not change the lamp efficiency significantly up to about 200 watts of RF input power, but beyond that level, the efficiency will drop.
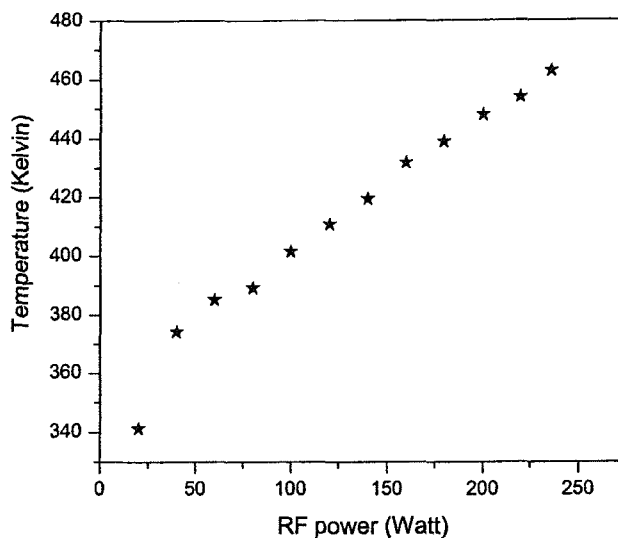
Figure 4.9: The RF power dependence of the temperature measured from the outside of the xenon lamp at 800 torr

4.1.4 Plasma Temperature Estimate

The excimer emission band intensity is proportional to the integral of the product of the dipole moment and the population distribution function. It is usually a very good assumption to assume a Boltzmann temperature distribution function. So, the shape of an excimer emission band should strongly depend on the temperature. Cheshnovsky et al. [70] performed an experimental study of the temperature dependence of emission spectra of diatomic Rg molecules, and derived an empirical formula which relates the emission line width with the discharge temperature. They found:

$$\Delta = \Delta_0 [coth(\hbar\omega/2k_BT)]^{1/2} \tag{4.8}$$

where Δ_0 is the line width in the limit $T \to 0$. Unknown parameters are determined by nonlinear fitting, which yields for xenon.

$$\Delta = 2550[coth(100/T)]^{1/2}$$ (4.9)

In Eq. (4.9), the line width is given in cm^{-1} units, and $\Delta_0 = 2550 \pm 100$ cm^{-1}.

Pressure(torr)	FWHM (cm^{-1})	T_1 discharge (K)	T_2 outside (K)
200	7528.3	868±73	353
400	7853.1	945±79	374
600	8012.9	984±82	389
800	8134.4	1014±85	403

Table 4.2: Temperature dependence of Xe_2^* in the vacuum ultraviolet
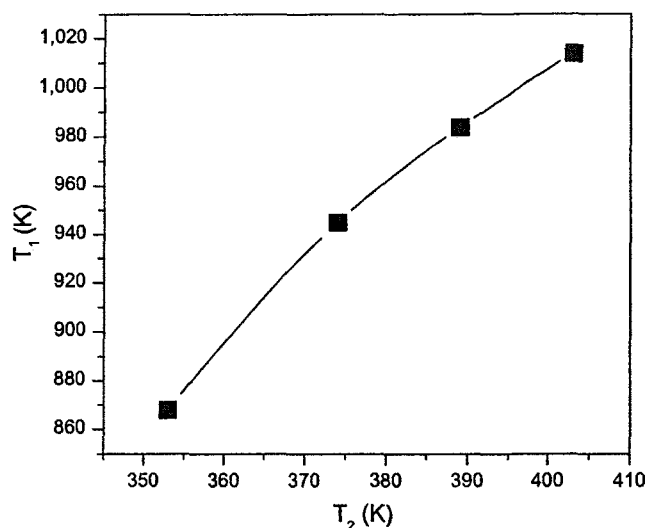
Figure 4.10: Temperature relationship: T_1 is the temperature of neutral gas estimated from the emission line width, T_2 is the measured temperature on the outer wall of the bulb

Table 4.2 lists the estimated gas temperatures obtained from Eq. (4.9) for xenon discharges using and the temperatures measured on the outer wall of the bulb at

different pressures. In Fig. 4.10, we present the relationship between these two temperatures. With the assumption of constant cooling conditions, one may use this plot to determine the gas temperature of other discharges from a simple temperature measurement of the bulb jacket. This depends on assuming that thermal conductivities of the gas mixtures in the discharge are approximately constant. This is not a particularly good approximation, but will suffice for yielding the zero-order engineering estimates we need below.

We have undertaken a simple engineering analysis of the heat flow for our system. The thermal conduction equation is

$$\dot{Q} = \frac{dQ}{dt} = -(\frac{A}{d})\,k\nabla T \tag{4.10}$$

where A is the cross-sectional area, d is the thickness, k is the thermal conductivity of the medium, and $\dot{Q}$ is the time derivative of the heat content.

Fig. 4.11 shows a cross section of a cylindrical shell with inner radius a and outer radius b. We represent the bulb as a hollow cylinder of radius $a < r < b$ and length l. On a given radial surface, selected at r, the temperature is $T(r)$. The temperatures on the inner and outer boundaries are held constant at T_1 and T_2 respectively. The most important assumption we make, and the one most likely to need major revision in a higher order model is that we only consider a steady flow in the radial direction. Less restrictively, we assume that k is constant. Since the heat flow along the longitudinal
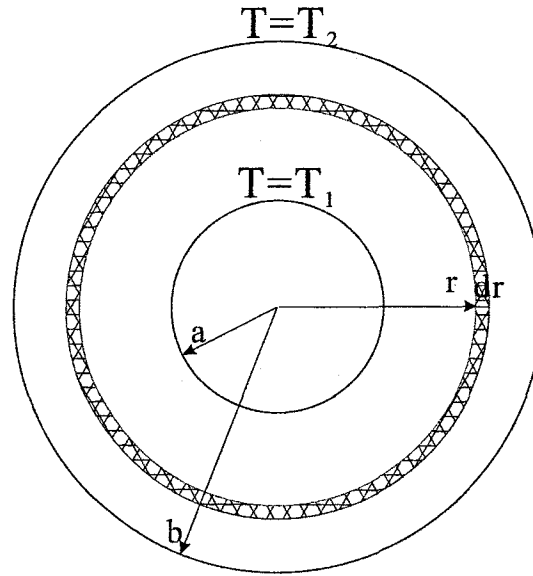
Figure 4.11: Cross section view of a cylindrical tube to display a radial heat flow

axis of the cylinder is ignored, the gradient of T reduces to a single term:

$$\nabla T = \vec{e}_r \frac{dT}{dr} \tag{4.11}$$

where $\vec{e}_r$ denotes a unit vector in the radial direction.

According to Eq. (4.10), we have

$$\dot{Q} = -k \cdot 2\pi l \frac{r}{dr} dT \tag{4.12}$$

Then from

$$\int_{T_1}^{T_2} dT = -\frac{\dot{Q}}{2\pi lk} \int_a^b \frac{dr}{r} \tag{4.13}$$

we have

$$\dot{Q} = \frac{2\pi lk}{\ln \frac{b}{a}} (T_1 - T_2) \tag{4.14}$$

The term k for fused silicon is $k_{qz} = 1.4$ W/mK and the length of discharge, $l = 0.5$m. The estimates we have made above for T_1 are estimates of the discharge temperature. Compared to the temperature at an infinitesimal distance inside the inner surface of the suprasil bulb, T_1 might be a few hundred degrees higher.

We have noted above that at high pressures, there are several rapidly moving discharge filaments inside the bulb. Although these filaments connect to the bulb surface occasionally, we will here assume that heat is transferred to the bulb mostly by conduction through the neutral gas. Refining the calculation much beyond this, to take into account neutral gas convective effects (Newtonian transfer) is not profitable however, since for the moment we are ignoring power transfer from charged particles transiting the sheath boundaries at the edge of the plasma. This form of charged particle transfer, especially electron conduction along the longitudinal direction for the locally twisted filaments, is far too difficult to model in this context. However, we expect that it is not an insignificant source of heat transfer.

For this moment, let us assume that the thermal conducting net effect can be schematically represented as shown in Fig. 4.12, where discharge filaments are confined in the central core of the bulb to a column with radius $a = 3$mm. Heat generated from the discharge in this zone is then transferred by the neutral gas xenon, then in series through the bulb jacket, to the outer wall of the bulb. The inner radius b and outer radius c are 4mm and 5mm respectively.

The steady state heat flow equation Eq. (4.14) has the same form as Ohm's Law
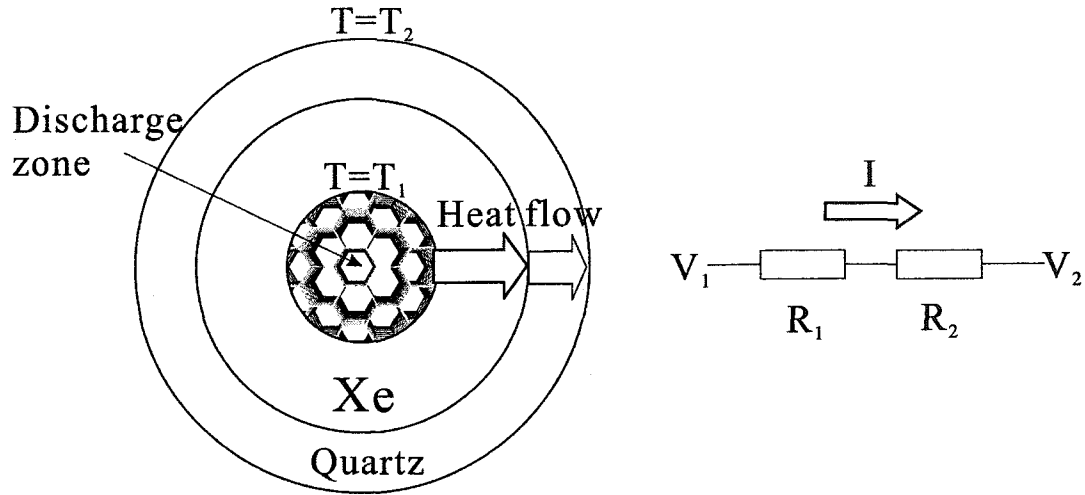
Figure 4.12: Electrical analogy for heat conduction in a cylindrical discharge tube by radial flow

for current flow through resistors in series,

$$I = \frac{1}{R}(V_1 - V_2) \tag{4.15}$$

The thermal resistance can be defined as

$$R_T = \frac{ln(b/a)}{2\pi l k} \tag{4.16}$$

We can solve by writing:

$$\dot{Q} = \frac{2\pi l}{ln\frac{b}{a}/k_{Xe} + ln\frac{c}{b}/k_{qz}}(T_1 - T_2) \tag{4.17}$$

where $k_{Xe} = 0.00569$ W/mK. Taking the temperature data from table 4.2 for a pressure of 600 torr xenon discharge, a heat flow of about 37 watts is obtained for

100 watts of rf input. Longitudinal losses comparable to this radial loss, associated with the high electron thermal conductivity of the filamentary column must also be present. There also is direct blackbody radiation from the optically thick (or at least not optically thin) hot gas column itself, serving to produce an infrared radiative loss. Together these losses account for the observed values of light efficiency produced in our lamp.

4.2 Emission Spectra of KrI Excimers

In this section, we report and analyze the KrI^*/I_2^* emission spectra over the wavelength range 160 nm - 360 nm generated in our novel capacitively coupled 13.56 MHz RF lamp. As for the Xe case, the total gas pressure strongly influences the emission efficiency. Over the pressure range studied, the intensities of the 225 nm KrI^* and 342 nm I_2^* emissions increase with increasing pressure, while the intensity of the 191 nm KrI^* emission is weak and decreases slowly with pressure. We present below a simple kinetic model that we developed to explain the observed KrI^* and I_2^* pressure dependence. The details of spectral analysis of our high resolution data may yield valuable experimental information from which accurate potential energy curves may be extracted, and these data may further allow predictions of the vibrational distributions of the rare gas halide emitting states.

4.2.1 Rare Gas Halides

Reactions of electronically excited Rg atoms with halogens or with reagents containing halogens lead to the formation of Rg halide excimer molecules [15, 33, 71, 72, 73, 74]. From previous studies of excimers by other groups [73, 75, 76], there are, in general, three low-lying states denoted in the light-atom, Hund's case b as $X^2\Sigma_{1/2}$, $A^2\Pi_{3/2}$, and $A^2\Pi_{1/2}$ and three closely spaced excited states $B^2\Sigma_{1/2}$, $C^2\Pi_{3/2}$, and $D^2\Pi_{1/2}$. The lower states ($X_{1/2}$, $A_{3/2}$, and $A_{1/2}$) are well-represented as unbound covalent states and the upper states ($B_{1/2}$, $C_{3/2}$, and $D_{1/2}$) are represented as ion-pair states, having high bond ionicity [16, 77, 78, 79]. The $X^2\Sigma_{1/2}$ (ground) state correlates to separated atoms corresponding to the ^1S state of the Rg and to the ^2P state of the halogen. The upper state correlates to a positive Rg ion $Rg^+(^2P)$ and a negative halogen ion $X^-(^1S)$. At close internuclear distances, the low-lying ^2P state of the halogen splits due to spin-orbit coupling to correlate with the $^2\Sigma_{1/2}$ and $^2\Pi_{1/2,3/2}$ states.

In the case of KrI* (Kr: $4s^2\ 4p^6$ and I: $5s^2\ 5p^5$), the $X^2\Sigma_{1/2}$ state arises from the ^1S ground state of Kr and the ^2P ($l = 1$, $m_l = 0$, $s = 1/2$) state of the iodine atom. The $A^2\Pi_{1/2}$, and $A^2\Pi_{3/2}$ states arise from the ground ^1S state of the Kr atom and the spin-orbit splitting of the ^2P ($l = 1$, $m_l = \pm 1$, $s = 1/2$) level of the iodine atom, thus at large internuclear separation, the energy of the $A^2\Pi_{3/2}$ state lies below the energy of the $A^2\Pi_{1/2}$ state by approximately the energy of the iodine atom spin-orbit splitting. The upper states are formed from the ^2P Kr^+ and ^1S I^- ions to correlate to

the $B^2\Sigma_{1/2}$, $C^2\Pi_{3/2}$, $D^2\Pi_{1/2}$ states. Calculations by Velasco et al. [80] show that the

$D^2\Pi_{1/2}$ state is at higher energy, corresponding to the spin-orbit splitting of the Kr^+

ion. The minimum of **B** state is estimated to be at 3.2 Åfor KrI, as determined from

an ionic model by Ewing et al. [79]. Previous studies [75, 81] of Rg halides described

several optical transitions occuring between the upper $(B^2\Sigma_{1/2}, C^2\Pi_{3/2}, D^2\Pi_{1/2})$ and

the lower $(X^2\Sigma_{1/2}, A^2\Pi_{3/2}, A^2\Pi_{1/2})$ states. In general, four allowed transitions [82]

$D^2\Pi_{1/2} \rightarrow X^2\Sigma_{1/2}$, $B^2\Sigma_{1/2} \rightarrow X^2\Sigma_{1/2}$, $C^2\Pi_{3/2} \rightarrow A^2\Pi_{3/2}$, and $B^2\Sigma_{1/2} \rightarrow A^2\Pi_{1/2}$

are expected to occur in discharges containing these RgX excimers, with the largest

transition moments occurring primarily for isolated ionic interactions [33]. These

transitions are not apparent in Rg halogen systems in which the ion-pair states are

not isolated, as described above, but rather in those cases are embedded in a manifold

of Rydberg states [55, 83].

Fig. 4.13 shows a schematic diagram of the overall features of part of the system

of potential energy curves for the six low-lying RgX states, based on the work of

Casavecchia et al. [84] and Golde et al. [85]. These states will also arise for KrI, though

modified by being intermediate to heavy-atom Hund's case c spin-orbit coupling. For

the purpose of this discussion of the general features of the potential curves, it is

convenient to discuss KrI as though it belongs to case b. These $^2\Sigma$ and $^2\Pi$ states

are repulsive due to the interaction between the doubly occupied $4p$ orbital of the

krypton with the open shell $5p$ orbital of the iodine. Because the $^2\Pi$ state results

from interaction between two closed shells, whereas, the $^2\Sigma$ state results from an

interaction between a closed shell and an open shell, the $^2\Pi$ state is predicted to be

Internuclear distance (R)
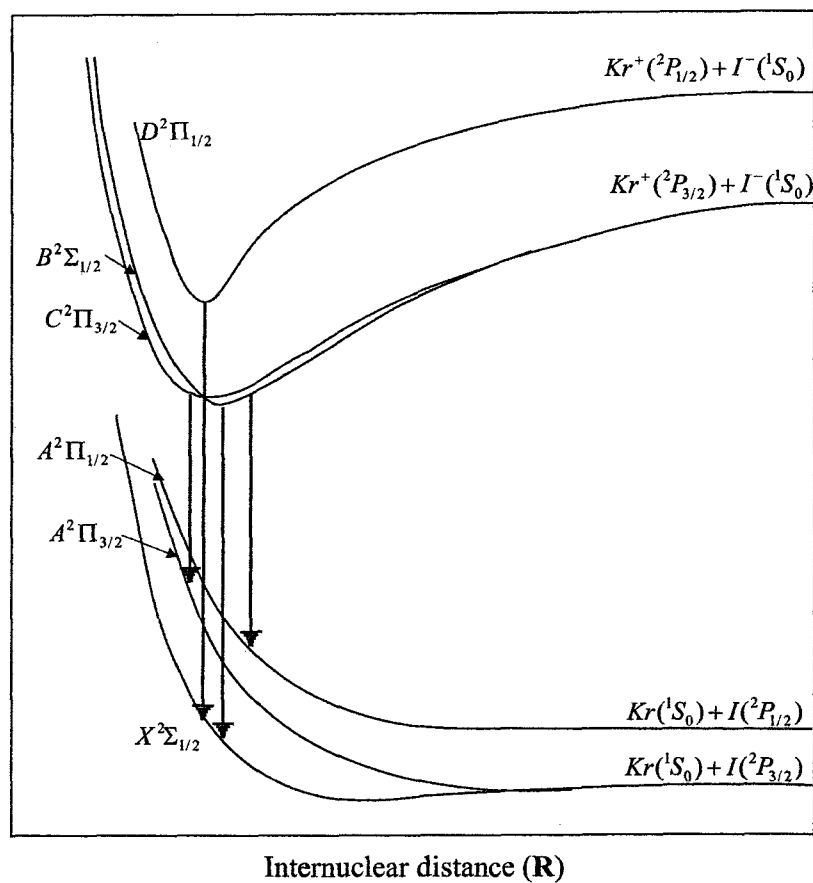
Figure 4.13: Potential energy curves for the low-lying electronic states of KrI. The transitions shown are observed for most RgX systems

more repulsive than the $^2\Sigma$ state [73, 79].

4.2.2 Background for KrI

Because RgX excimer transitions are used in commercial lasers, they are among the most comprehensively studied excimer systems [55]. Previous studies noted that the reaction mechanisms underlying the formation of the excited Rg halides are complicated, especially for the heavy halogens, which exhibit spin-orbit splitting.

Research group(s)	Mixture type	Technique	Reference
Casassa et al.	$Kr + I_2 / HI / CH_3 I / CH_2 I_2 + Ar$	DC discharge	[17]
Setser et al.	Kr/HI/Ar and He buffer gas	cold cathode discharge	[19]
Zhao et al.	Kr/HI/Ar and He buffer gas	photodetachment	[20]
Casavecchia et al.	$Kr + I_2$	molecular beam collision	[84]
Boyd et al.	$Kr/I_2/Ar$ buffer gas	DBD	[86]

Table 4.3: Previous KrI studies by selected research groups

In previous KrI* studies (see table 4.3), different reagents and methods were employed to generate KrI* emissions. But most of these studies were limited to low pressure (<100 torr) discharges where excimer states are not well populated. These observed excimer emissions are usually too weak to be useful for obtaining information of molecular potential curves. A recent, somewhat higher pressure study of KrI, performed by Boyd et al. [86], demonstrated strong excimer emissions at 191 nm (KrI* $B \rightarrow X$), 225 nm (KrI* $B \rightarrow A$) and 342 nm (I_2^* $D' \rightarrow A'$). Here for I_2^* excimer at pressures above 50 torr, the D state is collisionally converted to D', which decays via $D' \rightarrow A'$ emission around 342 nm and followed by thermalization of A' [87]. Unfortunately, the spectra Boyd et al. recorded were done only at low

resolution.

Thus, for high-pressure discharges in KrI*, experimental spectra are scarce, and there has not been a prior comprehensive theoretical study of the reaction dynamics. In this study, we present high-resolution spectra taken in rf discharges of KrI*/I_2^* over the 160 nm to 360 nm range and over the pressure range of 200 torr to 1500 torr with different gas mixtures. These spectral data are valuable to determine accurate potential energy curves for the KrI* excimer. The intensity relationships are useful for determining the reaction kinetics, as discussed below. In this investigation, we performed two separate experiments using i) additions of small amounts of pure crystalline iodine to research grade krypton gas (99.999% in purity), and ii) pre-mixed methyl-iodide (0.999%) in krypton (CH_3I/Kr) gas.

4.2.3   Emission Spectra for KrI* and I_2^*

In the case of the Kr and I_2 mixture, we added 5.0 mg of iodine crystals to 800 torr of krypton gas in our bulb, to yield an initial atomic number ratio I/Kr of about 3%. The CH_3I/Kr gas mixture was prepared with CH_3I forming 0.999% of total gas mixture. The CH_3I/Kr gas mixture was delivered through flame-cleaned stainless-steel 316LN lines to fill the discharge bulb to the desired pressure. In all our experiments, we ensured that the Kr/I mixture stayed at a fixed dilution ratio during operation.

Typical KrI*/I_2^* emission spectra from the capacitively coupled RF lamp, using the Kr/I_2 mixture and Kr/CH_3I mixture, are shown in Figs. 4.14 and 4.15 respectively.
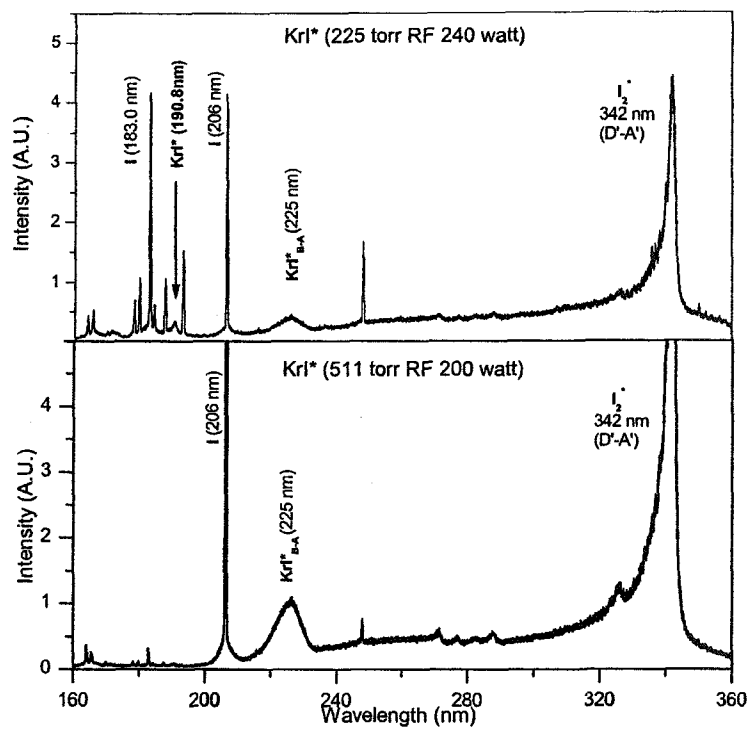
Figure 4.14: KrI*/I$_2^*$ spectra from Kr/I$_2$ mixtures in a capacitively coupled RF lamp at 225 torr and 511 torr
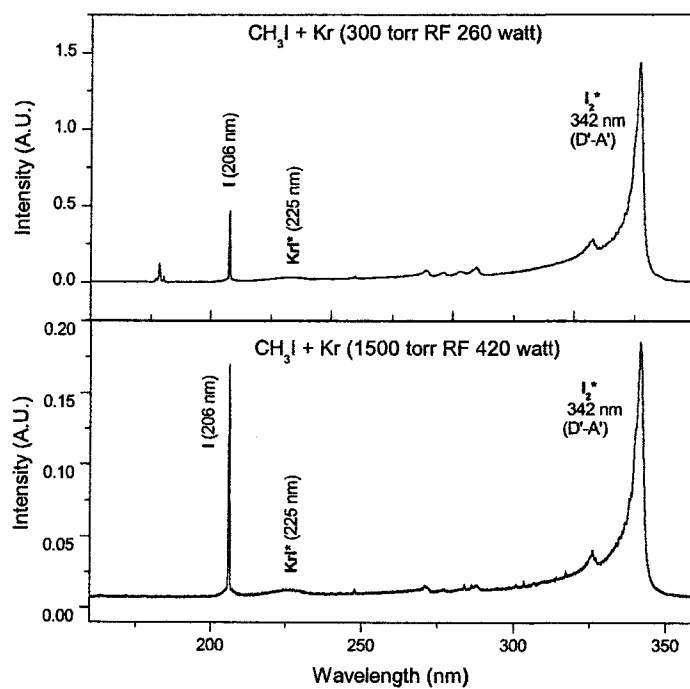
Figure 4.15: KrI*/I$_2^*$ spectra using CH$_3$I/Kr gas mixture. Over 90% of the emission is observed in the wavelength range of 300 nm - 350 nm

Although both Kr/I$_2$ and Kr/CH$_3$I mixtures yielded KrI* emissions, the production

of KrI* from the Kr/I$_2$ mixture was more efficient than the Kr/CH$_3$I mixture. The

wavelength locations of our observed spectral features are in good agreement with

previous studies of KrI* and I$_2^*$.
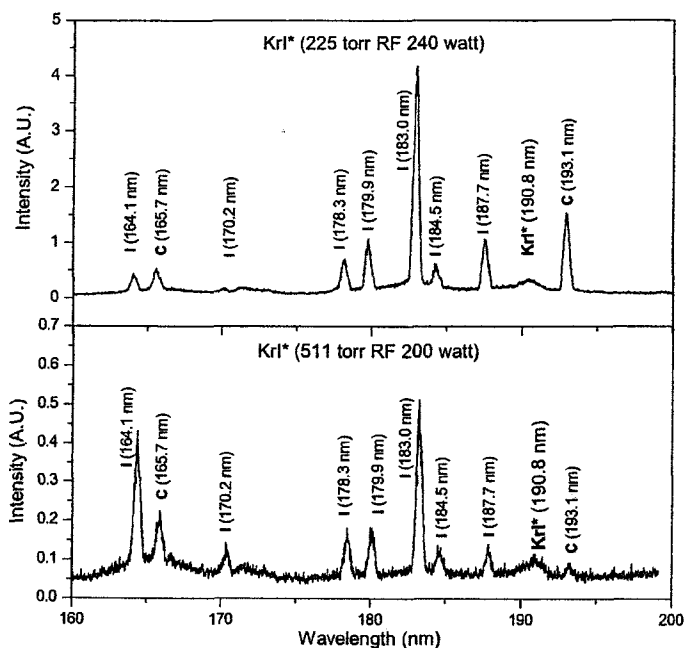
Figure 4.16: Details of the observed atomic lines below 200 nm in the KrI lamp filled with krypton and pure iodine

Fig. 4.16 shows the detailed emission below 200 nm for the case with krypton and

iodine. Tables 4.4 and 4.5 list the predominant molecular bands and atomic lines

that we observed. However, in the case with CH$_3$I, most of these atomic lines are

diminished even at pressure as low as 200 torr.

The observed emissions from excimer bands are given in table 4.4. Emissions from

Excimer transitions	Peak wavelength
B $^2\Sigma_{1/2} \rightarrow$ X $^2\Sigma_{1/2}$	191 nm KrI*
B $^2\Sigma_{1/2} \rightarrow$ A $^2\Pi_{1/2}$	225 nm KrI*
D$'$ $^3\Pi_{2g} \rightarrow$ A$'$ $^3\Pi_{2u}$	342 nm I$_2^*$

Table 4.4: Observed excimer transitions in the range from 160 nm to 360 nm

Transition levels	Wavelength (nm)	Relative Intensity
$^4P_{5/2} \rightarrow ^2P_{3/2}$	183	strong
$^2P_{3/2} \rightarrow ^2P_{1/2}$	206	strong
$^4P_{3/2} \rightarrow ^2P_{1/2}$	184.5	weak
$^2P_{1/2} \rightarrow ^2P_{1/2}$	179.9	weak
$^2P_{3/2} \rightarrow ^2P_{3/2}$	178.3	weak
$^2D_{3/2} \rightarrow ^2P_{1/2}$	170.2	weak
$^1S_0 \rightarrow ^1P_1$	247.9	strong
$^1D_2 \rightarrow ^1P_1$	193.1	strong
$^3P_2 \rightarrow ^3P_2$	165.7	weak

Table 4.5: Observed atomic lines in the range from 160 nm to 360 nm

iodine atomic transitions, shown in table 4.5, have been reported only at pressures less than 10 torr in previous work [17, 19]. Furthermore, those data were acquired either in separate studies, or were acquired in piecewise fashion in separate experimental runs. Thus relative intensities of the various emission bands could not be directly extracted in those previous studies. The present lamp spectrum is the first to display all of these emission in a continuously calibrated KrI*/I$_2^*$ spectra from 160 nm to 360 nm. We also note that because of the high power, high lamp efficiency, and the wide plasma operating range associated with 13.56 MHz RF capacitive coupling, accurate data were acquired over the pressure range from 200 torr to 800 torr at high resolution, distinguishing this work from the previous "high pressure" work on KrI*/I$_2^*$ reported

by Boyd et al. [86].

In the spectra obtained from both mixtures, we observed the $\mathbf{D}' \to \mathbf{A}'$ (342 nm I_2^*) transition at pressures below 200 torr, We did not observe the $\mathbf{B}\ ^2\Sigma_{1/2} \to \mathbf{A}\ ^2\Pi_{1/2}$ (225 nm KrI*) at low pressures. However, as pressure increased above 200 torr, both of these transitions were observed along with the other emissions. The $\mathbf{D}' \to \mathbf{A}'$ (342 nm I_2^*) transition is a broadband emission extending from below 300 nm to 350 nm that is shaded towards violet. Although we did not see a discernibly $\mathbf{C}\ ^2\Pi_{3/2} \to \mathbf{A}\ ^2\Pi_{3/2}$ (195 nm KrI*) continuum at high pressures around 1 atm, we believe that the 183 nm iodine resonance line, shown in Fig. 4.14, marks the low wavelength limit of that system.

Based on the potential energy curves shown in Fig. 4.13, the limiting low and high wavelength regions of the $\mathbf{B}\ ^2\Sigma_{1/2} \to \mathbf{A}\ ^2\Pi_{1/2}$ (225 nm) and $\mathbf{C}\ ^2\Pi_{3/2} \to \mathbf{A}\ ^2\Pi_{3/2}$ (195 nm) transitions are expected to be relatively close to the inner and outer turning points of the highest vibrational populated levels of the emitting states. In our spectra the low wavelength limit of the $\mathbf{B}\ ^2\Sigma_{1/2} \to \mathbf{A}\ ^2\Pi_{1/2}$ (225 nm KrI*) appears at 213.0 ± 0.5 nm, a displacement of about 7696.18 cm^{-1} (0.95 eV) from the 183 nm iodine line. This value is close to the 7603 cm^{-1} (0.94 eV) spin-orbit splitting of the iodine atom [16]. Similarly, the long wavelength limit of the $\mathbf{C}\ ^2\Pi_{3/2} \to \mathbf{A}\ ^2\Pi_{3/2}$ (195 nm KrI*) is separated from the long wavelength limit of the $\mathbf{B}\ ^2\Sigma_{1/2} \to \mathbf{A}\ ^2\Pi_{1/2}$ (225 nm KrI*) by a value also close to the iodine spin-orbit splitting.

Some of the observed transitions changed in intensity and shape as a function of pressure, indicating different collisional processes associated with their formation.

The $\mathbf{B}\ ^2\Sigma_{1/2} \rightarrow \mathbf{X}\ ^2\Sigma_{1/2}$ (191 nm KrI*) emission remained very weak but the intensity

drops slowly with pressure. Increasing the pressure diminishes the 342 nm structure

as a result of vibrational relaxation. The $\mathbf{B}\ ^2\Sigma_{1/2} \rightarrow \mathbf{A}\ ^2\Pi_{1/2}$ (225 nm KrI*) emission

intensity is more than doubled over the pressure range 225 torr to 511 torr (Fig. 4.17)

and the width of this feature also changed.
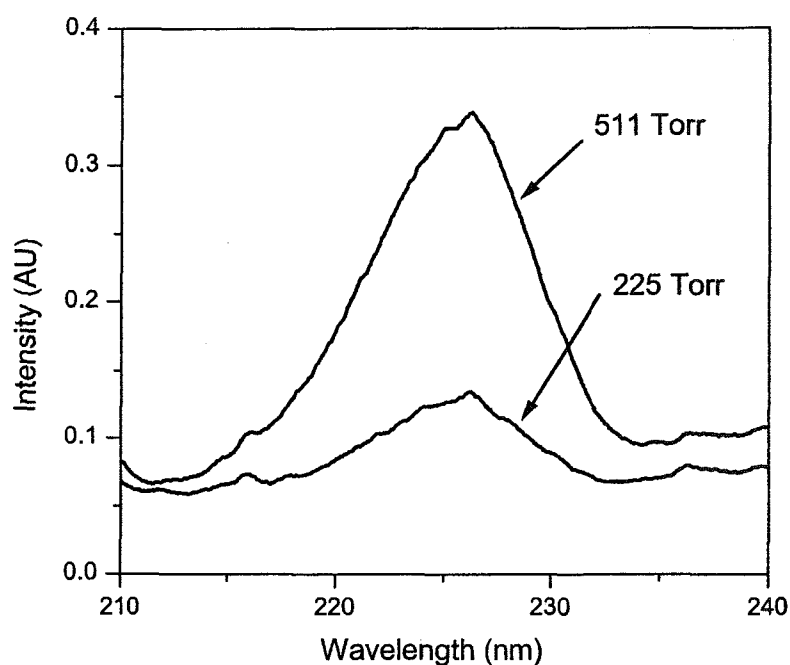
Figure 4.17: Pressure dependence of the KrI* $\mathbf{B}\ ^2\Sigma_{1/2} \rightarrow \mathbf{A}\ ^2\Pi_{1/2}$ transition. The emission
is more than doubled as pressure invereases from 225 torr to 511 torr

We can see from Fig. 4.14 that the 225 nm KrI* band superposes on the 342

nm I_2^* band. The contribution from I_2^* emission is subtracted from the observed

KrI* intensity in the band width calculation and the line shape simulation in a later

chapter. The full width at half maximum (FWHM) values of the $\mathbf{B}\ ^2\Sigma_{1/2} \rightarrow \mathbf{A}$

$^2\Pi_{1/2}$ (225 nm KrI*) transition at 225 torr and 511 torr are $\sim$7.5 nm and 10 nm respectively. The enhancement of this transition with increasing pressure, we believe, is due to electronically quenching of the C $^2\Pi_{3/2}$ state in favor of the B $^2\Sigma_{1/2}$ state as suggested by Y. T. Lee et al. [17], who observed an analogous enhancement of the B $^2\Sigma_{1/2} \to$ A $^2\Pi_{1/2}$ transition as a function of pressure in other RgX excimer studies. These data are not sufficient to infer how the vibrational distribution in the B $^2\Sigma_{1/2}$ state changes with pressure.
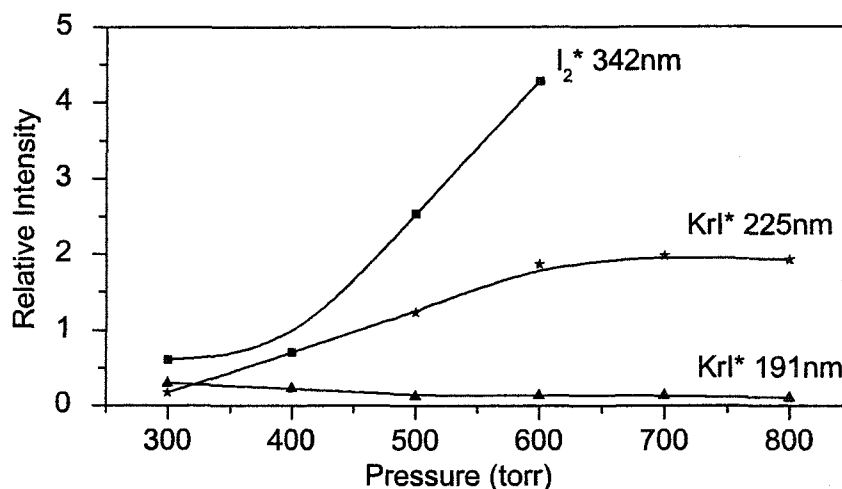
Figure 4.18: Pressure dependence of the 191 nm KrI* (B $^2\Sigma_{1/2} \to$ X $^2\Sigma_{1/2}$), 225 nm KrI* (B $^2\Sigma_{1/2} \to$ A $^2\Pi_{1/2}$) and 342 nm I_2^* (D$'$ $\to$ A$'$) transitions

Fig. 4.18 shows the pressure dependence of the 191 nm KrI*, 225 nm KrI*, and 342 nm I_2^* emission intensities from 300 to 800 torr. Our results are in contrast to the observation of Boyd et al. [86], who saw a decrease of the 342 nm I_2^* with an increasing pressure. The distribution over electronic states, and the distribution of vibronic levels

within an electronic state strongly depend on the excitation technique employed. It is therefore not surprising that our observed KrI^* and I_2^* pressure dependence is different from what was observed by Boyd et al. in a DBD system. A rise in I_2^* emission with pressure has been observed in other studies [55] where cw excitation was used.

4.2.4 Kr/I$_2$ Mixture Reaction Kinetics

The reaction kinetics of the rare gas halides are rather complex because a large number of atomic and molecular species are involved in many different reactions. Besides, the quenching rate constants and effective radiative lifetimes usually depend on the partial gas pressures and the internal energy of generated molecules [88]. In this section we derive a preliminary kinetic model for high-pressure KrI based on the simple steady-state rate equation model for Xe used by Schoenbach et al. [67].

KrI^* and I_2^* intensities are governed by the population of the upper emitting states. The population of the emitting states is dependent on the (1) molecular excitation and de-excitation processes, (2) the density of the electronically excited species and (3) excitation and relaxation rate coefficients on gas density. The following set of rate equations suffices to describe the relevant dominant processes involved in production of KrI^* and I_2^* excimers.

$$
\begin{array}{lll}
\text{(a)} & e^- + Kr \longrightarrow Kr^+ + 2e^- & \\[2mm]
\text{(b)} & e^- + Kr \longrightarrow Kr^* + e^- & (4.18)
\end{array}
$$
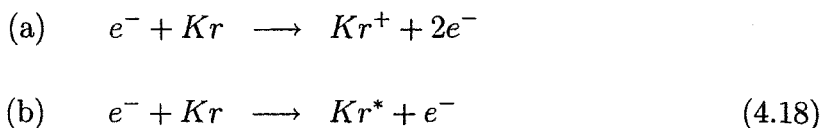
These initial reactions in Eq. 4.18 are presumably intended to be electron impact excitation processes. The ionization potential energy for krypton is 14 eV [51], and the average energy needed to excite a krypton atom to its first excited state is about 9.9 eV [58]. We will demonstrate the existence of hot electrons by PIC simulations in the next chapter. From the electron energy distribution function in Fig. 5.15, these hot electrons are certainly capable of causing these excitation processes, which are usually described by an energy-dependent-cross-section, σ.

At high pressure, collisions rapidly promote electronic and vibrational relaxations to the lowest lying levels of the ionic curves. The reaction to form the Kr_2^* excimer state is mainly by three-body collisions, Eq. (4.19), which have been found to be a strong destruction process for the lower metastable ($1s_5$) level in krypton by Turner [89].

$$Kr^* + 2Kr \xrightarrow{\kappa_1} Kr_2^* + Kr \qquad (4.19)$$
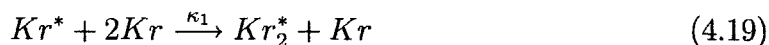
where the three-body collisional destruction rate, κ_1, was found by Ku et al. [90] to be 5.36×10^{-32} cm^6/s.

When iodine is added to krypton, KrI* is predominantly produced by the harpooning and ion-ion recombination processes. KrI is known to be predissociated strongly [91]. For simplicity, we assume the ion channel does not predominate in the production of KrI*. The dependence of the I_2^* fluorescence yield in Fig. 4.18 was found to be largest at high pressure, so we assume Kr_2^* is the primary source of I_2^*

in high pressure discharges. The direct excitation transfer process, which acts as the primary excitation pathway in our system can be written as:

$$Kr_2^* + I_2 \xrightarrow{\kappa_2} 2Kr + I^* + I \tag{4.20}$$
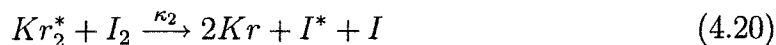
The rate constant, κ_2, for Eq. (4.20) is not available based on our search, so a value for this reaction between Kr_2^* and F_2 will be used here ($\kappa_2 = 2.1 \times 10^{-10}$ cm^6/s) [92].

$$I^* + I_2 \xrightarrow{\kappa_3} I_2^* + I \tag{4.21}$$

$$Kr^* + I_2 \xrightarrow{\kappa_4} KrI^* + I \tag{4.22}$$

In the harpooning reactions Eqs. (4.21) and (4.22), the excited species, Kr^* and I^*, will transfer their loosely bound electron to the iodine molecule [86] to create an attractive bond between them. The rate constant κ_3 for Eq. (4.21) is about 1.5×10^{-9} cm^3/s [55]. Although the rate for harpooning reaction to generate KrI^* is not available, there is evidence showing that the quenching rates for rare gases with the same halogen reagent do not vary much [80], so we use the known rate between Ar^* and I_2 [55] for Eq. (4.22), which is $\kappa_4 = 1.8 \times 10^{-9}$ cm^3/s. As pressure is raised, the rates of formation in these harpooning reactions are expected to increase leading to the formation of KrI^* and I_2^*.

$$(a) \quad Kr^* \xrightarrow{\tau_1} Kr + h\nu$$

$$(b) \quad Kr_2^* \xrightarrow{\tau_2} 2Kr + h\nu$$

$$(c) \quad I^* \xrightarrow{\tau_3} I + h\nu$$

$$(d) \quad I_2^* \xrightarrow{\tau_4} 2I + h\nu$$

$$(e) \quad KrI^* \xrightarrow{\tau_5} Kr + I + h\nu$$

$$(4.23)$$
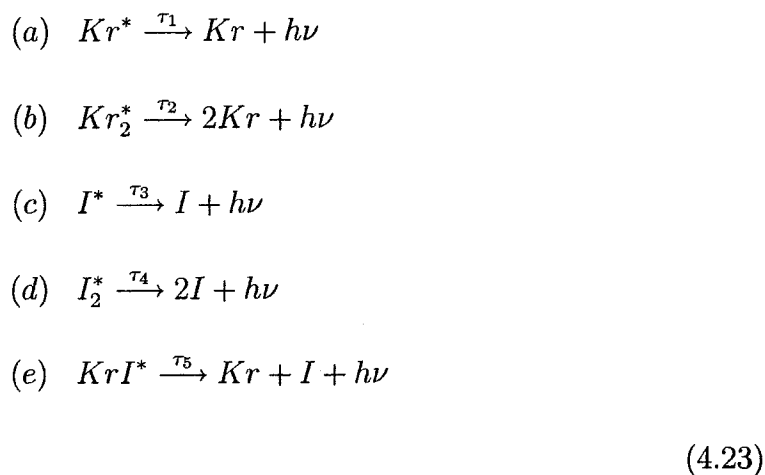
These excited species all decay to their lower states through radiative steps shown in Eqs. 4.23(a-e), and τ_1 through τ_5 are the radiative decay constants. There have been many reports about the decay of resonance radiative in pure krypton, such as Turner's result, $\tau_1 = 4.15 \times 10^{-9}$s [89]. The radiative decay constant for Kr_2 is $\tau_2 = 2.83 \times 10^{-6}$s [93], and the rates of I^* and I_2^* were reported as $\tau_3 = 57.9 \times 10^{-9}$s [94] and $\tau_4 = 7 \times 10^{-9}$s [55, 95] respectively. Although the radiative decay rate of KrI^* has not been directly measured, theoretical data indicates that it is of the order of $\sim 10^{-9}$s.

Based on the above reaction kinetics for Kr/I mixture, we developed simple steady-state rate equations to predict the pressure dependence of the KrI^* and I_2^* emissions. The rate equations describing the generation of KrI^* and I_2^* are given in Eqs. 4.24(a-e) below. In this model, we assume steady state concentrations for KrI^*, I_2^*, I^*, Kr_2^*, and Kr^*, to obtain the estimates of the excited state densities.

$$(a) \qquad \frac{d}{dt}[KrI^*] = \kappa_4[Kr^*][I_2] - \frac{1}{\tau_5}[KrI^*] = 0$$

$$(b) \qquad \frac{d}{dt}[I_2^*] = \kappa_3[I^*][I_2] - \frac{1}{\tau_4}[I_2^*] = 0$$

$$(c) \qquad \frac{d}{dt}[I^*] = \kappa_2[Kr_2^*][I_2] - \frac{1}{\tau_3}[I^*] = 0$$

$$(d) \qquad \frac{d}{dt}[Kr_2^*] = \kappa_1[Kr^*][Kr]^2 - \frac{1}{\tau_2}[Kr_2^*] = 0$$

$$(e) \qquad \frac{d}{dt}[Kr^*] = \frac{P'}{w} - \kappa_4[Kr^*][I_2] - \kappa_1[Kr^*][Kr]^2 - \frac{1}{\tau_1}[Kr^*] = 0$$

$$(4.24)$$

where P' is the deposited power in a unit volume of the discharge and w is the mean

energy necessary to produce one excited krypton atom [67]. Combining Eqs. 4.24(a)

to 4.24(e), we obtain expressions for the [KrI*] and [I$_2^*$] excimer concentrations re-

spectively as:

$$(a) \qquad [KrI^*] = \frac{P'}{w} \cdot \frac{\tau_5 \kappa_4 [I_2]}{\kappa_4[I_2] + \kappa_1[Kr]^2 + 1/\tau_1}$$

$$(b) \qquad [I_2^*] = \frac{P'}{w} \cdot \frac{\tau_2 \tau_3 \tau_4 \kappa_1 \kappa_2 \kappa_3 [Kr]^2 [I_2]^2}{\kappa_4[I_2] + \kappa_1[Kr]^2 + 1/\tau_1}$$

$$(4.25)$$

Assuming an ideal gas, we can express [Kr] and [I$_2$] in Eqs. 4.25(a) and 4.25(b)

in terms of the total gas pressure, P,

Letting [Kr]=aP/kT, where a is some constant obtained from the mixture ratio

and kT is the neutral gas thermal energy, we have $[I_2]=(1-a)P/kT$. Hence the solutions in Eq. (4.25) can be expressed as a function of the total gas pressure.

$$
\begin{aligned}
\text{(a)} \quad [KrI^*] &= \frac{P'}{w} \cdot \frac{\tau_5\kappa_4(1-a)P}{\kappa_4(1-a)P + \kappa_1 a^2 P^2/kT + kT/\tau_1} \\
\text{(b)} \quad [I_2^*] &= \frac{P'}{w} \cdot \frac{\tau_2\tau_3\tau_4\kappa_1\kappa_2\kappa_3 a^2(1-a)^2 P^4/(kT)^4}{\kappa_4(1-a)P/kT + \kappa_1 a^2 P^2/(kT)^2 + 1/\tau_1}
\end{aligned}
$$

$$(4.26)$$

The model above provides us with a sufficient idea of how the KrI* and I$_2^*$ emissions respond to pressures changes. In RF discharges, there are two components of excitation, a steady-state one and a time-dependent component. Typically, the latter is not able to follow field changes at 13.56 MHz, thus the steady state component dominates.

In order to compare this model with experiment, accurate estimates for the reaction rates are necessary. From Eq. (4.26), parameters that govern the curve shapes include κ_1, κ_4 and τ_1. Although κ_1 for the three-body collisional destruction rate is considered accurate enough, κ_4 hasn't been completed studied. Besides, detailed studies [96, 97, 98, 99, 100] of τ_1 indicate that it strongly depends on pressure. By varying κ_4 and τ_1 and fitting our model to KrI* results obtained from our experiments, we obtain $\kappa_4 = 2.9 \times 10^{-12}$ cm^3/s and $\tau_1 = 1.2 \times 10^{-6}$s. Because the decay rate depends on gas pressure, these values obtained from data fitting should only be considered as average values within the pressure range of our interest. The curves

obtained from our model calculation are plotted in Fig. (4.19) along with the data

points.
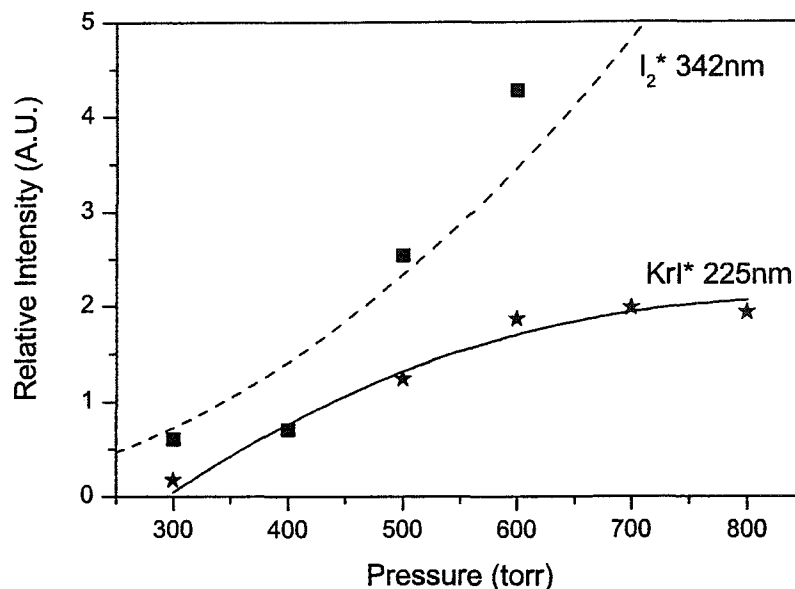
Figure 4.19: Measured and calculated excimer intensities for KrI* and I_2^*. Solid line is the calculated values for KrI* from fitting, and the I_2^* model is plotted as a dash line using the KrI* fitting results

A useful comparison is made in table 4.6 to Boyd's KrI work. The major difference

is probably caused by the channel of direct energy transfer process. Our lamp has

been proven to be efficient for formation of Xe_2^* molecules at high pressure, so at high

Kr-host gas pressures, the formation of Kr_2^* molecules is considered to be dominant,

which also leads to the increasing I_2^* fluorescence yield in our kinetic model. Boyd

has Kr* as the major agent for energy transfer, so a decreasing pressure dependence

for I_2^* was observed. The very weak KrI* $\mathbf{B}\ ^2\Sigma_{1/2} \rightarrow \mathbf{X}\ ^2\Sigma_{1/2}$ transition at 191 nm

	Current work of KrI	Boyd's work of KrI
KrI $B \rightarrow X$ 191nm	very weak, slowly decreases vs P	strong, remains constant
KrI $B \rightarrow A$ 225nm	strong, increases vs P	strong, increases vs P
I^* 183nm	strong at low P, but very weak at high P, decreases vs P	very strong, increases vs P
I_2^* 342nm	very strong, increases vs P	strong, decreases vs P
Kinetics for I^*	$Kr_2^* + I_2 \rightarrow 2Kr + I^* + I$	$Kr^* + I_2 \rightarrow Kr + I^* + I$

Table 4.6: Comparison of KrI results between our work and Boyd's

in our lamp is due to the predissociation [55, 86]. Besides iodine vapor absorption in the long light path of our system is also significant because iodine has a strong absorption band below 200 nm [101, 102], which will be further discussed in the next section. Boyd's system has an optically thinner light path than ours, so the observed $B \rightarrow X$ transition doesn't suffer from iodine absorption as we do here.

4.3 Emission Spectra of XeI Excimers

The bound-free emission spectra for XeI have been extensively investigated by many groups [17, 79], and detailed theoretical interpretation of these spectra has been successfully achieved by Tamagake [14], and independently by Tellinghuisen [103, 104]. The potential diagram for XeI is similar to that of KrI shown in Fig. 4.13.

Our recorded XeI spectra (see Fig. 4.20) are consistent with these previous reports. The two intense excimer emissions are assigned to $B_{1/2} \rightarrow X_{1/2}$ at 253 nm and $B_{1/2} \rightarrow A_{1/2}$ at 320 nm [82]. We observed a decrease in XeI(B) emission at high
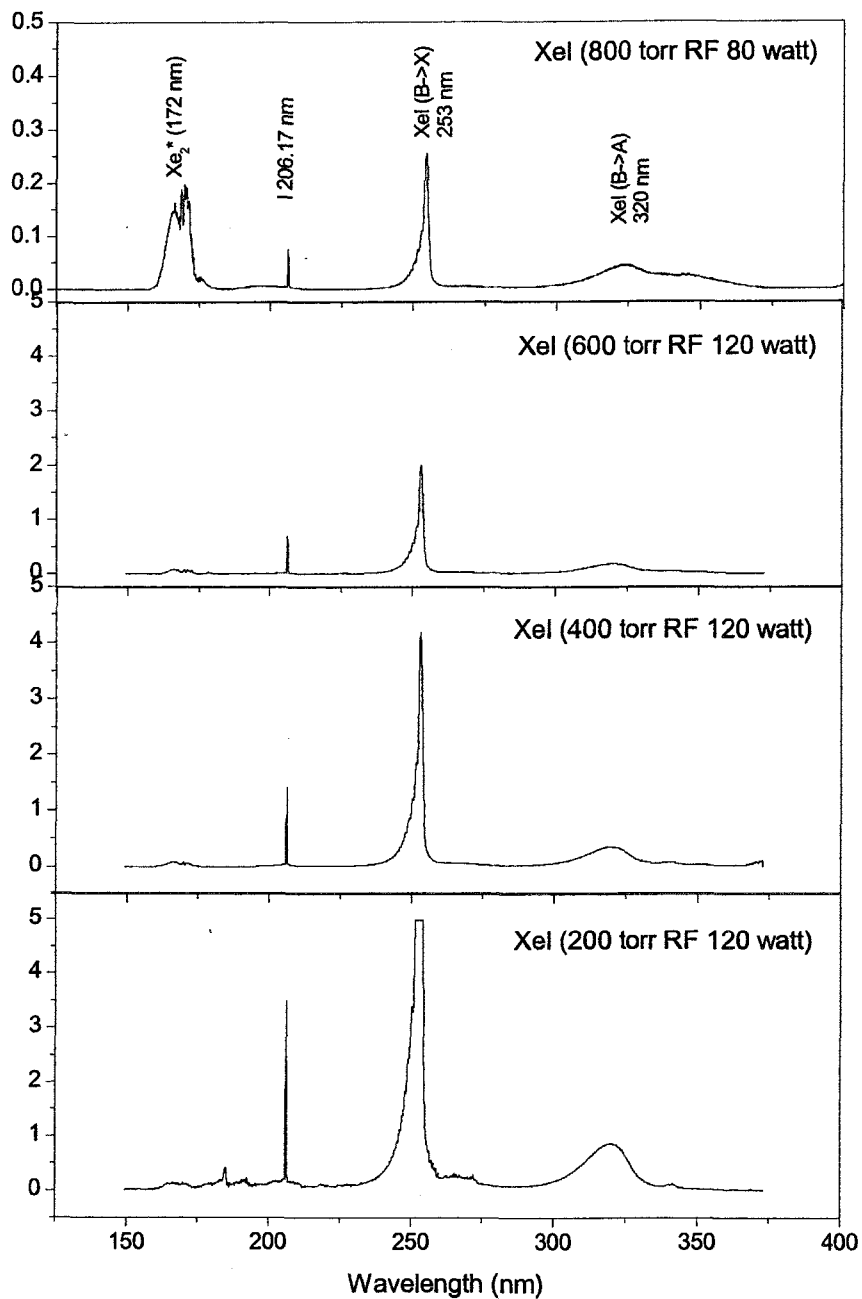
Figure 4.20: XeI broad band emissions at different pressures

pressures, this may in part be due to formation of Xe_2I^* [105]. The major differences

between XeI and KrI are: (1) XeI spectra have a very strong $B_{1/2} \rightarrow X_{1/2}$ emission

at 253 nm, whereas this system is weak or absent for KrI; (2) the $D' \rightarrow A'$ emission

of I_2^* at 342 nm is quenched in the case of XeI; (3) no I resonance lines are observed

in XeI discharges below 200 nm, such lines are strong in KrI.
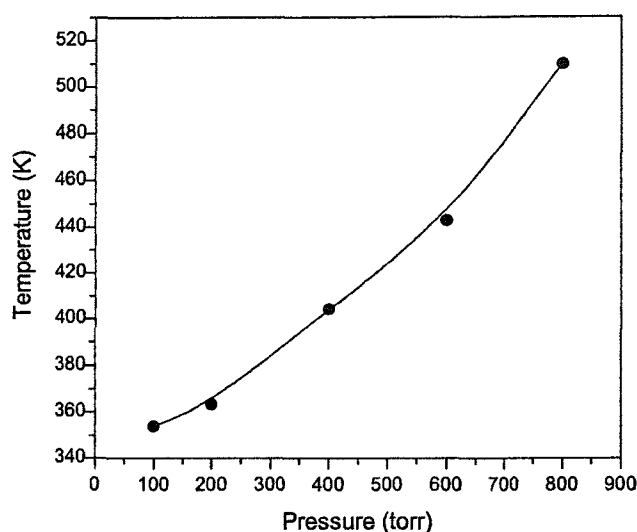
Figure 4.21: Outer surface temperature of 120 watt XeI RF lamp at different pressures

Fig. 4.21 shows the temperatures measured on the outside of the bulb close to

the tuner where the hottest electrons are present. The bulb temperature increases

rapidly with gas pressure. By using the calculated temperature relationship shown in

Fig. 4.10, the discharge temperature for a 120 watt XeI lamp at 400 torr is estimated to

be about 1016 K. Compared with the 140 watt Xe lamp at 400 torr with a temperature

of 945 K, the XeI lamp will emit more heat, resulting in a lower efficiency for producing

the desired VUV and near UV emission.
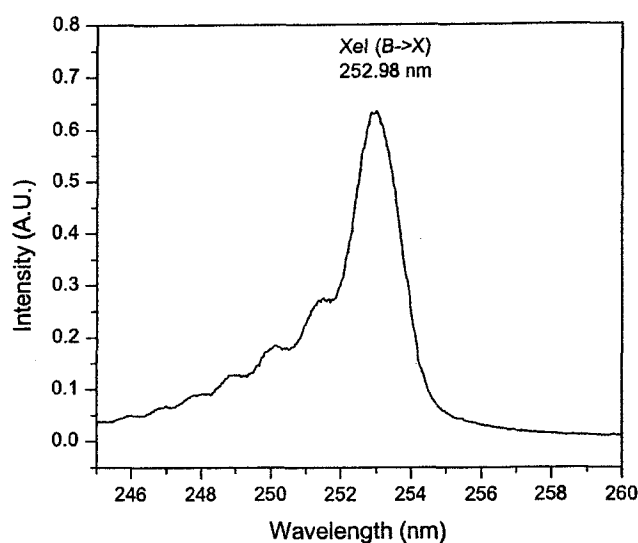
Figure 4.22: The undulatory structure of $B \to X$ transition in a 80 watt XeI lamp at 800 torr

The intense emission band observed in Fig. 4.22 has potential antibacterial applications since certain DNA chains in microbes have strong absorption band around 250 nm.

The undulatory structure on the short wavelength side of the band can be explained as the result of bound-free transitions from a bound upper state to a slowly varying repulsive lower state [103]. This structure results from emissions from low $(v' = 1, 2, ...)$ vibrational levels of the upper state. About 95% of excited molecules will be in vibrational states $v' = 1, ..., 4$ [79]. However, the peaks do not indicate the exact position of the maximum for each component. The analytical decomposition by Tellinghuisen et al. [103] shows that each peak in the spectrum also contains

contributions from other higher v' levels.
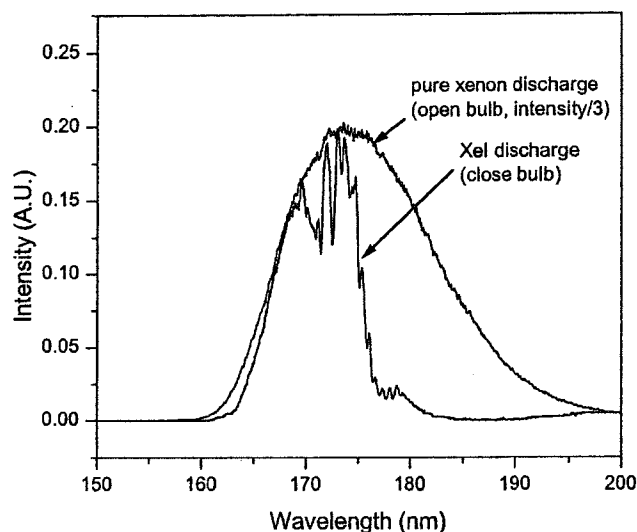
Figure 4.23: The second continuum of Xe_2^* in pure xenon and XeI discharges

In the XeI discharge, the second continuum of Xe_2^*, at around 172 nm, is found to increase in intensity as pressure increases in a XeI lamp, but the long wavelength part of the emission band (Fig. 4.23) appears to be "chewed out". We believe this is caused by the absorption of I_2 vapor. According to Hiraya and Donovan [101, 102], who studied the VUV emission and absorption spectra of I_2 in detail, there are a broad ion-pair absorption bands between 178 nm and 200 nm and strong Rydberg transitions, which dominate the region between 132 and 178 nm. The absorption cross-section curve (Fig. 4.24) they obtained, corresponds to the cut off of Xe_2^* band at around 175 nm, and the dips we see at around 170 nm.

Fig. 4.24 also shows that a likely reason for the observed weakness of the $B_{1/2} \rightarrow$
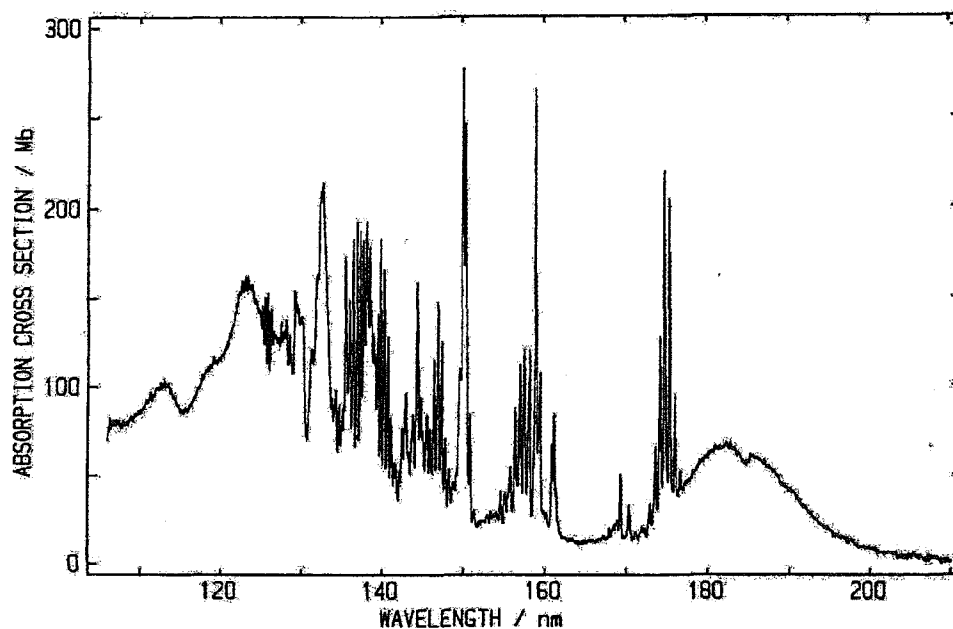
Figure 4.24: The absorption cross section for I_2 (after Hiraya et al.)

$X_{1/2}$ emission at 191 nm and for the absence of the $C_{3/2} \rightarrow A_{3/2}$ emission at 195 nm in KrI is that they are strongly absorbed by iodine. The $B_{1/2} \rightarrow X_{1/2}$ emisssion for XeI* survives at 253 nm because of the lack of iodine absorption in this region. This "self-filtering" of the KrI lamp makes it even more useful for biological application in the 250 nm range [106]. It would be possible to achieve the same degree of narrow-band filtering by using an absorbing bulb jacket material, or by adding optical high-pass filters to cut off the far uv region to the same degree as observed in our lamp. However, filtering by I_2 in the gas phase is greatly preferred since the absorption process promotes the desired sequence of reactions to form excimers, via Eq. (4.21) above, rather that dissipating the electrical power unnecessarily as unwanted heat in

the bulb jacket.

Chapter 5

MAGIC Simulation

5.1 Introduction of PIC Simulation

Particle-In-Cell (PIC) simulation is a widely used numerical technique for solving

hyperbolic equations in arbitrary dimensions. MAGIC is a PIC tool particularly useful

for electromagnetic (EM) simulations. It utilizes a set of computational particles to

represent the transport of locally conserved quantities like mass and charge in an EM

field, governed by Maxwell equations on a pre-defined spatial grid. These particles are

described by macroparticles in a 6D phasespace (x, y, z, P_x, P_y, P_z), whose movements

are confined by certain boundary conditions.

A typical PIC simulation includes solving real-life problems with several coupled

particle equations and EM field equations dynamically. Numerical methods are very

useful to deal with these problems especially when complex materials and geome-

tries are involved. Standard numerical techniques, such as second-order in space

and time, like conventional finite difference (FD) method [107], finite-difference time-

domain (FDTD) method [108, 109, 110], and finite integration technique (FIT) [111]

111

are usually applied on spacial grids to obtain solution of Maxwell equations. Although these methods have been very popular, mainly due to their simplicity and the ability to handle large to huge problems, they still suffer difficulties when modeling geometries with curved material boundaries on orthogonal grids, resulting in inaccurate solutions close to such boundaries. In addition, these numerical methods in the time domain suffer from artificial numerical dispersion. Readers are directed to the paper of Gjonaj et al. [112] for details of handling some of these problems.

5.2 Impact Ionization Test by Electron Beam (EB) Injection

Ionization of rare gas atoms is very important in the nonequilibrium process of excimer formation. In a discharge, the generation of charged particles are mostly due to ionization of a background neutral gas. Electron-impact ionization and photoionization are fundamental processes in atomic and molecular physics [113], and electron-impact ionization is one of the most important processes in our excimer lamps.

In this section, we simulate a dynamic process when a short E-beam is injected into a fused silicon bulb filled with xenon to a certain pressure. In fact, this is one of the simplest methods to generate excimers and is used in many excimer laser systems. In our experiments, as mentioned before, we use a Tesla coil to ignite our lamps. The Tesla coil can usually generate a voltage of ~10 kV at its tip, high enough to break

down the rare gas inside the bulb when the tip gets close enough. The hot electrons initialized by this process will generate ions and secondary electrons by collisions with the background neutral gas. In this section, we concentrate on the initial particle interactions in our lamps.

The Tesla coil is a low-Q tuned circuit that generates a.c. voltages at frequencies around 500 KHz. So the exciting voltage has a period $\sim 2 \times 10^{-6}$ s. To model this, we inject a uniform E-beam with the energy of 500 eV, and turn it off after 8×10^{-13} s, following the subsequent dynamic processes. The short period allows for a uniform energy assumption, brings least interference to the post simulation when an external EM field (RF or microwave) is added, and keeps the total number of particles low for yielding a shorter simulation time.
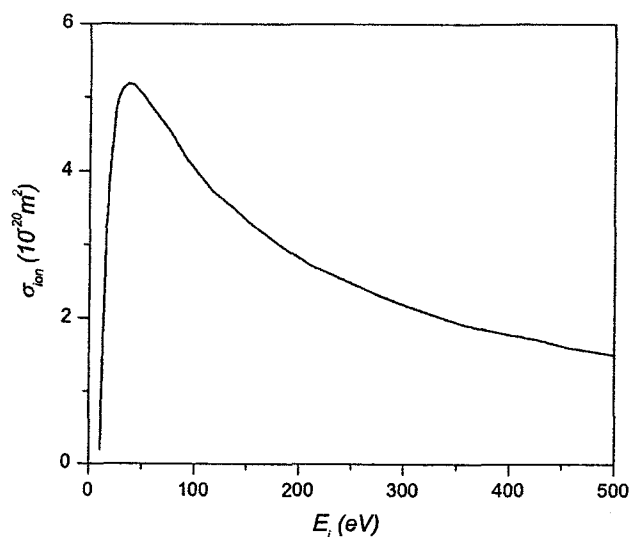
Figure 5.1: The cross section for ionization of the ground state ($5p^6 \, ^1S_0$) xenon atom by an electron of energy E_i (after D.A. Erwin and J.A. Kunc)

MAGIC uses externally configurable modules to create a block-functional model of a plasma. Charged particle creation can be done in various ways, one of which is a module called "IMPACT", which determines the ionization rate based on the electron impact ionization cross-section coefficients associated with the particular target neutral. In our simulation for xenon gas discharge, we used cross-section results from a recent work done by Erwin et al. [114] (Fig. 5.1). The cross-section function $\sigma_{ion}(E_i)$ used in MAGIC is in units of the standard atomic unit ($\pi a_0^2 = 0.88 \times 10^{-20} \text{m}^2$), and E_i is in units of eV.

The rate equation for the impact-ionization model is given by the following equation:

$$\frac{dn^-}{dt} = \frac{dn^+}{dt} = \sigma_{ion} n_t \phi_I, \tag{5.1}$$

where, σ_{ion} is the total cross section for impact ionization, n_t is the target neutrals number density, and ϕ_I is the incident particle flux.

Figs. 5.2 through 5.6 show results for an impact ionization simulation in a 10 torr xenon bulb. In this simulation, electrons enter as a uniform circular beam from the left side of the picture, causing ionization. The resulting charge particle motions are shown in the figure.

Fig. 5.2 shows the location of charged particles after a significant time of interval; the blue lines indicate positively charged xenon ions created by collisions between the injected energetic electrons and neutral xenon atoms. The charged particles created during electron impact are given a momentum based on a Maxwellian distribution,
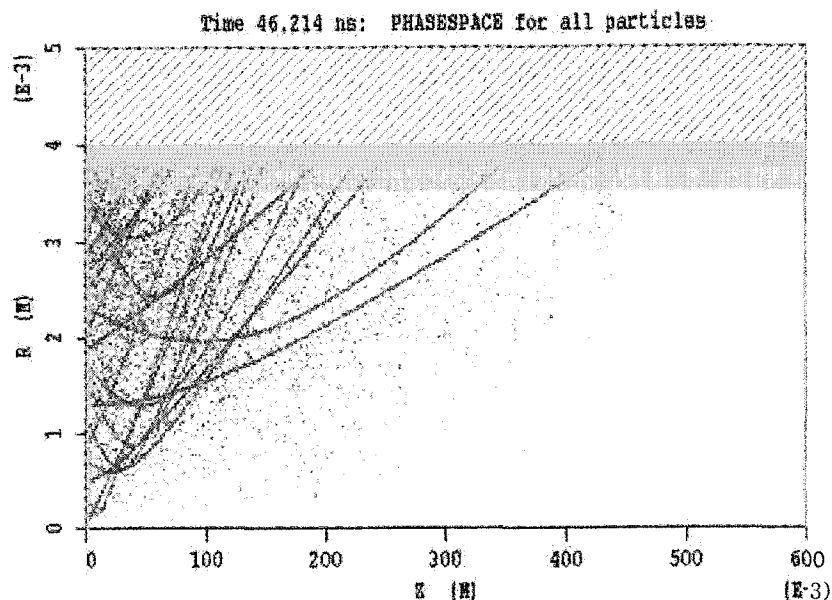
Figure 5.2: Phasespace plot of ions (blue) and electrons (red) in an impact ionization model

which assumes a thermal energy equal to kT, where T is the gas temperature.

Among the charged particles created by impact ionization, electrons gain much more momentum and have a higher kinetic energy than ions, as shown in Fig. 5.3 through 5.5. If an EM field exists, these electrons are accelerated, and create subsequent collision products. Since ions move much slower than electrons, when an EM field is added, they look "quasi-static". Electrons serve to transfer energy to these heavy neutral atoms or ions.

Since our bulb is about 60 cm long and only 0.8 cm in ID, the plasma generated by an E-beam injection from one end of the bulb without other external drive is very nonuniform. Although the average electron density is a very important parameter in a discharge, and is one of the key means of classifying discharges, the high degree of

Time 60.516 ns: PHASESPACE for all particles
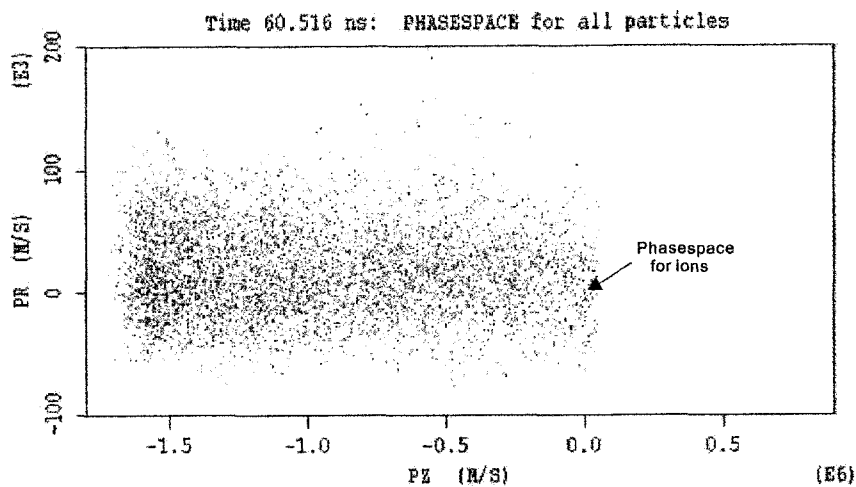
Figure 5.3: The momenta of all particles in an impact ionization model. Electrons (red) have a much higher momentum than ions (blue)

Time 60.516 ns: PHASESPACE for all particles
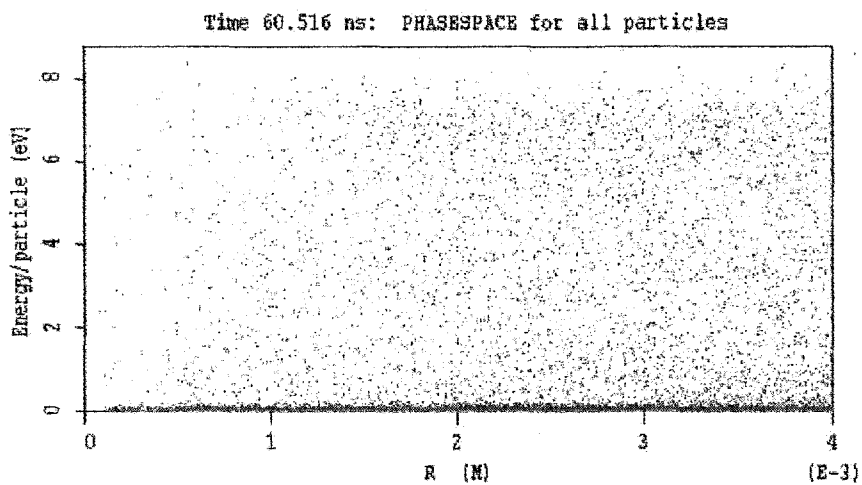
Figure 5.4: Particle energy distribution in the radial direction. Electrons (red) have a much higher kinetic energy than ions (blue)

Time 46.200 ns: PHASESPACE for all particles
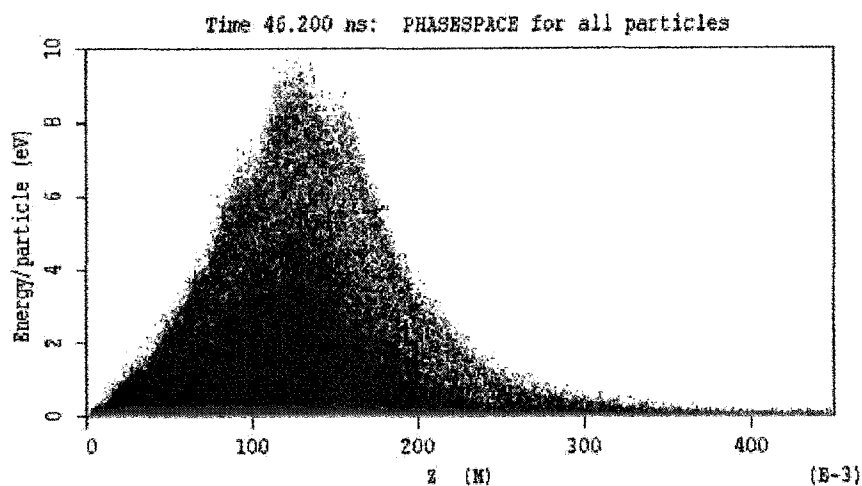
Figure 5.5: Particle energy distribution in the longitudinal direction. Electrons (red) have a much higher kinetic energy than ions (blue). The longitudinal distribution of electron energy also is quite non-uniform

Time 60.516 ns: ELECTRON number density at OSYS$AREA
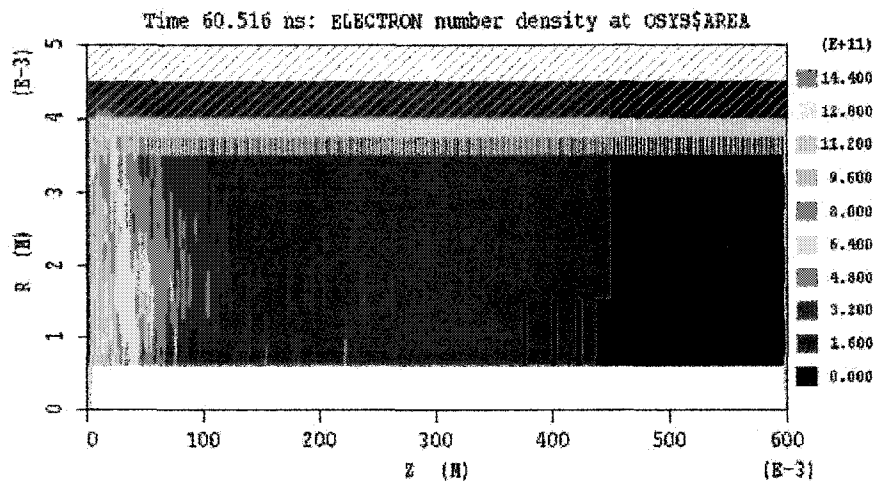
Figure 5.6: Longitudinal electron density distribution in a 10 torr xenon bulb at 60.516 ns

Time 60.516 ns: XENON number density at OSYS$AREA
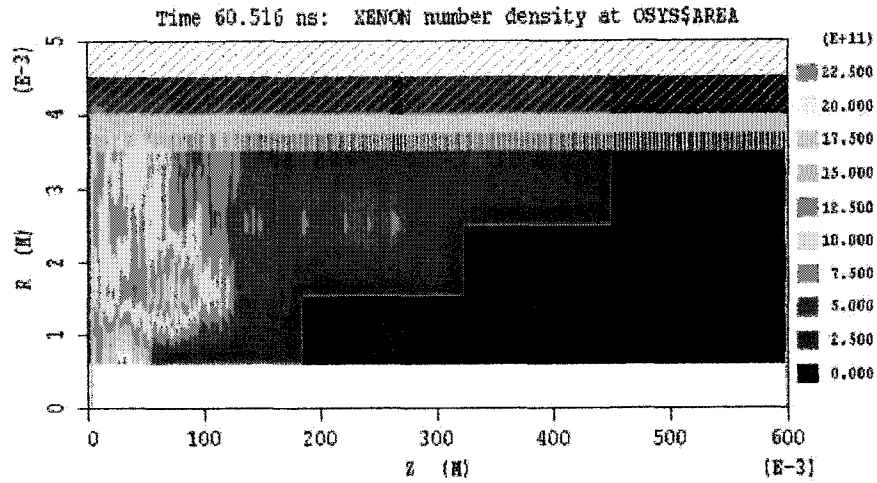
Figure 5.7: Longitudinal xenon ion density distribution in a 10 torr xenon bulb at 60.516 ns

spatial non-uniformity reduces the utility of this simple means of expression. We must use more moments of the distribution, or the distribution itself to discuss the resulting excimer physics. The maximum plasma density, and the detailed density distribution within the bulb, determine the local Debye length. This parameter determines the scale length of the grid for computation.

Fig. 5.6 and 5.7 show the number density distribution of electrons and xenon ions. For 10 torr xenon bulb, the maximum plasma density is about $10^{12}/m^3$. We also note that the distribution is very non-uniform and shows a hollow density profile with peaks near the wall of the tube.

One fundamental characteristic frequency of a plasma is the electron plasma frequency which represents a sinusoidal oscillation of the electron cloud with respect to

the ion cloud, given by

$$\omega_{pe} = \left(\frac{e^2 n_e}{\epsilon_0 m_e}\right) \tag{5.2}$$

In practical units,

$$f_{pe} = \frac{\omega_{pe}}{2\pi} \approx 8980\sqrt{n_e}\ Hz,\ \ (n_e\ \text{in}\ cm^{-3}) \tag{5.3}$$

In this low pressure case, the electron plasma frequency is about 20 MHz.
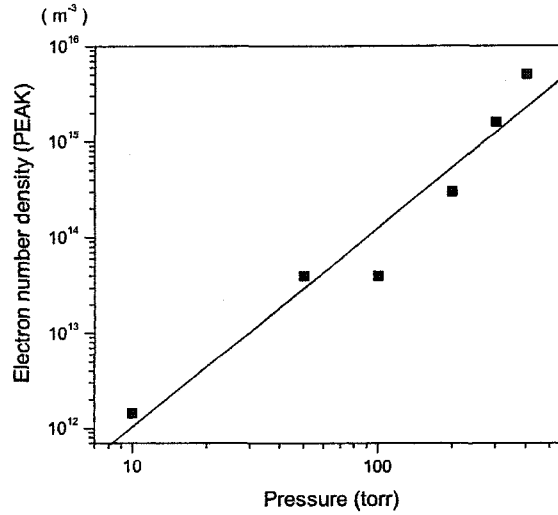
Figure 5.8: Electron number density increases with gas pressure ($log(n_e)$ vs $log(P)$)

As pressure rises in our model simulations, the number density increases dramatically. As shown in Fig. 5.8, the log of the density shows a near linear dependence on the log value of gas pressure, indicating an exponential dependence of electron density on neutral pressure.

$$n_e \propto P^k \tag{5.4}$$

where $k = 2.1 \pm 0.2$, given by the linear fitting in Fig. 5.8.

5.3   Ionization in the RF Capacitively-Coupled Lamp

In this section, a plasma formed by impact ionization is studied using PIC simulation. This ionization model has been studied in the last section without external fields, but here we will study a more realistic model that includes field and particle interactions in space and time.
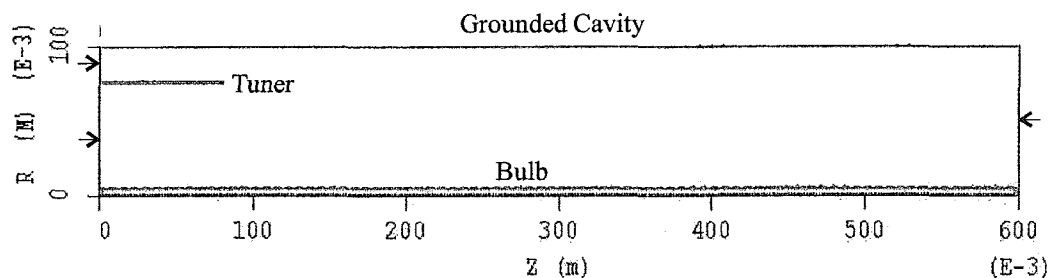
Figure 5.9: The RF lamp includes a cylindrical grounded cavity, a cylindrical tuner and a bulb in center

The geometry of the RF system is shown in Fig. 5.9, which includes a cylindrical grounded cavity with a 10 cm radius, a short cylindrical tuner (8 cm diameter) as the anode, and a dielectric jacket representing the fused silica bulb (0.5 cm diameter) disposed along the center of the cylinder axis. The arrows inside Fig. 5.9 denote the ports for incoming and outgoing electromagnetic waves.

In the present work we assume the same short E-beam (500 eV) is emitted from the left side of the bulb, which initializes neutral gas ionization. The generated charge particles immediately interact with the external field radiating between the

anode (tuner) and the cathode (ground). This model is limited in that it lacks an adequate model to account for recombination processes. Since the only particle-loss mechanism is neutralization at the dielectric wall, charged particles may build up or disappear if the net losses are not well-balanced by the ionization processes. So we examine simulation results very early in the discharge process, at around one or two RF cycles, when the effects of such build up is not significant.

We apply a voltage between the tuner and the grounded cavity which varies at the frequency of 13.56 MHz. Based on the geometry and symmetry of the lamp, X1 represents Z axis pointing along the direction of the grounded cavity axes, X2 is the radial direction for rho, and the third axis X3, which is hidden in a 2D simulation, represents $theta$. This problem represents a transverse electromagnetic (TEM) wave traveling in the third spatial dimension (azimuthally, an assumed symmetric direction). The voltage pulse supplies a radial electric field (E2). Basically the dynamic fields of interest are the E1 E2 and B3. In fact because of symmetry the B1 B2 and E3 fields are completely decoupled, and since there is no significant J3 currents (J azimuthal), B1 B2 and E3 are not generated.

Fig. 5.10 shows the E-field potential in the cavity. On the left side close to the tuner, the field is dominated by radial component E2. On the right side, downstream of the coupler, the longitudinal component E1 dominates. From these figures, we can see that it has a high potential gradient below the coupler, and the outside of the bulb is at a lower potential, ions will hit on the bulb causing quartz degrading.

We are more interested in the plasma region inside the bulb. In usual EM-PIC

Erho   Ez
(E+1)

Time 53.518 ns: X1-Integral of Ez (V/m) at OSYS$AREA

Time 53.518 ns: X2-Integral of Erho (V/m) at OSYS$AREA
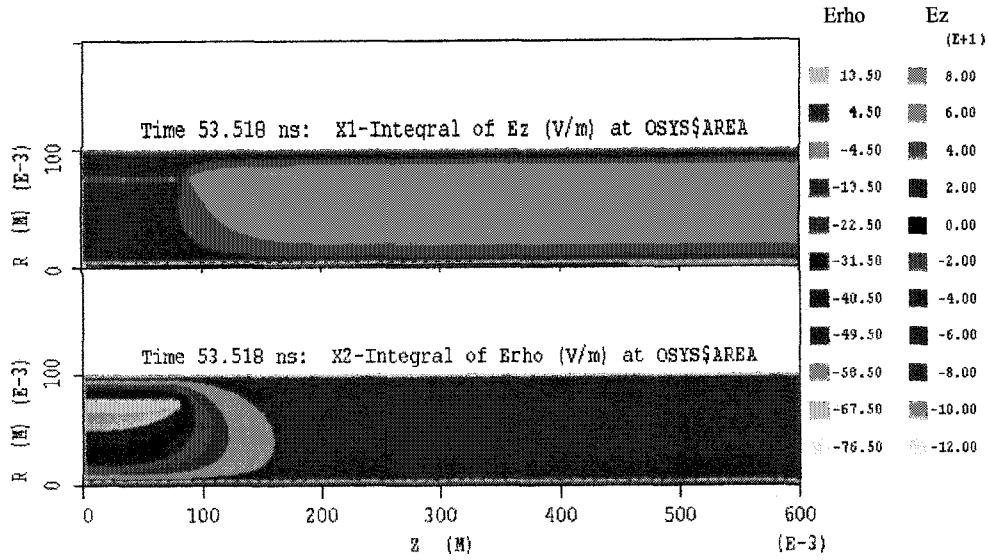
Figure 5.10: Quasi-static electric potential in the RF lamp cavity

simulations, cell aspect ratios are generally kept between 1/4 and 4/1. However, in

our problem, the bulb is 60 cm long and 0.4 cm in diameter, which results in an ex-

treme cell aspect ratio. Although this does not constitute a severe problem, probably

due to the symmetry, the radial components in our results are less meaningful than

components in the lengthways direction because of the small number of cells in that

direction. Nevertheless, the higher field on the outer annulus of the bulb corresponds

to the hollow electron density profile seen in the earlier figures.

Successful PIC simulation requires that the cell size be smaller than the Debye

length and that the time step is subject to the Courant condition, that is that it

must be smaller than the fastest natural oscillation in this (unmagnetized) plasma,

$2\pi/\omega_{pe}$ [115]. For a 10 torr xenon plasma in the RF lamp, which we will examine

here, the temperature of electrons $T_e \approx 0.27$ V, and the number density, $n_e \approx 10^6$

cm^{-3}. Substituting these values into Eq. (2.6), we obtain $\lambda_{De} \approx 0.4$ cm. This means

that the plasma, at least in the radial direction is "all sheath", and thus we do not

expect a radial quasi-equilibrium to develop at these low pressures. From Eq. (5.3),

the critical time step limit is about 50 ns. We choose $\Delta z = 2$ mm, $\Delta r = 1$ mm and

$\Delta t = 5.337026 \times 10^{-13}$ s to guarantee the Courant criterion is fulfilled.
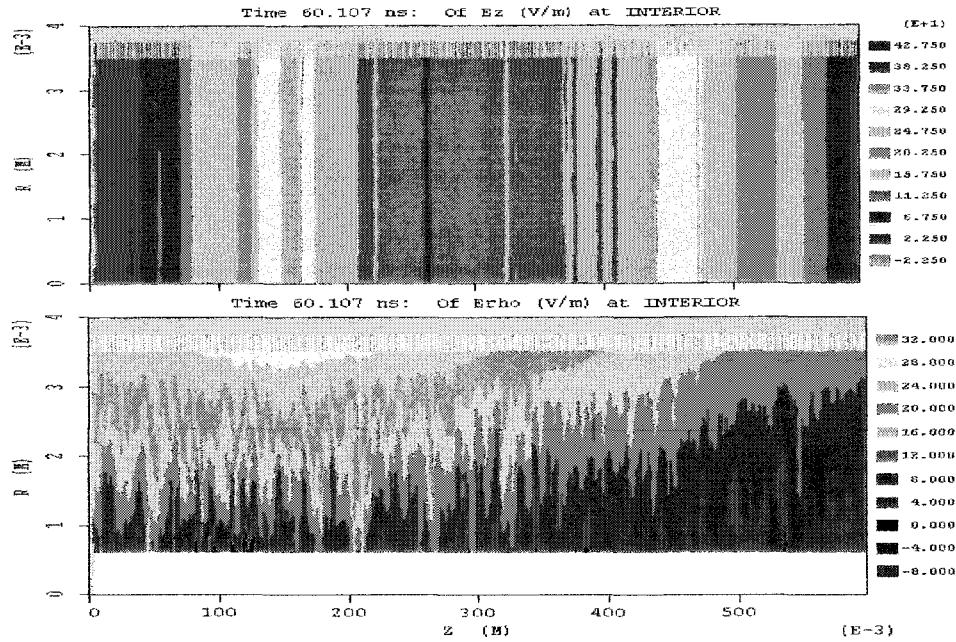
Figure 5.11: Electric field distribution in the bulb of the RF lamp

Fig. 5.11 displays the field distribution in the bulb. Again, E_{rho} dominates the

left end near the rf input coupler, and E_z is strong in the downstream side. So the

dominant motion of electrons in the bulb is along the length of the bulb, with a

superposition of radial motion on the side nearest the coupler.

The field distribution is more clearly displayed by the integral of Poynting vector

inside the bulb. Fig. 5.12 shows the curve for field power distribution which correlates
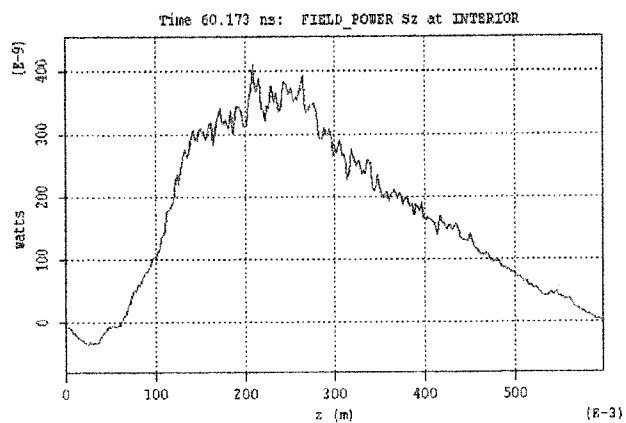
Figure 5.12: The energy flux distribution in the bulb
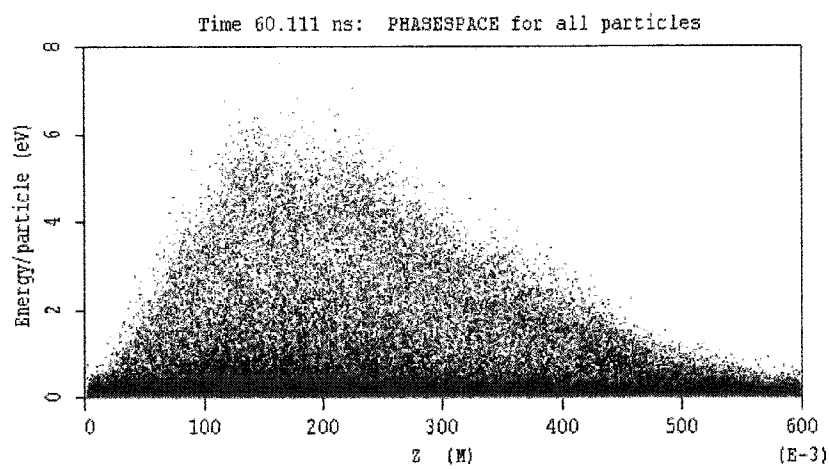
Figure 5.13: The average particle kinetic energy in the bulb. Electrons - red dots; xenon ions - blue dots

very well with the electron average energy phasespace as shown in Fig. 5.13.
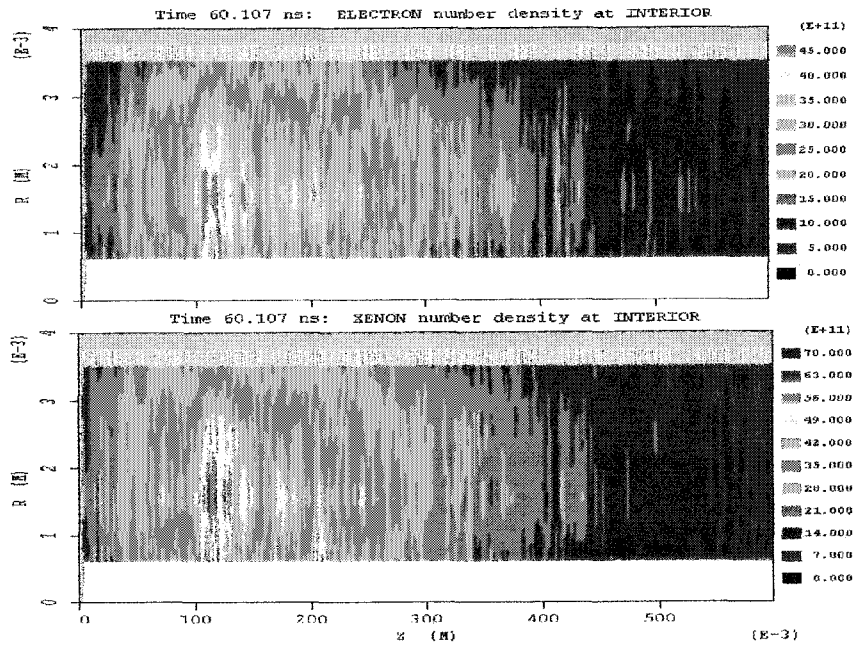
Figure 5.14: The plasma number density (in m^{-3}) distribution inside the bulb at 60.107 ns

For this 10 torr plasma driven by an RF source at 13.56 MHz, the plasma density in the bulk peaks at 4.5×10^{12} m^{-3} for electrons and 7×10^{12} m^{-3} for ions Fig. 5.14. The plasma density increases with time and finally reaches an equilibrium distribution. More importantly, we can see, since most of the energy is put right under the coupler where one can find high concentration of electron density and high energy electrons, we would expect the production of excimers within that region. We have demonstrated the importance of these hot electrons for excimer formation in the kinetic model in chapter 4.

The electron energy distribution function (EEDF) is one of the most important

fundamental characteristic within a gas discharge. For a uniform classical gas without any external forces, one may expect a Maxwellian distribution to be the equilibrium solution of the Boltzmann equation. The 1D velocity distribution along the x axis is given by

$$\frac{dG}{dv_x} = (\frac{m_e}{2\pi kT_e})^{1/2} exp\{-\frac{m_e v_x^2}{2kT_e}\} \tag{5.5}$$

The 3D form of the Maxwellian distribution function is

$$\frac{dG}{dv} = 4\pi(\frac{m_e}{2\pi kT_e})^{3/2} v^2 exp\{-\frac{m_e v^2}{2kT_e}\} \tag{5.6}$$

where v is the electron speed. Eq. (5.6) can be written as an EEDF, i.e.,

$$\frac{dG}{d\varepsilon} = \frac{dG}{dv}\frac{dv}{d\varepsilon} = \frac{2}{kT_e}\sqrt{\frac{\varepsilon}{\pi kT_e}} exp\{-\frac{\varepsilon}{kT_e}\} \tag{5.7}$$

where ε is the electron energy, usually in units of eV.

In some cases the EEDF can be fitted by a sum of two Gaussians to form a bi-Maxwellian distribution [116, 117]. Hence, two electron temperatures can be assigned. The EEDF at 80 ns is shown in Fig. 5.15. It can be represented as a sum of two Maxwellian distributions with temperatures of $T_l = 0.186 \pm 0.002$ eV and $T_h = 3.8 \pm 0.3$ eV, where T_l and T_h are the effective temperatures of the low and high energy electron groups. We note that for the low temperature group, the statistical error is very low, but how far this persists out into the curved region between the low and high energy distributions is a somewhat arbitrary choice. Thus a different

choice of upper boundary for the fit would have looked nearly as good to the eye, but would have yielded a higher temperature. Thus, although the statistical error is very small, this systematic error argues that we should allow a more generous latitude in assigning $T_e \sim 0.2$ eV+0.01/ − .015 eV to the low temperature component of the bi-Maxwellian in this simulation.
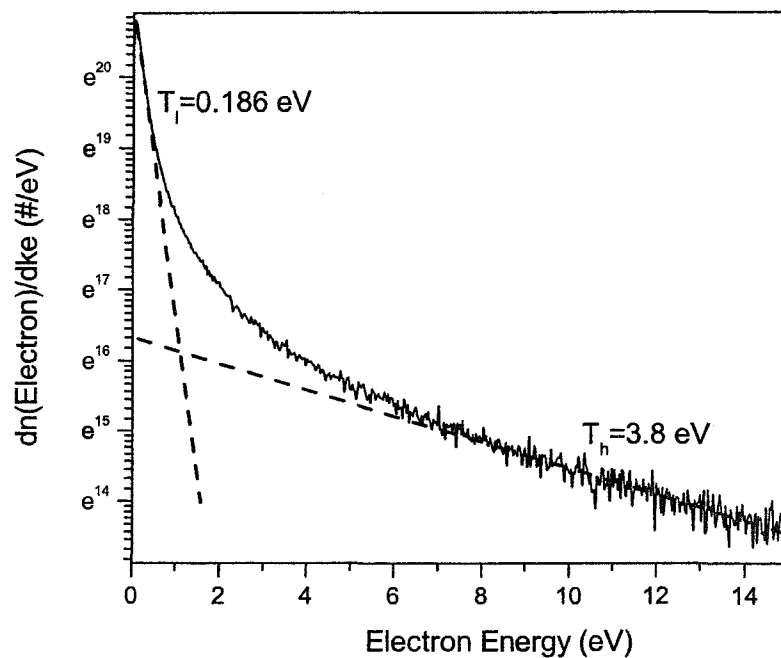
Figure 5.15: The electron energy distribution function (EEDF) in a RF discharge lamp at the neutral pressure of 10 torr at 80 ns. The broken lines represent the two-temperature Maxwellian distribution of the discharge

Fig. 5.16 shows the time history of the EEDF in the RF discharge. At the beginning electrons generated from ionization have low energy. These electrons are then accelerated by external fields, and the "hot electron tail" shows up. When this group

of hot electrons gains enough energy that exceeds the first ionization potential of xenon, (the ionization cross section becomes non-zero), collisions with neutral xenon atoms will generate more electron-ion pairs.
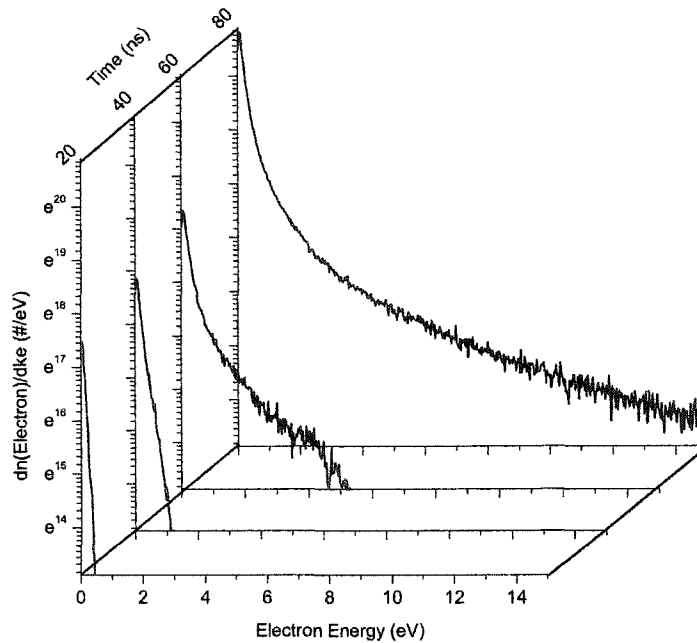
Figure 5.16: The time evolution of EEDF for the RF discharge at 10 torr

5.4 Electromagnetic Simulation of the Microwave Lamp

In this section, a microwave discharge in a rectangular cavity is simulated with the 3D PIC code. This lamp is driven by six magnetrons which directly couple to the bottom of a large "over-moded" cavity. Details about the lamp geometry are described in

Sec. 3.2.1. Fig. 5.17 shows the bottom area of the lamp with magnetrons labeled. The front view of the cross section (Fig. 5.18) shows the position of the bulb. In the present simulation, only one bulb is placed in the cavity. Because conformal objects are required by the particle statistics commands in 3D MAGIC simulation, we define a bulb with a square cross section. The small radius makes this approximation better than it otherwise might be. All particles are constrained to lie in the active spatial region defined by the inner volume of this bulb.
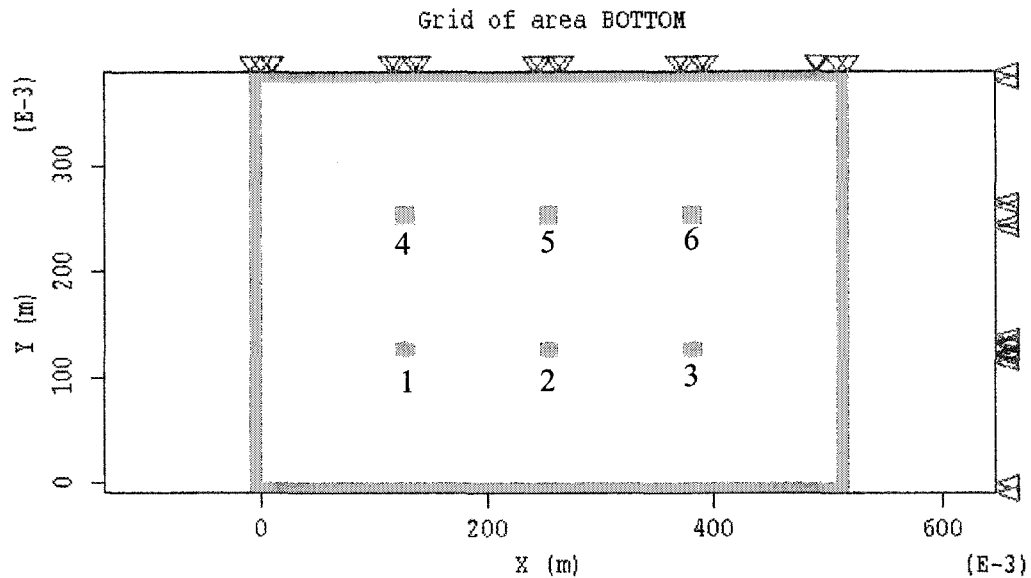
Figure 5.17: The top view of the microwave lamp cavity geometry with magnetrons labeled

The driving plasma frequency is 2.45 GHz, at 1000 V a.c.; the xenon gas pressure is fixed at 1 torr, at the temperature of 900 K. The initial condition is assume to be similar with that described in Sec. 5.2, which is an E-beam injection from one side of the bulb, followed by ionization processes, whose rate is defined by the impact

Grid of area BULBSLICE
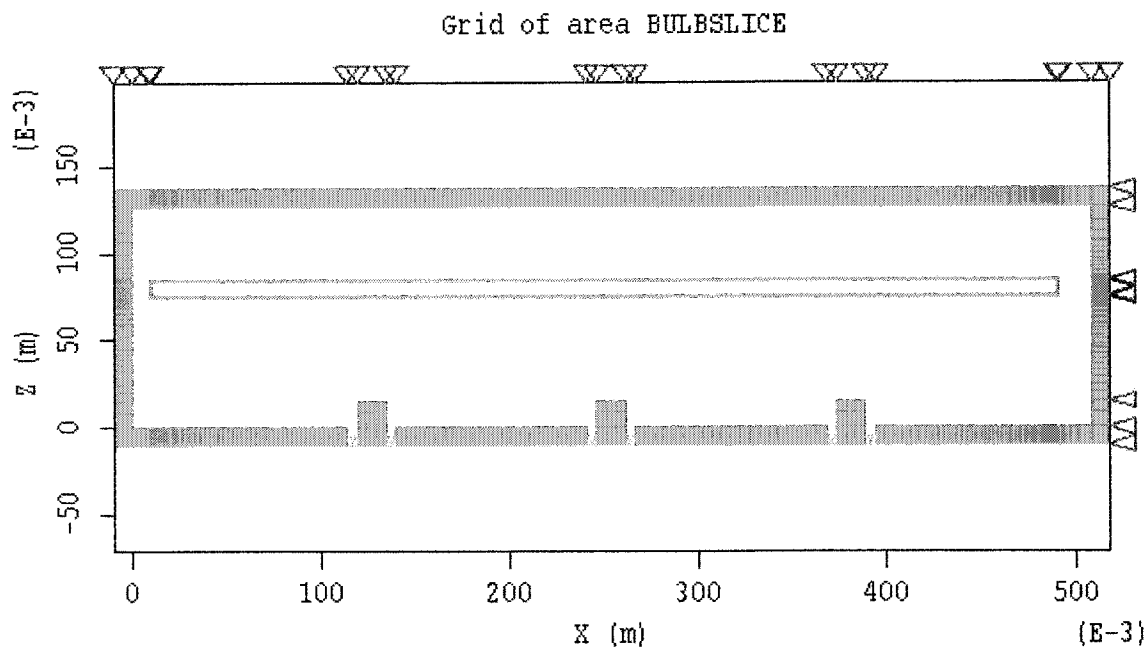
Figure 5.18: The front view of the microwave lamp cavity geometry. The lamp bulb is placed on top of the magnetron antennas at a height of 8cm

ionization cross section function. The difference between this simulation and previous rf simulation is that these charged particles are now driven by the EM fields that result from porting in microwave power to the overmoded cavity.

Fig. 5.19 is a visualization of the electric field modes depicting one of the E-field components in the XZ plane. Clearly, EM modes arise from these magnetrons that strongly couple to each other. This has the experimental consequence of synchronizing the operation of the magnetrons, which can be a problem. At the level where the bulb lies, there is no single mode dominating. When the h-f field crosses the bulb, electrons gain energy and transfer that energy to neutral or ionized gas molecules or atoms. The average power transferred per unit volume gas is defined in Eq. 2.31.
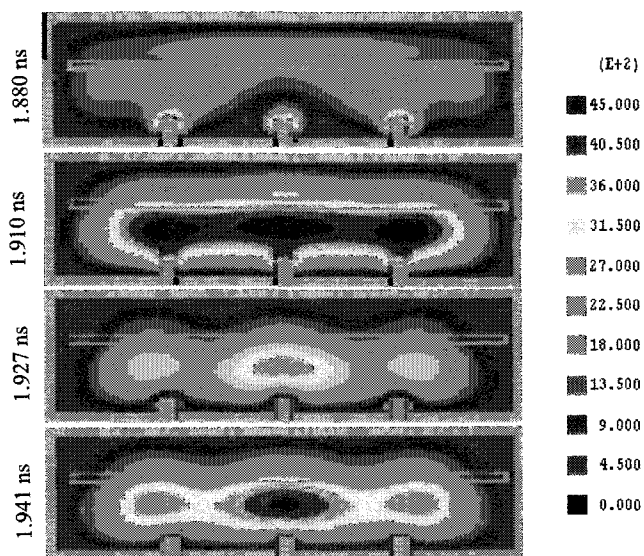
Figure 5.19: The electric field contour Ey (V/m) at the XZ plane in the microwave lamp
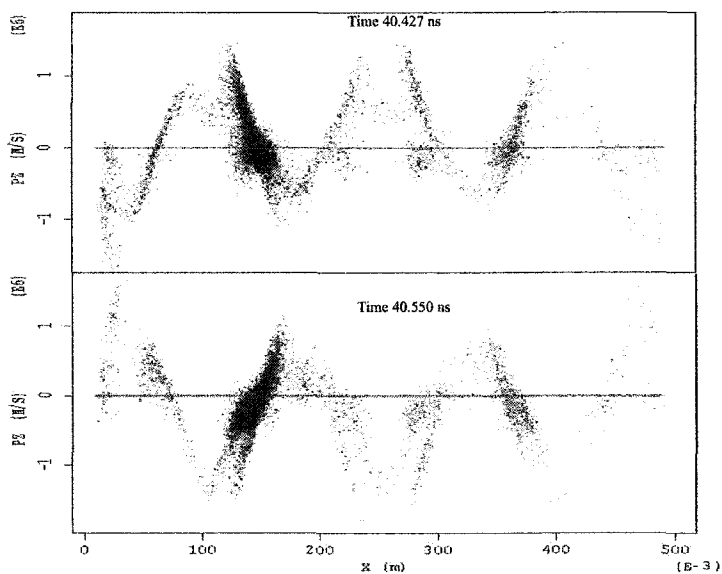
Figure 5.20: $P_z - X$ phasespace for electrons (red) and ions (blue)

Some characteristic values including the temperature and average energy for electrons and xenon ions are extracted from the simulation; results are shown in Fig. 5.21 through 5.24. The initial ionization is again caused by a very short $(8 \times 10^{-13} \text{ s})$ high-energy E-beam pulse at 500 eV. It takes about 37 ns to go through the bulb from one end to the other. Since we are more interested in the later times when electrons are in thermal equilibrium, we examine parameters many microwave cycles after 40 ns (see the inset of Fig. 5.21).
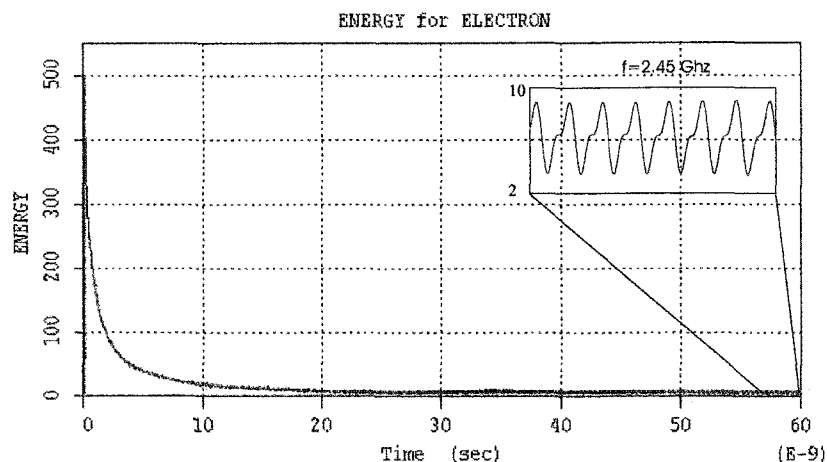
Figure 5.21: The electron energy in the microwave lamp. Equilibrium is reached after 40 ns

From Fig. 5.21 and 5.22, we see that electrons are losing energy during collisions with xenon atoms. After equilibrium, the electrons have an average energy of 6.4 eV, and the electron energy oscillates about 2 eV above and below this value, at the frequency of the driving field. The ions have much lower energy of about 0.11 eV.

Fig. 5.23 and 5.24 show that the electron temperature is about 3.8 ± 0.8 V, and the ion temperature is only 0.08 V.
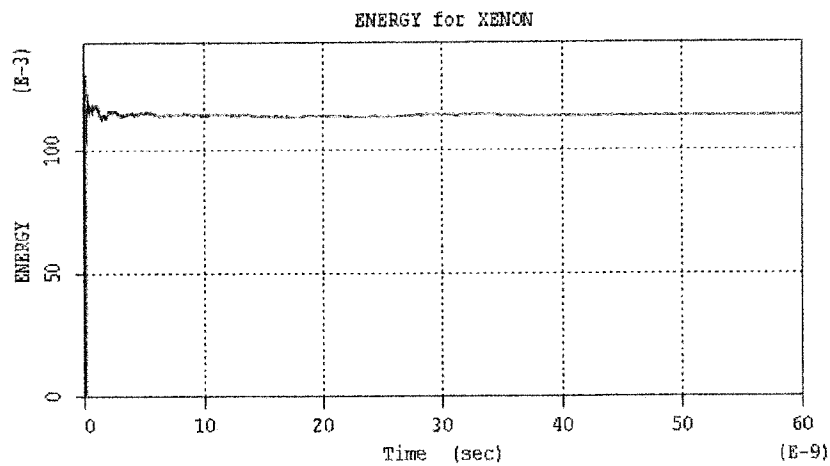
Figure 5.22: The ion energy in the microwave lamp
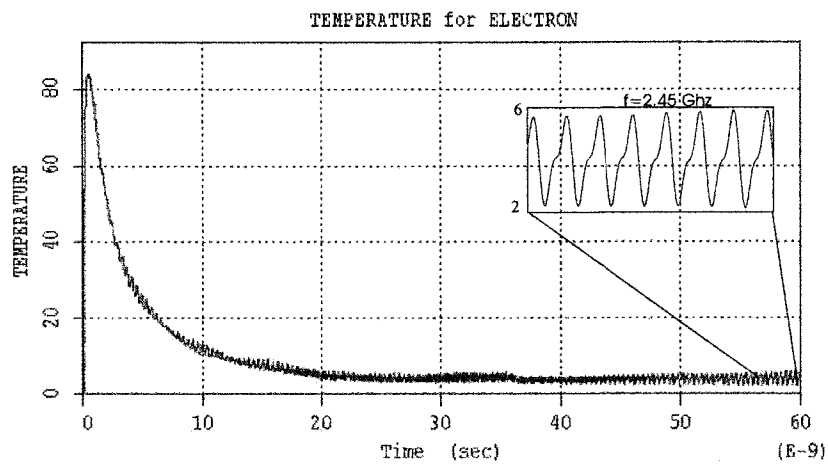
Figure 5.23: The electron temperature in the microwave lamp. Equilibrium is reached after 40 ns
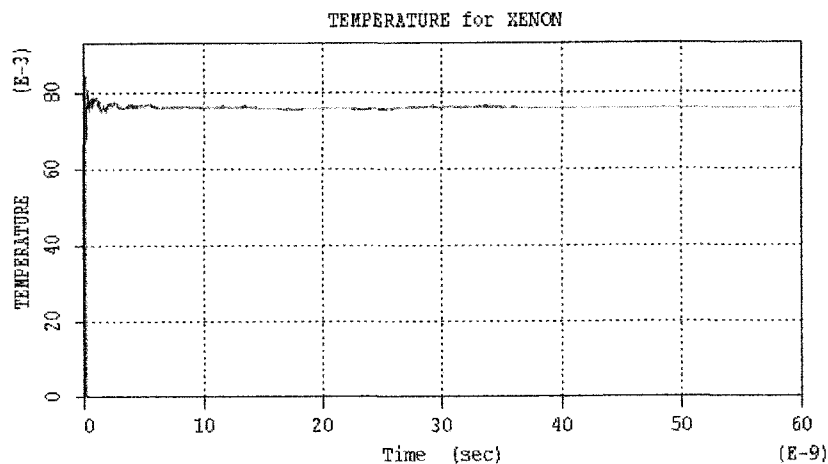
Figure 5.24: The ion temperature in the microwave lamp

5.5 Conclusions

In this chapter we have shown successful PIC simulations with impact ionization model in practical prototype plasma lamps. Issues about field distribution, particle density/temperature and EEDF are discussed.

From a fundamental point of view in the simulation, the RF lamp hasn't reached equilibrium within 60 ns. We have observed the plasma density peak in Fig. 5.14 moving downstream at about 80 ns, which is probably driven by the electric field. The electron temperature obtained from EEDF will continuously increase until reaching equilibrium.

Because of the limitation of computation resources, simulations with the ionization model in our RF and microwave lamp systems are not performed for high pressure plasmas. If computation time is not a concern, one can perform high pressure ($>$ 100 torr) calculations taking care to satisfy the Courant criterion discussed in previous

context. At high pressure, plasmas will have smaller Debye length, so one would need

smaller (and more) cells in the simulation.

Chapter 6

Gaussian Simulation

6.1 An Overview of Gaussian

Gaussian [118] is a system of programs for performing a variety of semiclassical and ab initio molecular orbital (MO) calculations. It is powerful in exploring complex molecular systems with various interests such as substituent effects, reaction mechanisms, potential energy surfaces, and excitation energies. These calculations all presume a particular choice of wavefunction basis set coupled to a specific theory model. Given the basis set from which to construct orbitals, a unique assignment of electrons to orbitals is made according to some "building up" principle. After some necessary anti-symmetrization scheme to account for the fact that electrons are fermions, these orbitals thus form a suitable many-electron wavefunction, which is the solution of the Schrödinger equation, used to predict all kinds of characteristics of molecules. In this chapter, we will begin by reviewing briefly the goals and methods of ab initio calculations, followed by the use of Gaussian 03W to explore the molecular mechanics of KrI with efforts to gain insight into the details of the physics governing light emission

136

from this species.

6.2 Interaction Potentials

Although the interaction potentials of some rare gas-halogen molecules have been well studied, the determination of ground and excited state interaction potentials for many heavy excimers have not been extensively characterized either theoretically or experimentally. The ground state interaction potential is very important for understanding emission spectra and to elucidate the transition from van der Waals binding to a stable chemical bond. A detailed knowledge of the ground state curve is also important to understand and predict the recombination of halogen atoms in rare gas buffers.

For a molecule with unknown geometric structure, it is necessary to study structural changes within a molecule which often are associated with differences in energy and various properties of interest. The way the energy of a molecular system varies with small changes in its structure is specified by its potential energy surface (PES). A potential energy surface is, in general, a multi-dimensional mathematical representation linking the resulting energy with variation in bond distances and angles. For a diatomic molecule, the potential is shown as a simple curve connecting the internuclear separation on the X-axis to the energy on the Y-axis.

Finding the optimum geometry in general requires finding the minima on the PES, thereby predicting equilibrium structures of molecules. It begins at an assumed

molecular structure specified as its input, and steps along the various primary coordinates on the PES. One computes the energy and the local gradient, which represents the net force at that location, allowing an efficient algorithm to choose the step size and direction for the next step in the optimization, which searches for local and absolute minima in the gradient. For systems with more than two dimensions, saddle points must be differentiated from true minima by evaluating the value of the second derivative of the energy with respect to the molecular coordinates. For the simple curve associated with the PES for diatomic molecules, there are no such complications and finding the minimum is very straightforward.

There are a large number of varieties of computational models for solving the Schrödinger equation, and a great multiplicity of basis set functions that are appropriate for use in each of these models, as well as user-specified basis sets customized for the task at hand. The Gaussian program contains a hierarchy of procedures corresponding to different approximation methods (different levels of theory). More accurate methods, or choices of larger basis sets within a given model, lead to correspondingly more time-consuming computations. In return, larger basis sets impose fewer constraints on electrons and more accurately approximate exact molecular orbitals.

For diatomic molecules, computational time is usually not a large concern. But since KrI is a very heavy (high-Z nuclei) molecule, the inner shell electrons are not as well decoupled from the outer shell electrons. Thus more complex methods, a higher-order theory, and bigger basis sets must be used. In addition, for the KrI case,

full electron correlation models were used.

In a many-body system, two electrons cannot be in the same place at the same time and electrons must move to avoid each other, i.e. their motion must be correlated. Hartree-Fock optimization accounts for electron correlation only in an average sense, since single electron motions occur in the average potential of all other electrons in an iterative optimization scheme. Other methods consider electron correlation as instantaneous pairwise interactions of electrons with opposite spin. This averaging approximation causes Hartree-Fock results to be less accurate in general, and in some heavy-atom cases like KrI, totally unsuitable. For the KrI simulations, I selected a large basis set "LANL2DZ" and compare the results of calculations with different theoretical models. For a given basis set, the difference between the exact energy and the Hartree-Fock energy is the correlation energy.

MP2 [119] stands for second-order Møller-Plesset perturbation theory. The theory was developed for an approximate treatment of many-electron systems in a given external field, in which the Hartree-Fock solution appears as the zero-order approximation. The first-order correction for the energy and the charge density of the system is proved to be zero. So with the standard Rayleigh-Schrödinger perturbation theory, the many-body problem was solved accurately to the second order by Møller and Plesset. MP2 is the simplest and least-expensive traditional method for incorporating electron correlation effects in ab initio electronic structure calculations [120]. However, when higher-order perturbation calculations are applied, the divergent behavior of the Møller-Plesset series becomes a problem [121]. In general, MP2 is considered

as less accurate and less robust than the best density function theory when applied to complicated correlation problems, such as transition states, and metal-containing compounds. The "Tight" option in MP2 is used to increase the precision in the MP2 energy and gradients. Tightening thresholds for computation of the atomic orbit (AO) and molecular orbit (MO) integrals usually provides better results for computing very accurate geometries or numerical frequencies.

QCISD is quadratic configuration interaction that includes determinants corresponding to single and double excitations. It is a full numerical calculation for electron correlation corrections and usually takes much more time. The QCISD method completely omits effects of triple substitutions, which is known to be important, so one can include the triples correction by using QCISD(T).

Another methods for electron correlation problems uses coupled cluster theory. It was introduced by Cizek [122] and denoted by CCSD. This set of methods use substituted configurations in a multiplicative (exponential) rather than an additive manner. It has been found that they are still effective under circumstances where perturbation theory convergence is slow. Triples correction is added in the same way as CISD. The E4T option requests an evaluation of MP4 triples in addition to the triples contribution to the energy.

Traditionally, the above three sets of methods (MP2, CISD, CCSD) are referred to as post-SCF methods because they add correlation corrections to the basic Hartree-Fock model. There is another class of electronic structure methods called density functional methods. DFT includes the effects of electron correlation, but requires

about the same amount of computation resources as Hartree-Fock theory. DFT uses

Becke exchange functional and Lee-Yang-Parr correlation functions [123], as well as

Hartree-Fock exchange. In Gaussian, it is called by using keyword "UB3LYP". DFT

is an ab initio method not based upon a wavefunction. Instead, the energy is com-

puted as a function of the electron density. Within the framework of DFT, the prac-

tically unsolvable many-body problem of interacting electrons is reduced to a solvable

problem of a single electron moving in an averaged effective force field. This effective

force field can be represented by a potential energy being created by all the other

electrons as well as the atomic nuclei, which are seen as fixed under BOA. Because of

these appealing features, DFT is proven to be one of the most popular and successful

quantum mechanical approaches to the many-body problems either in molecular or

condensed matter systems.

Theory	Atom separation at minimum(Å)	Energy(a.u.)	Dipole(Debye)
MP2	5.6648	-29.0417944	0.0002
MP2 (Tight)	5.5927	-29.0461796	0.0003
QCISD(T)	5.5846	-29.0228258	0.0089
QCISD	5.6202	-29.0228259	0.0002
CCSD(T)	5.5846	-29.0228258	0.0089
CCSD	5.6211	-29.0228259	0.0002
CCSD(T,E4T)	5.5846	-29.0228259	0.0002
UB3LYP	5.8608	-29.4828956	0.0001

Table 6.1: Geometry optimization with basis set "LANL2DZ"

Within the DFT model, we computed the energy using various basis sets to ex-

amine the differences between them. Table 6.2 lists the results for these calculations

with increasing basis set size.

Basis Set	Atom separation at minimum(Å)	Energy(a.u.)	Dipole(Debye)
STO-3G	3.3657	-9576.84496294	0.8805
3-21G	3.7408	-9631.50967693	0.5032
CEP-4G,31G,121G	6.5357	-29.79512432	0.0017
LanL2MB	5.9253	-29.48224816	0.0006
LanL2DZ	5.8608	-29.48289559	0.0001
SDD,SDDAll	5.9358	-29.78857199	0.0153

Table 6.2: Geometry optimization with DFT calculation

With the first two basis sets shown in table 6.2, the magnitudes of the calculated energies are unrealistically large, indicating that the STO-3G and 3-21G are too small for KrI. The other basis sets yield similar results for internuclear distances between 5Å and 6Å. However, we are in need of the short distance values, because KrI is a very repulsive system, and we are simulating high energy collisional processing as well as rapid bond dissociation associated with radiative (impulsive) population of the lower state curve from above.

We used Gaussian to perform a series of single point energy calculations over sampled points on the potential energy surface, using all of the available levels of theory appearing in the table of results. We found that the various theory models, subject to the same convergence conditions, yielded nearly identical potential energy curves (see Fig. 6.1). None of these curves predict even a weakly bound ground state, that is, we observe no shallow potential well for KrI ground state. Although the ground states of all noble gas halides are usually very repulsive, very often there is still a shallow potential well, representing a very weak bond, so in this respect KrI stands out.
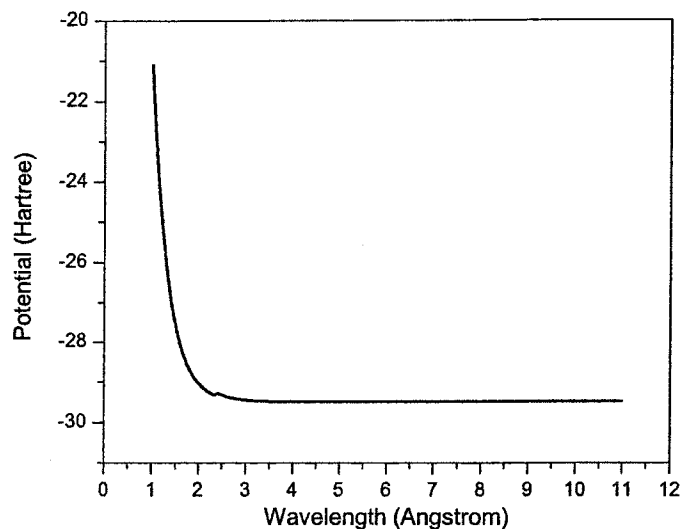
Figure 6.1: KrI 1-D scan of the potential energy curves using different theory models (SCF, MP2, MP3 QCISD, QCISD(T)) coincides. No potential well, indicative of a bound state, was observed.

Molecular orbitals can be constructed from neutral atom basis sets, or from sets that represent ionic states of the atoms. Intermediate sets allow for highly polarized molecules, such as inert gas halides, that may approach a more nearly ionic bond in the gas phase. To provide more accurate descriptions of these ions-like neutral states in molecules, basis sets may be augmented with so-called diffuse functions, which have a radial dependence of $exp(-\alpha r^2)$. Here α is the exponent, designed to represent the diffuse form of the radial density around the atomic core. The range of the orbital that corresponds to a Gaussian function is thus proportional to $\alpha^{-1/2}$. This addition of diffuse terms is intended to improve the basis set at large distances from the nuclei, thus better describing electrons that are at sufficient distance from the core that they

are barely bound. This is a necessary expedient for heavy atoms when relativistic effects of rapidly moving inner shell electrons become significant.
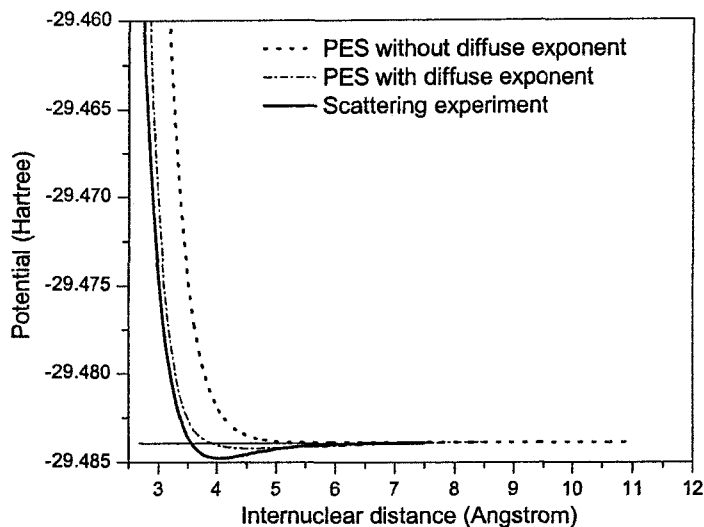
Figure 6.2: Comparison of experiment result with the B3LYP/LANL2Dz ground state potential energy curve for KrI with and without diffusion components

Check and co-workers [124] supplemented polarization and diffuse functions for p-block elements including iodine. Wilson et al. [125] reported the exponents for krypton extrapolated from the values of the preceding atoms. On convergence of our calculations, we obtained the ground state PES for KrI with the diffuse exponents $\alpha_I = 0.0278$ and $\alpha_{Kr} = 0.065145$. Fig. 6.2 compares the results for the calculated potential curves with those extracted from the atom scattering experiment of the group of Y. T. Lee [84]. Failing to correct for polarization effects, by not including diffuse exponents leads to significant disagreement with experiments. As can be seen, the curve obtained with the values of diffuse exponents listed above agrees well with

experiments over this range of internuclear separation.

	Potential energy gradient at 3.2Å (kcal/mol Å^{-1})	Potential minimum of the ground state (Å)
Scattering experiment	11.8	4.05
Gaussian with diffuse exponent	15.9	4.6
Gaussian without diffuse exponent	41.7	5.86

Table 6.3: Comparison of the potential curve gradient and minimum between Gaussian calculation and scattering experiments

The lower limit on separation in the scattering experiments was limited by the upper limit of the available speed of the nozzle beam of neutrals in the scattering experiment. The collision energies specified in the experiments were 0.28 eV and 1.62 eV. The obtained potential curve from the low energy experiment is accurate for internuclear distance larger than 3Å. At higher scattering energy, the data reflect the scattering mainly from the repulsive part of the potential with the distance larger than 2.5Å. The other part of the curve was estimated by fitting to an analytic form (Morse-Morse-switching function-van der Waals). Their values for the steep potential energy gradient in the Franck-Condon region and the ground state potential minimum are compared to our Gaussian calculation results in table 6.3. These values determine the line shape and intensity of the transitions to the ground state by reflecting the relation between the upper state and the ground state potentials.

The good agreement we observe gives us greater confidence that extensions of this calculation to smaller radii will yield curves that can be trusted to simulate

higher energy events in our plasma driven systems. Equally important, we note that the inclusion of diffuse exponents yields a weakly bound state, in somewhat better agreement with the scattering data. If it were our intent to simulate the fine features of angle-scattering at low energy, larger bases, and a more refined computational model would be required to more exactly reproduce the region near 3.8Å.

6.3   Molecular Orbitals and Electron Density

Visualization of molecular orbitals is useful for qualitative understanding of the electron density distribution in molecules, and for understanding much of the physics governing their behavior in plasma systems, in reactive collisions, and in various types of photo-transitions. In Gaussian, the theoretical models are all based on various molecular orbital theories, although it is important to remember that these will at best be approximations to the actual wavefunctions of molecular states [126]. In practical calculations, the molecular orbitals ψ_i are often defined as linear combinations of a set of N one-electron functions ϕ_u,

$$\psi_i = \sum_{u=1}^{N} c_{ui}\phi_u \tag{6.1}$$

where the functions $\phi_1, \phi_2, ..., \phi_N$ are members of the one-electron basis function set spanning the Hilbert space of the Schrödinger operator.

In such calculations, electron spin is incorporated either in an open shell model, also known as "unrestricted orbitals", or in a closed shell model, also known as "re-

stricted orbitals". Closed shell molecules, will always have an even number of electrons, and thus this grouping can be divided into pairs of opposite spin. So each orbital is doubly occupied by electrons, one spin up, the other spin down. Open shell systems which have at least one unpaired spin, and so are usually modeled by an unrestricted model, wherein each electron, whether spin up, or spin down, occupies a separate spatial orbitals. Spin up orbitals are given the designation α orbitals, spin down orbitals are called β orbitals. Unrestricted calculations are not only used for molecules with odd numbers of electrons. They are also used for calculation of certain excited state configurations, to calculate systems with abnormal or unusual electronic structures, and for calculation of processes such as bond dissociation, which simulates the spatial separation of an electron pair.

Krypton has 36 electrons and iodine has 53 electrons, so that the resulting molecular form, KrI, containing 89 electrons, requires the use of an unrestricted model. In Gaussian, after optimizing the geometry, the molecular orbitals can be visualized from various outputs (known as check files) associated with the B3LYP/LanL2DZ calculation.

We examined the highest occupied molecular orbits (HOMO) for both α and β orbitals of KrI. The HOMO's of α and β orbitals are so nearly identical that they are indistinguishable when plotted, as seen in Fig. 6.3. These orbitals are dominated by the iodine p orbitals of the iodine atom. The introduction of the krypton atom perturbs the iodine resonant states, $5p^2 P_{3/2,1/2}$ to form the molecular states of KrI.

The molecular electrostatic potential is the potential energy of a proton at a par-
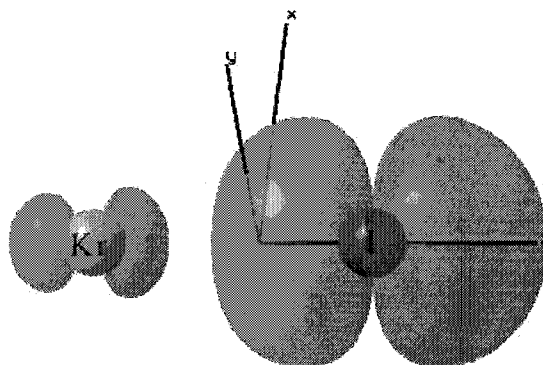
Figure 6.3: The HOMO of KrI α orbital shows that the iodine atomic orbital p_z is perturbated by the krypton atom to form a molecular orbital. The HOMO of KrI β orbital is nearly identical as α

ticular location near a molecule. The electrostatic potential correlates with dipole moment, electronegativity, and partial charges. It provides a visual method to understand the relative polarity of a molecule. Fig. 6.4 depicts only a portion close to the center of the KrI molecule with some edges truncated. The negative electrostatic potential corresponds to an attraction of the proton by the concentrated electron density in the molecules (colored in shades of brown). The positive electrostatic potential corresponds to repulsion of the proton by the atomic nuclei in regions where low electron density exists and the nuclear charge is incompletely shielded (color in shades of purple).

Fig. 6.5 shows the electron density distribution within the molecular system. As can be seen, electrons have been withdrawn towards the iodine atom, which makes it slightly negatively charged, leaving the krypton atom positively charged. The electrostatic potential on the resulting electron density surface is indicated by different
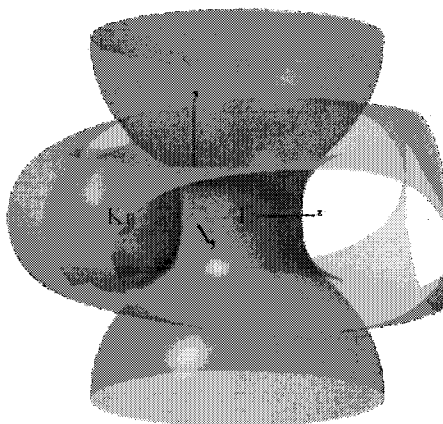
Figure 6.4: The electrostatic potential surface of KrI

colors. Clearly there is a net polarization of the molecule that leaves a surplus of electrons on the iodine, and a corresponding deficit on the Kr. A classical electrostatic interpretation of the chemical bond will regard a molecule as two or more nuclei imbedded in a rigid three-dimensional distribution of negative charges. With this picture, the repulsive force between nuclei is balanced by an attractive force exerted by the negatively-charged electron density distribution. A chemical bond is thus the result of the accumulation of negative charge density in the region between the nuclei to an extent sufficient to balance the nuclear forces of the repulsion.

6.4 Summary

Potential energy curves represent the atomic interactions within a molecular system at a certain state. Most spectroscopic results can be obtained from potential curves. In this chapter we introduce a simulation approach to obtain this information for
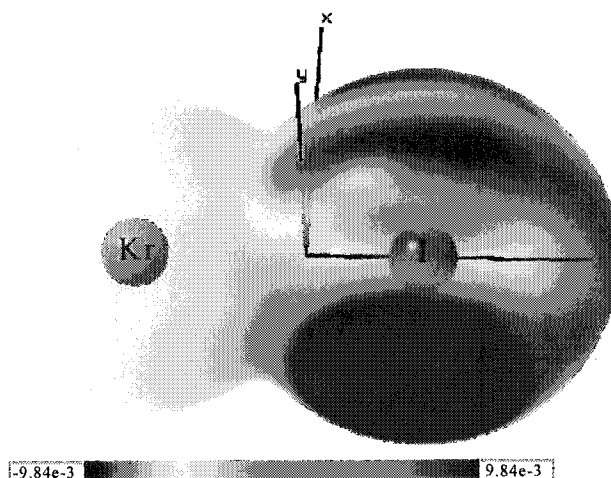
Figure 6.5: The electron density of KrI from SCF calculation. The colors mark different electrostatic potential values

unknown molecular systems such as KrI. The result is in reasonable agreement with the scarce scattering experiment results. Our Gaussian simulations for the KrI ground state indicate that the X potential must be steeper in the Franck-Condon region than found from previous scattering experiments. With an accurate potential curve, one will be able to study various important aspects such as transition rates, intensities, and line shapes and estimate molecular constants related to these transitions. We will show a semiclassical approach to deal with RgX transitions in the next chapter. The molecular orbitals, electrostatic potential surfaces and electron density distribution will be very useful in analysis of molecular polarization, bonding, and reaction path in different state.

Chapter 7

Semiclassical Line Shape

Simulation

Rare gas halide emission spectra have been an attractive topic for several decades. Several groups have developed a variety of excitation techniques and there have been simulation models to study the molecular dynamics of their emissions. But experimental data for KrI spectra are scarce, and there has not been a prior comprehensive theoretical study of the reaction dynamics. In this chapter, we provide a semiclassical model and derive an explicit expression for the excimer spectral line shape for the RgX systems. The model and calculations are applied to KrI* emission studies and the results of comparison the simulation results with experimental data of high-pressure KrI* obtained in our novel 13.56 MHz excimer lamp system are reported. This model provides semi-quantitative estimates for the governing potential functions associated with the ground and excited states.

151

7.1   Derivation

Our approach to modeling the excimer systems will be to use semiclassical methods to estimate transition probabilities for comparison to observed intensities [127]. Analogous methods are described by Child [128]. For KrI, the angular momentum coupling properly lies at some intermediate between Hund's case (b) and case (c), and probably closer to case (c). Nevertheless, within the accuracy of our formulas, we may label states as though they belong to Hund's case (b), in order to provide a closer correspondence to the better-known light atom excimer potentials.

We consider a single excited electronic state, vibrationally bound with a potential well a few eV deep, and a single repulsive electronic ground state. Using the Born-Oppenheimer approximation (BOA), the dipole matrix element separates into an electronic factor times a Franck-Condon factor. The latter can be calculated by approximating the nuclear wave functions as a Gaussian function (for the bound state) and an Airy function (for the free state). The resulting integral is easily evaluated in a closed form by a transformation to momentum space. In this derivation, we eliminate unnecessary details by considering the case that the electronic states both have zero total angular momentum.

Our derivation is very similar with the one used by Stueckelberg [129] back to 1932 to study the absorption band in oxygen. However, stueckelberg's model is based on the assumption that the wavefunctions are different from zero only in the immediate neighborhood of the bound state equilibrium position, so that the integral for dipole

matrix element can be Taylor expanded to its first order. In our derivation, we keep

the integral form of the dipole matrix element, and only expand the effective final

state within Franck-Condon region in order to obtain the wavefuntion, which makes

our model more applicable for general cases.

The rate of photon emission, which determines the intensity, I_{em}, of a spectral

line is proportional to the Einstein coefficient A for spontaneous emission [130].

$$A = \left(\frac{64\pi^4 \nu^3}{3hc^3} \right) |D|^2 \qquad (7.1)$$

where D is the dipole matrix element given by

$$D = \left\langle \psi_f \left| \sum_{i=0} q_i \vec{r}_i \right| \psi_i \right\rangle \qquad (7.2)$$

Here the summation is over all particles including electrons and nuclei, i.e., $\sum q_i \vec{r}_i =$

$\sum -e\vec{r}_j + \sum q_n \vec{R}_n$. According to the Born Oppenheimer Approximation (BOA), the

initial state wavefunction ψ_i and the final state wavefunction ψ_f can be written as

a product of two parts corresponding to the nuclei and electrons. In this section we

will review the essential features of the BOA calculation, following the treatment of

Straughan et. al. [131], wherein the electron problem is solved for ϕ at each value

of a fixed internuclear separation. Thus the Schrödinger equation yields separable

solution for χ and ϕ.

$$\psi_{i,f} = \underbrace{\chi(\vec{R})}_{nuclei} \underbrace{\phi(\vec{r}, \vec{R})}_{electrons} \qquad (7.3)$$

where $\vec{R}$ is the internuclear separation and $\vec{r}$ is the coordinate for all electrons.

When we evaluate the dipole matrix element Eq. (7.2) $D = < \chi_f\phi_f | \sum_{i=0} q_i\vec{r}_i|\chi_i\phi_i >$, the electric dipole moment μ can be divided into two components, the first for the electrons $\mu_e(= \sum_j -e\vec{r}_j)$, and the second for the nuclei $\mu_n(= \sum_n q_n\vec{R}_n)$. Thus D is given by two parts corresponding to the integrals of the dipole moments for electrons and nuclei:

$$D = \left\langle \chi_f\phi_f \left| \sum_j -e\vec{r}_j \right| \chi_i\phi_i \right\rangle + \left\langle \chi_f\phi_f \left| \sum_n q_n\vec{R}_n \right| \chi_i\phi_i \right\rangle \qquad (7.4)$$

Since ϕ_f and ϕ_i belong to different electronic states, each of which is an independent solution of an eigenvalue problem, they must be orthogonal to one another and therefore

$$\left\langle \chi_f\phi_f \left| \sum_n q_n\vec{R}_n \right| \chi_i\phi_i \right\rangle = \left\langle \chi_f \left| \sum_n q_n\vec{R}_n \right| \chi_i \right\rangle < \phi_f|\phi_i >= 0 \qquad (7.5)$$

The other term can be averaged to give an effective dipole moment, $\vec{d}(\vec{R})$.

$$D = \int \chi_f^*(\vec{R}) \underbrace{\left[\int \phi_f^*(\vec{r}, \vec{R}) \left(\sum_j -e\vec{r}_j \right) \phi_i^*(\vec{r}, \vec{R})d\vec{r} \right]}_{\vec{d}(\vec{R})} \chi_i(\vec{R})d\vec{R} \qquad (7.6)$$

In the most general case, the nuclear wavefunction can be further separated into radial and angular parts, yielding vibrational and rotational factors, with associated overlap integrals in each of these separated coordinates. For states with $\Omega = 0(\Lambda = 0, \Sigma = 0)$, $\vec{d}(\vec{R})$ points along the internuclear axis and the electronic wavefunctions are cylindrically symmetric. So we may write

$$\vec{d}(\vec{R}) = \hat{R}d(R) \tag{7.7}$$

where $d(R)$ represents the magnitude of the integral of the electric dipole over the electronic wavefunctions, and $\hat{R}$ is a unit vector indicating the direction of the electric dipole moment D. The main contributions to the integral in Eq. (7.6) arise where the integrand $d(R)$ is slowly varying [132], so we can assume $d(R)$ is constant over the range where $\chi_{i,f}(\vec{R})$ is significant, and therefore

$$D = d(R_{eq}) \int \chi_f^*(\vec{R})\hat{R}\chi_i(\vec{R})d\vec{R} \tag{7.8}$$

where R_{eq} is the internuclear separation of the upper state minimum.

We further define j_f as the quantum number for the final rotational angular momentum (J_f) of the dissociating molecule. Under the semiclassical approximation, $J_f^2 = j_f(j_f + 1)\hbar^2 \approx (j_f + 1/2)^2\hbar^2$. We can define J_i and j_i for the upper state in the same way.

Separating the nuclear wavefunctions into radial and angular (rotation) factors, we write:

$$\chi(\vec{R}) = u(J, R)Y_{jm}(\Theta, \Phi) \tag{7.9}$$

Allowing that $d(R_{eq})$ is approximately constant, the dipole matrix element D can be written as

$$D = d(R_{eq}) \int u_i(J_i, R) u_f(J_f, R) R^2 dR \int Y_{j_i m_i}(\Theta, \Phi) \hat{R} Y_{j_f m_f}(\Theta, \Phi) \sin \Theta d\Theta d\Phi$$

$$(7.10)$$

The angular integrals, in Hund's case (b), give selection rules for the angular momentum, and for its projection on the internuclear axis.

$$\Delta j = \pm 1, \Delta m = \pm 1, 0 \qquad (7.11)$$

Now the dipole matrix element is proportional to the radial integral,

$$D = d(R_{eq}) \int [R \cdot u_i(j_i, R)][R \cdot u_f(j_f, R)] dR \qquad (7.12)$$

Defining $w_{i,f}(j_{i,f}, R) = R \cdot u_{i,f}(j_{i,f}, R)$, then the final state $w_f(j_f, R)$ must also satisfy the following Schrödinger equation.

$$\left\{ \frac{d^2}{dR^2} + \frac{2\mu}{\hbar^2} \left[E_f - \left(V_f(R) + \frac{J_f^2}{2\mu R^2} \right) \right] \right\} w_f(j_f, R) = 0 \qquad (7.13)$$

We can Taylor expand the effective potential of the final state $V_f^{eff}(R) = V_f(R) + J_f^2/2\mu R^2$ to first order around R_{eq}.

$$V_f^{eff}(R) \approx \left(V_f(R_{eq}) + \frac{J_f^2}{2\mu R_{eq}^2} \right) - F_{j_f}(R - R_{eq}) \qquad (7.14)$$

where

$$F_{j_f} = -\frac{d}{dR} \left(V_f(R) + \frac{J_f^2}{2\mu R^2} \right)_{R_{eq}} = \left[F_0(R_{eq}) + \frac{J_f^2}{\mu R_{eq}^3} \right] \qquad (7.15)$$

with $F_0(R_{eq})$ being the force in the ground state, evaluated at the equilibrium distance of the excited state, and $J_f^2/\mu R_{eq}^3$ the effective repulsive-force arising from the presence of a non-zero angular momentum associated with rotation in the molecule ("centrifugal force").

Defining

$$
\begin{aligned}
x &= R - R_{eq} \\
\Xi &= E_f - V_f(R_{eq}) - \frac{J_f^2}{2\mu R_{eq}^2}
\end{aligned}
\tag{7.16}
$$

The Schrödinger equation [Eq. 7.13] for the lower state is simplified as

$$
\left[\frac{d^2}{dx^2} + \frac{2\mu}{\hbar^2}(\Xi + F_{j_f}x) \right] w_f(j_f, x) = 0
\tag{7.17}
$$

Further defining

$$
\begin{aligned}
y &= C(\Xi + F_{j_f}x) \\
C &= -\left(\frac{2\mu}{\hbar^2 F_{j_f}^2} \right)^{\frac{1}{3}}
\end{aligned}
\tag{7.18}
$$

and substituting these into Eq. (7.17), it yields a standard differential equation (Airy)

$$
\left(\frac{d^2}{dy^2} - y \right) w_f(j_f, y) = 0
\tag{7.19}
$$

whose solution is an Airy function.

$$w_f(j_f, y) = C_f Ai(y) \qquad (7.20)$$

where C_f is a constant, independent of y. A more detailed analysis shows that C_f has only a weak dependence on j_f and E_f, and we neglect those dependences.

For the excited state, Taylor expansion of the potential energy about R_{eq} leads to the Schrödinger equation for a harmonic oscillator,

$$\left[-\frac{\hbar^2}{2\mu}\frac{d^2}{dx^2} + V_i^{eff}(R_{eq}) + \frac{1}{2}kx^2 \right] w_i = E_i w_i \qquad (7.21)$$

where $V_i^{eff}(R_{eq}) = V_i(R_{eq}) + J_i^2/2\mu R_{eq}^2$. The solution of this standard equation (Hermite) is

$$w_i = C_i e^{-\alpha x^2} \qquad (7.22)$$

where

$$C_i = \left(\frac{\mu\omega_e}{\hbar\pi}\right)^{\frac{1}{4}}, \alpha = \frac{\mu\omega_e}{2\hbar}, \omega_e = \sqrt{\frac{k}{\mu}} \qquad (7.23)$$

Substituting Eq. (7.20) and Eq. (7.22) into Eq. (7.12), we get the integral expression for the dipole matrix element D.

$$D = d(R_{eq}) \int w_i(R)w_f(R)dR = C_i C_f d(R_{eq}) \int e^{-\alpha x^2} Ai[y(x)]dx \qquad (7.24)$$

By transforming from coordinate to momentum space, this integral is easily evaluated. To do this we use the Fourier transformation and avail ourselves of an integral expression for the Airy function.

$$\int w_f^*(x)w_i(x)dx = \int \widetilde{w}_f^*(p)\widetilde{w}_i(p)dp \tag{7.25}$$

where

$$\widetilde{w}(p) = \frac{1}{\sqrt{2\pi\hbar}} \int e^{-ipx/\hbar}w(x)dx \tag{7.26}$$

So the wavefunction for the upper state in momentum space is

$$\widetilde{w}_i(p) = \widetilde{C}_i e^{-\widetilde{\alpha}p^2} \tag{7.27}$$

with

$$
\begin{aligned}
\widetilde{C}_i &= \frac{C_i}{\sqrt{2\alpha\hbar}} \\
\widetilde{\alpha} &= \frac{1}{4\alpha\hbar^2}
\end{aligned}
\tag{7.28}
$$

Evaluation of the Airy function can be found in standard mathematics handbooks, [133]
$(3a)^{-1/3}\pi Ai[\pm(3a)^{-1/3}x] = \int_0^\infty cos(at^3 \pm xt)dt$, we have

$$Ai(y) = \frac{1}{2\pi} \int_{-\infty}^{\infty} e^{i(s^3/3+ys)}ds \tag{7.29}$$

So with $w_f(x) = C_f Ai[y(x)]$, we have

$$
\begin{aligned}
\widetilde{w}_f(p) &= \frac{1}{\sqrt{2\pi\hbar}} \int e^{-ipx/\hbar} C_f Ai[y(x)] dx \\
&= \frac{C_f}{\sqrt{2\pi\hbar}} \int dx \cdot e^{-ipx/\hbar} \frac{1}{2\pi} \int ds \cdot e^{i[s^3/3 + y(x)s]} ds \\
&= \frac{1}{2\pi} \frac{C_f}{\sqrt{2\pi\hbar}} \int ds \cdot e^{i\frac{s^3}{3}} \int dx \cdot e^{-ix\frac{p}{\hbar} + iy(x)s} \\
&\quad (from Eq.\ (7.18), y = C(\Xi + F_{j_f} x)) \\
&= \frac{1}{2\pi} \frac{C_f}{\sqrt{2\pi\hbar}} \int ds \cdot e^{i\frac{s^3}{3}} e^{isC\Xi} \underbrace{\int dx \cdot e^{ix(sCF_{j_f} - \frac{p}{\hbar})}}_{\frac{\sqrt{2\pi}}{CF_{j_f}} \delta\left(s - \frac{p}{\hbar CF_{j_f}}\right)} \\
&= \frac{C_f}{2\pi\sqrt{\hbar C F_{j_f}}} exp\left[i\left(\frac{1}{3}\frac{p^3}{(\hbar CF_{j_f})^3} + \frac{p \cdot \Xi}{\hbar F_{j_f}}\right)\right]
\end{aligned}
$$

(7.30)

Hence the solution for the lower state in the momentum space is

$$
\widetilde{w}_f(p) = \widetilde{C_f} e^{i(a\frac{p^3}{3} + bp)}
$$

(7.31)

where

$$
\begin{aligned}
\widetilde{C_f} &= \frac{C_f}{2\pi\sqrt{\hbar C F_{j_f}}} \\
a &= \frac{1}{(\hbar C F_{j_f})^3} \\
b &= \frac{\Xi}{\hbar F_{j_f}} \\
C &= -\left(\frac{2\mu}{\hbar^2 F_{j_f}^2}\right)^{\frac{1}{3}} \hookrightarrow (from\ Eq.\ (7.18))
\end{aligned}
$$

(7.32)

From Eq. (7.24) and Eq. (7.25), the integral expression for the dipole matrix

element D in momentum space is

$$
\begin{aligned}
D &= d(R_{eq})\widetilde{C_f}\widetilde{C_i}\int e^{-\widetilde{\alpha}p^2}e^{i(a\frac{p^3}{3}+bp)}dp \\
&= d(R_{eq})\widetilde{C_f}\widetilde{C_i}\int e^{i(a\frac{p^3}{3}+i\widetilde{\alpha}p^2+bp)}dp
\end{aligned}
\tag{7.33}
$$

By translating coordinates $p' = p - p_0$, we can eliminate the quadratic term in the exponent. Then the integral comes to a product of an Airy Function times an exponential function. The result can be seen in Fig. 7.1), and has the form:

$$
D = d(R_{eq})\widetilde{C_f}\widetilde{C_i}a^{-\frac{1}{3}}2\pi Ai\left(\frac{\widetilde{\alpha}^2/a+b}{a^{1/3}}\right)exp\left(\frac{2\widetilde{\alpha}^3}{3a^2}+\frac{b\widetilde{\alpha}}{a}\right)
\tag{7.34}
$$
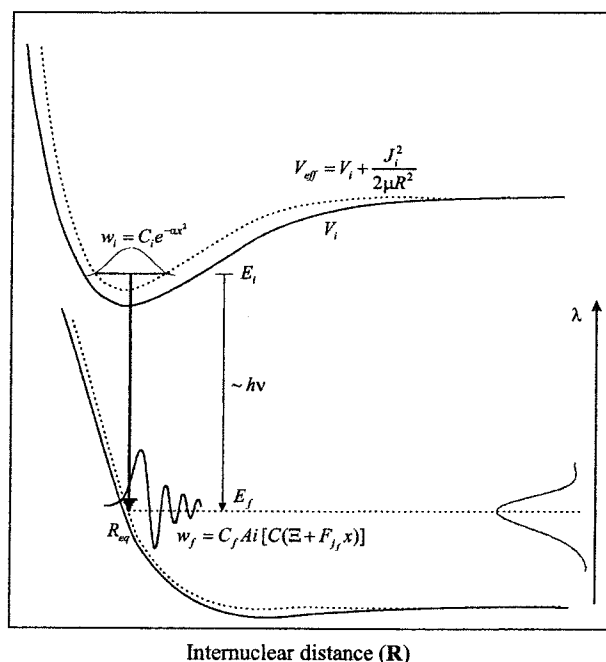
Figure 7.1: The transition diagram for RgX systems under semiclassical approximation

In order to show a more explicit frequency dependence, we expand Eq. (7.34). For a radiative transition (see Fig. 7.1), $E_i - E_f = h\nu$, where for the energy of

the upper state, we use the "impulse approximation" that is the hallmark of the Franck-Condon treatment. This approximation specifies that the electronic transition occurs without a significant change in either the internuclear separation or in the total angular momentum of the system:

$$E_i = V_i(R_{eq}) + \frac{J_i^2}{2\mu R_{eq}^2} + \frac{1}{2}\hbar\omega_e \tag{7.35}$$

$$E_f \approx V_f(R_{eq}) + \frac{J_f^2}{2\mu R_{eq}^2} \tag{7.36}$$

The two sides of Eq. (7.36) are only approximately equal to each other and only in the region of internuclear separation where the magnitude of the upper state wavefunction is significant, corresponding to a high electron density probability. We define Ξ to represent the difference. Referring to Eq. (7.16)

$$\begin{aligned} \Xi &= E_f - \left[V_f(R_{eq}) + \frac{J_f^2}{2\mu R_{eq}^2}\right] \\ &= E_i - V_f(R_{eq}) - \frac{J_f^2}{2\mu R_{eq}^2} - h\nu \end{aligned} \tag{7.37}$$

We can also we define $E_i - V_f(R_{eq}) - J_f^2/2\mu R_{eq}^2 = h\nu_0$, where ν_0 must then be a point representing an energy near the center of the transition. This would correspond to a value of 225.88 nm for the KrI* $B \rightarrow A$ transition. It follows that

$$\Xi = h(\nu_0 - \nu) \tag{7.38}$$

Combining all of the above, and noting that the emission intensity [130] is the

product of (the photon emission rate A)×(the energy per photon $h\nu$)×(the number of atoms in the excited state), we obtain,

$$I_{em} = C_{em}\nu^4 \left\{ Ai[Y_{airy}(\nu)] \, exp[Y_{exp}(\nu)] \right\}^2 \tag{7.39}$$

where

$$C_{em} = \frac{64\pi^4}{3c^3} \left(\frac{\hbar}{\pi\mu\omega_e} \right)^{\frac{1}{2}} [d(R_{eq})C_f]^2$$

$$Y_{airy} = \left(\frac{F_{jf}^2}{2\hbar\mu\omega_e^3} \right)^{\frac{2}{3}} - \left(\frac{2\mu}{\hbar^2 F_{jf}^2} \right)^{\frac{1}{3}} \times [h(\nu_0 - \nu)]$$

$$Y_{exp} = \frac{2}{3} \left(\frac{\hbar C^2 F_{jf}^2}{2\mu\omega_e} \right)^3 - \frac{1}{\hbar\omega_e} \times [h(\nu_0 - \nu)] \tag{7.40}$$

7.2 A Compact Form of the Formula

Further analytical decomposition of Eq. 7.39 shows that it can be expressed in a more compact form:

$$I_{em}(\nu) = C_{em}\nu^4 \left[Ai(\beta^2 + \zeta)exp \left(\frac{2}{3}\beta^3 + \beta\zeta \right) \right]^2 \tag{7.41}$$

where C_{em} is the normalization constant, ζ is proportional to the frequency, and β is a positive constant.

$$\zeta = \frac{h(\nu - \nu_0)}{\eta} \tag{7.42}$$

$$\beta = \frac{\eta}{\hbar\omega_e} = \left(\frac{F_{jf}^2}{2\mu\hbar\omega_e^3}\right)^{\frac{1}{3}} \tag{7.43}$$

$$\eta = \left(\frac{\hbar^2 F_{jf}^2}{2\mu}\right)^{\frac{1}{3}} \tag{7.44}$$
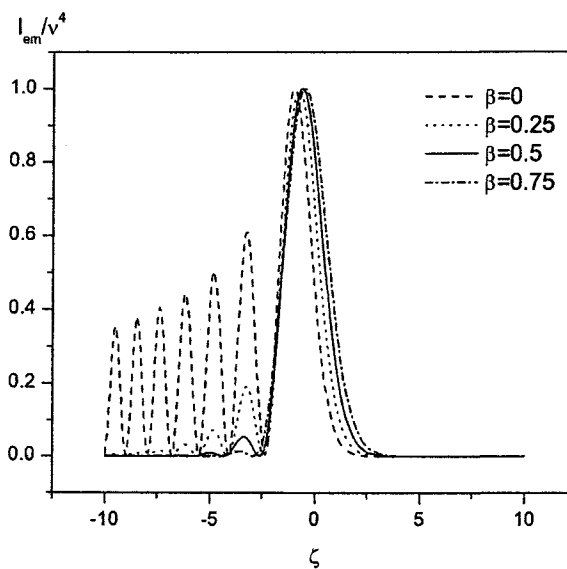
Figure 7.2: The line shape function displays undulatory structure for small β

To investigate the behavior of the line shape expression, we write Eq. 7.41 in the following form,

$$S(\zeta,\beta) = \frac{I_{em}}{C_{em}\nu^4} = \left[Ai(\beta^2 + \zeta)exp\left(\frac{2}{3}\beta^3 + \beta\zeta\right)\right]^2 \tag{7.45}$$
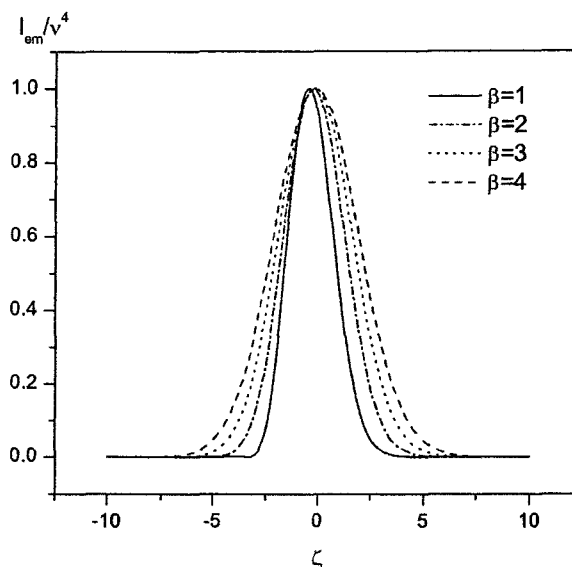
Figure 7.3: The line shape function becomes structureless for large β

We plot the function for different β values in Figs 7.2 and 7.3. For $\beta = 0$, $S(\zeta, \beta)$ is just the square of the Airy function. As β increases, the oscillations at negative ζ are reduced, so that as we reach values $\beta > 1$, they are not visible on this graph.

From the expression in Eq. (7.45), we know that the most important two parameters that determine the line shape are the vibrational frequency of the excited electronic state ω_e, and the magnitude of the force $F_{j_f=0}(=F_0)$, i.e., the magnitude of the slope of the lower state potential curve in the Franck-Condon region. The force contains the centrifugal term, and so depends upon the final angular momentum (J_f) of the dissociating molecule as

$$F_{j_f} = F_0 + \frac{J_f^2}{\mu R_{eq}^3} \tag{7.46}$$

Since the parameters β and η depend upon j_f, the line shape function $I_{em}(\nu)$ in Eq. (7.41) also depends upon j_f, and we re-express it as $I_{em}(\nu, j_f)$. To compare with experiments, we must average over all rotational states to obtain

$$I(\nu) = \frac{1}{Q} \int I_{em}(\nu, j_f) exp[-E(J_f)/kT] \, (2j_f + 1) dj_f \qquad (7.47)$$

with $E(J_f) = J_f^2/2\mu R_{eq}^2$, and $Q = \int exp[-E(J_f)/kT] \, (2j_f+1)dj_f$. In our applications, j_f, and the range of j_f, are large compare to the step size between j values, so that the discrete angular momentum sum can be approximated by an integral.
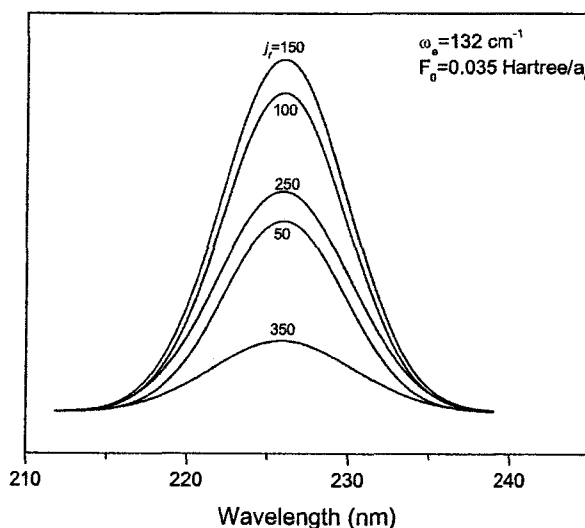
Figure 7.4: Line shapes for different value of angular momentum j_f

In Fig. 7.4, we show the line shapes of several branches in Eq. (7.47) as a function of $\lambda(= c/\nu)$ for various choices of values for j_f. We see that the line shape does not change much as j_f changes, but the magnitude changes greatly. The integrand is

largest for $j_f \approx 150$, one can safely cut off the integral above $j_f \approx 400$ where the magnitude becomes insignificantly small.

7.3 KrI* Spectrum Simulation

There have been no prior systematic studies on the interaction potentials for KrI, so applicable data, such as vibrational constants, B-values, anharmonicity constants, rotational-vibrational coupling, spin-orbit constants, and so on, necessary for discrete simulation of the KrI spectrum are not available. Instead, we tested our analytic model computation against the data taken from the KrI* $B\ ^2\Pi_{1/2} \rightarrow A\ ^2\Pi_{1/2}$ transition in the neighborhood of λ_0=225.88 nm. Our analytical formula, Eq. (7.41), provides a simple approach for studying these unknown systems and estimating at least the first order of these important parameters, which can be used to describe energy levels and transitions in a molecular system.

Physical Quantity	Atomic Unit	Transformation
Energy	Hartree	1 Hartree=4.35974381 $\times 10^{-18}$Joule =627.52 Kcal/mol =27.2116 eV =219474.6 cm^{-1}
Length	a_0	1 $a_0 = 0.529$Å $= 5.29 \times 10^{-11}$meter
Mass	m_e	1 $m_e = 9.10939 \times 10^{-31}$kg
Charge	e_0	1 $e_0 = 1.602188 \times 10^{-19}$Coulombs
Time	t_0	1 $t_0 = 2.4189 \times 10^{-17}$sec

Table 7.1: Atomic units transformation

The computation is performed in atomic units. Table 7.3 lists the transformation

relations between AU and SI units. The parameters used in the formula evaluation are shown in table 7.3.

Parameter	Symbol	Value
Planck's constant	h $\hbar$	$6.6260755 \times 10^{-34}$ J·s= 6.28315 Hartree·t_0 1 Hartree
Speed of light	c	3×10^8 $m/s = 137.17769$ (a_0/t_0)
KrI reduced mass	μ	9.20042×10^4 m_e

Table 7.2: Computational parameters used in KrI* spectrum simulation

By varying the two unknown parameters ω_e and F_0, the analytic expression in Eq. (7.47) is fitted to our experimental data. From this calculation, we estimate $\omega_e = 132$ cm^{-1} and $F_0 = 0.035$ Hartree/a_0. The vibrational constant for B state agrees with Brau's result [12], $\omega_e = 138$ cm^{-1}, from predictions of an alkali-halide model.

Fig. 7.5 shows the experimental and final calculated spectra for KrI* ($\mathbf{B}$ $^2\Pi_{1/2} \rightarrow$ $\mathbf{A}$ $^2\Pi_{1/2}$) transition. Tellinguisen et al. [103] have performed an analytical model calculation for other inert gas halides such as XeI, although their calculation is different in detail from ours. We note that for KrI, we did not observe the undulatory structure that their calculations and experiments found for XeI. We also did not observe such undulations in our experimental data. It is likely that steeper slope of the lower state in the Franck-Condon overlap region suppresses such undulations in KrI. According to the interaction potentials measured by Y. T. Lee et al. [84] from crossed molecular beams experiments, the lower potential curve ($\mathbf{X}$) $^2\Sigma_{1/2}$ slope for XeI at 3.3Å is about 7.1 Kcal/mol Å^{-1} ($\sim$0.006 Hartree/a_0), which is much smaller than the slope for the
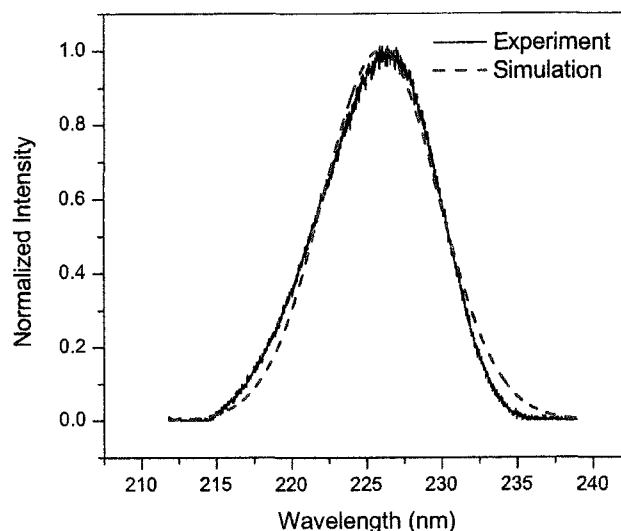
Figure 7.5: Experimental spectrum and simulated semiclassical spectrum for KrI* ($\mathbf{B}$ $^2\Pi_{1/2} \rightarrow \mathbf{A}\ ^2\Pi_{1/2}$) transition when ω_e is 132 cm^{-1} and $F_0 = 0.035$ Hartree/a_0

KrI lower state $\mathbf{A}\ ^2\Pi_{1/2}$ (0.035 Hartree/a_0), at 3.2Å, obtained from our calculation.

In the derivation above, we have assumed that the lowest vibrational state dominates the observed intensity, and we have ignored contributions from higher-level vibrational states. Ewing and Brau [79] calculated that roughly 95% of inert gas halide molecules will be in vibrational states, $v = 0, ..., 4$. That the dominant fraction of our molecules are from $v = 0$ is likely to be a good assumption because of predissociation [91] of KrI at very low v levels and the rapid vibrational relaxation at the high pressure we used in our experiment ($\sim 1 - 2$ atm). The agreement of experimental and simulated spectrum also verifies the sufficiency of this assumption for KrI. Better agreement is expected if we incorporate contributions from higher vibrational levels. In principle, the same technique can be used to evaluate the effects

of higher vibrational levels.
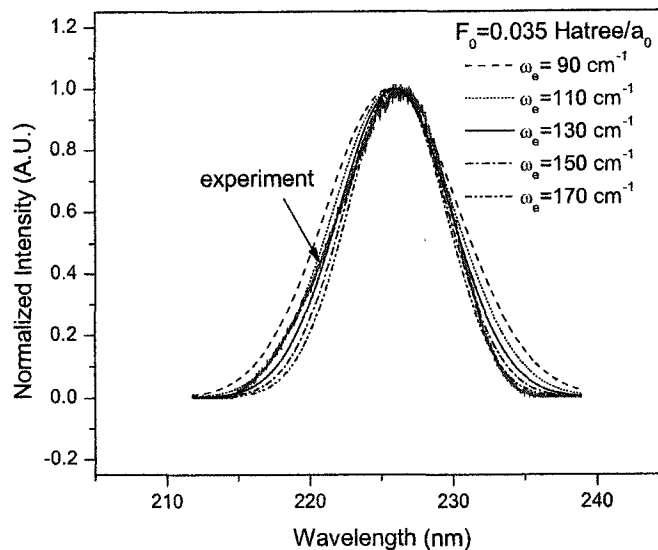
Figure 7.6: Influence of ω_e on the line shape for KrI emissions. The band shape changes slowly with ω_e

Fig. 7.6 displays a sensitivity analysis, showing that the effect of changing vibrational frequency of the upper state: changing ω_e by $\pm 10\%$ has only a minor effect on the line shape. It suggests that the width of the theoretical spectrum increases slightly when the upper state vibration constant ω_e becomes smaller. With a smaller vibration constant, the upper state wavefunction spans a wider region. This results in a wider Frank-Condon overlap region, hence a larger width for the spectrum.

Fig. 7.7 illustrates the very much greater sensitivity associated with changing the slope of the lower state potential curve in the Franck-Condon region. The shape expands when the potential curve becomes steeper. With further experimental and
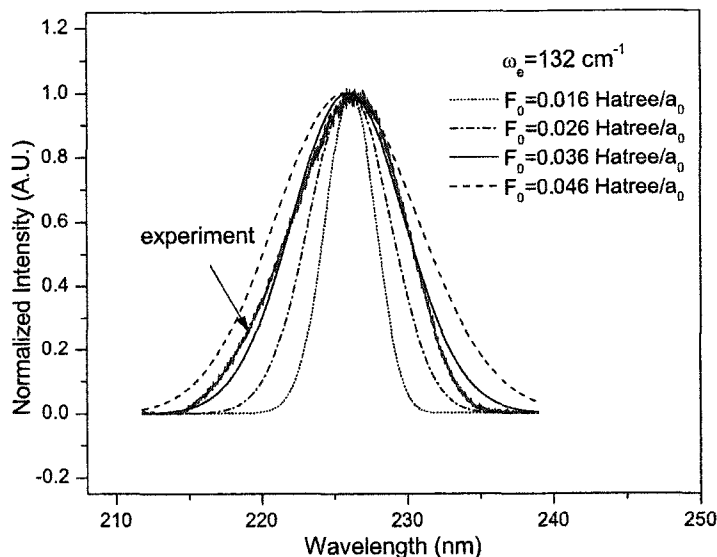
Figure 7.7: Influence of F_0 on the line shape for KrI emissions. The width increases with a steeper potential curve for the lower state

analytical studies, as suggested above, one could, in principle, extract parameters related to the details of the spectrum of photon emission more accurately.

Furthermore, we believe this model is applicable to any two level systems wherein there are transitions between an unbound state and a bound state, yielding convenient analytical expressions for the lineshape. Even if higher order theories to deal with higher vibrational levels yield equations for which an analytic expression does not exist, the resulting integrals can be computed numerically. Thus our calculation provides an easy approach to analyze the detailed molecular curves and constants associated with molecular states of these excimers.

Chapter 8

Summary and Future Work

8.1 Summary

We have demonstrated the production of intense UV light in the RF lamp and microwave lamp with an emphasis on the RF lamp in this dissertation. A more detailed description of the microwave lamp systems can be found in the dissertation work of Dr. Joseph Ametepe [34].

In this work, various discharges, including Xe, KrI, XeI, etc have been investigated in the RF lamp system over the pressure range from 200 torr up to 1500 torr. A detailed kinetic model for the mechanism of formation of rare gas halides has been developed. The neutral gas temperatures have been estimated from the line widths of various emission systems in the spectra.

We also performed 2D and 3D Electromagnetic Particle in Cell (EM-PIC) simulations for both the rf and microwave systems. From these model calculations, we have been able to estimate the most likely EM field distributions in the lamps. The ionization model used in these calculations also provided us with a way to estimate

172

important plasma parameters, such as the electron density n_e, electron temperature T_e, which are exceedingly difficult to measure in such systems, but are nevertheless essential for understanding the physics. The PIC calculations also provide a means to estimate the electron energy distribution function in the rf discharge, necessary to account for features of the observed emission. The calculation suggests the presence of hot electrons, capable of exciting the high-lying ion and neutral states that are necessary to produce VUV emissions.

Besides performing the PIC simulations, we also performed a high level *ab initio* quantum mechanical calculation, using a code known as Gaussian, to construct the ground state and excited-state interaction potential curves of KrI. The resulting emissions, which can be predicted from these curves, agree well with experiments. This *ab initio* work also provides other interesting results including pictorial representations of the molecular orbitals, electron distribution and electrostatic potential.

Prior to this work, there have not been successful systematic theoretical efforts to elucidate the light emission mechanism of KrI. Our work provides a new semiclassical model for studying important molecular parameters governing such light emission. We derived an analytic expression for the line shape of excimer emissions which will be generally useful for modeling other such species. Furthermore, the resulting model can be used to fit the analytical equation to experimental data in order to find reasonable estimates for molecular parameters needed in other physical calculations.

8.2 Future Work

8.2.1 Plasma Diagnostic

In this work, we demonstrated computational methods to obtain estimates of plasma temperature and density using PIC codes. The results from this work helped us in our design and point the way for others to determine the optimal geometry and operating parameters for such high pressure designs to maximize uv output and to tune the lamps for selected areas of wavelength where these lamps will be needed.

We assessed the suitability of microwave interferometry to obtain the line-integrated electron density of the plasma. Although this non-intrusive method would have been highly desirable, we determined that is is not applicable for our rf lamp. As we described in chapter 4, these high pressure discharges are composed of several thin, rapidly moving, random filaments. Microwave interferometry determines the average electron density from the phase shift caused as a well-collimated beam of electromagnetic radiation transits a plasma [134]. In our lamps, the random filaments are of very narrow diameter, and move much too fast and randomly for this method to provide a reasonable spatial result for the electron density distribution.

Future experiments may be able to take advantage of various spectroscopic techniques, that are more suitable for assessing average properties of such high pressure discharges. Analysis of the spectra, using calibrated measurement of absolute line-intensity measurements can permit one to obtain information on plasma parameters such as the temperature and density. The electron temperatures can be

determined by the relative intensity ratio of discharge species decaying to the same final state [135, 136]. Additional information on the behavior of the discharge in the sheath region can be obtained by measuring ion kinetic temperature, or even the velocity distribution, via Doppler broadening. Detailed experimental study of the emission spectra over a wide range of wavelength, coupled to modeling and other plasma measurements, can yield information on the electron energy distribution function which can be compared to the EEDF obtained in our PIC simulations.

8.2.2   Biology Applications

We foresee experiments to test the applications of our rf lamps for vaious technical purposes. One of these would be to disinfect surfaces. Another would be to purify water by eliminating microbial agents. To point the way for such follow-on experimental proposals, we did some preliminary UV exposure experiments on Escherichia coli (E. coli) cultures, that were prepared by our co-workers in the biology department of Hollins University in Roanoke Virginia. These agar-plate cultures were irradiated using rf lamps, operating at around 1 kW, with a fill producing a XeI* discharge.

This lamp is dominated by emission around 253 nm. Irradiation times ranged from 5 to 60 seconds and at irradiation distances of 5 cm to 20 cm from bulb surface. We limited the exposure to distances greater than 5 cm to minimize substrate heating which could confuse the experiment with thermal damage to the organisms. Fig. 8.1 shows photos of the irradiated and unirradiated cultures of the Escherichia coli. At all

distances we tried, from 5 to 20 cm, more than 99.9% of the bacteria were inactivated.

At 5 cm from bulb surface, using these relatively low colony counts, we obtained an

apparent 100% inactivation within 5 seconds. At 20 cm, we found that the same

intensity required 30 seconds of exposure to yield 99.9% inactivation. These high

percentages of inactivation are not entirely unexpected since the XeI* lamp has more

than 90% of its UV emission within 5 nm of 253 nm, which gives it a very large overlap

with the known primary uv absorption band of DNA. Although these results are quite

preliminary, and a great deal more systematic investigation will be required to test

the efficacy of this style of lamp against not only E. Coli, but other major pathogens

of interest in the areas of food service, clinical practice, defense, or counter-terrorism

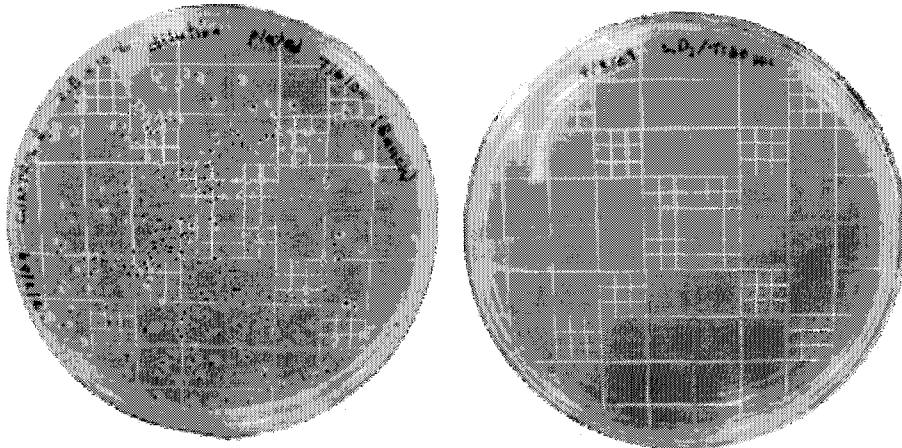uses, our preliminary work indicates that such studies are likely to yield excellent

results.

Figure 8.1: Photos of unirradiated (left) and irradiated (right) cultures of Escherichia coli. Irradiations were done at distances of 5 cm to 20 cm from bulb surface. In all cases we obtained over 99.9% inactivation corresponding to disinfection coefficient of 4.3

One of the main advantages of our lamp system for such studies is that it provides an easy means to determine the antibacterial efficacy of different wavelengths of uv light to vitiate various bacteria. Our lamp also provide the potential for very easy variation of intensity and can be "seeded" with species to yield very different spectral distributions of emitters to allow studies of synergies between multiple wavelengths at various intensities.

8.2.3   Spectral Model

The semiclassical model for bound to continuum electronic transitions only includes transitions from the lowest vibrational level of the **B** state. It accounts for our measured spectra probably because of the predissociation of KrI. For other RgX systems where transitions from higher vibrational levels cannot be ignored, we propose further studies to evaluate the Franck-Condon integral between the higher vibrational state of a harmonic oscillator and the unbound lower state analytically or numerically.

A more detailed spectroscopic study is also proposed to obtain $B-$ and $A-$state potentials of KrI. For this purpose, a spectrum with the resolution high enough to resolve individual vibrational transitions is needed to obtain accurate Franck-Condon factors. The potential energy curves can be modeled by a Morse-RKR function for the A state and a Rittner function for the B state. Trial-and error Franck-Condon calculations that are used by Tellinghuisen [104] could be applied for KrI to locate the B and A state potential curves.

Accurate state potentials are valuable for explaining various phenomena in spectra and plasma, such as predissociation, energy transfer and reaction path. All these are important in building ultra-intense light sources that will find considerable applications in many areas.

Appendix A

Franck-Condon Principle

Classically, the Franck-Condon principle is the approximation that an electronic transition is most likely to occur without changes in the positions of the nuclei in the molecular entity and its environment. The resulting state is called a Franck-Condon state, and the transition involved, a vertical transition.

The quantum mechanical formulation of this principle is that the intensity of a vibronic transition is proportional to the square of the overlap integral between the vibrational wavefunctions of the two states that are involved in the transition. The Condon approximation is based on the assumptions that the electronic transition occurs on a time scale short compared to nuclear motion so that the transition probability can be calculated at a fixed nuclear.

Note that this is a more restrictive approximation than the Born-Oppenheimer approximation (BOA), which states that the motion of electrons can be considered decoupled from the motion of the nuclei and each form of motion can be treated separately. BOA is based on the fact that the mass of the atomic nuclei is far greater than the mass of the electrons orbiting it, and it does not demand that the nuclear

179

coordinate be a fixed value.

Then, the wavefunctions of the initial and final states are the products of the respective electronic and vibrational wavefunctions. The intensity of a vibrational band in an electronically allowed transition is proportional to the absolute square of the overlap integral of the vibrational wavefunctions of the initial and final states. It indicates only that transitions are favored when there is a large overlap between the vibrational wavefunctions of the initial and final states of the transition.

Given the Franck-Condon principle, we can write the transition probability as a product of an electronic term and a nuclear term.

$$B = |\mu_{ge}|^2 FCF \tag{A.1}$$

where FCF refers to the Franck-Condon factor which is the nuclear term. The FCF can be expressed as the square of nuclear overlap terms.

$$FCF = \sum_{\nu'}^{\infty} \sum_{\nu''}^{\infty} S_{\nu',\nu''}^2 \tag{A.2}$$

We must sum over all vibrational states of the lower state and the upper state in order to calculate the FCF. In reality only a finite number of states have significant overlap and can contribute to the line shape.

Appendix B

Hund's Coupling Cases

Quantum numbers of molecular terms of dimers depend on the rules of summing the electronic momenta into the total molecular momentum $\mathbf{J}$. These rules are determined by three kinds of interactions in a molecule: V_e, the interaction potential between the orbital angular momentum and molecular axis, V_m, the interaction potential between electrons and rotational motion of the molecular. Depending on possible relationships between the above interaction potentials, one can define different types of so-called Hund's coupling cases. For each case, there is a set of quantum numbers to describe the coupling scheme. The figures below are adapted from Herzberg [127]. Further details about each case are discussed in Ref. [127].

Hund's case (a)

In Hund's case (a), the electronic motion (spin as well as orbital) is strongly coupled to the molecular axis, so only the projections Λ of the total orbital angular momentum $\mathbf{L}$ and Σ of the total spin angular momentum $\mathbf{S}$ are significant. It is assumed that the interaction of the nuclear rotation $\mathbf{N}$ with the electronic motion $\mathbf{L}, \mathbf{S}$ is very weak. Therefore, the limit $V_e \gg V_m$ corresponds to the Hund's case (a).
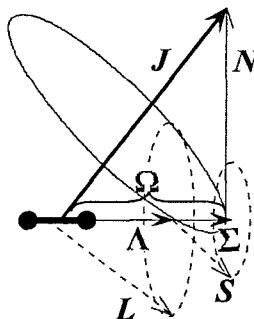
Figure B.1: Diagram of Hund's case (a): the electronic motions couple to the internuclear axis to form Ω, then the angular momentum of the nuclear rotation $\mathbf{N}$ and Ω form total angular momentum $\mathbf{J}$

The sum of $\mathbf{L}$ and $\mathbf{S}$, which is the electronic angular momentum Ω, is well defined.

Ω and $\mathbf{N}$ form the resultant total molecular angular momentum $\mathbf{J}$. Figure B.1 gives

the vector diagram for this case. The vector $\mathbf{J}$ is constant in both magnitude and

direction. Ω and $\mathbf{N}$ rotate about this vector, as is called nutation. The precession of

$\mathbf{L}$ and $\mathbf{S}$ is about the internuclear axis. In this case, the precession motion is assumed

to be very much faster than the nutation motion.

Hund's case (b)

When $\Lambda = 0$, and $\mathbf{S} \neq 0$, the spin vector $\mathbf{S}$ is not coupled to the internuclear axis

at all. In this case Ω is not defined. Sometimes, particularly for light molecules, even

if $\Lambda \neq 0$, $\mathbf{S}$ may be only weakly coupled to the internuclear axis. The above weak (or

zero) coupling of spin angular momentum to the internuclear axis is the characteristic

of Hun's case (b). In this case, Λ and $\mathbf{N}$ form a resultant momentum designated as

$\mathbf{K}$ here. And the total molecular angular momentum $\mathbf{J}$ is formed by $\mathbf{K}$ and $\mathbf{S}$ (see
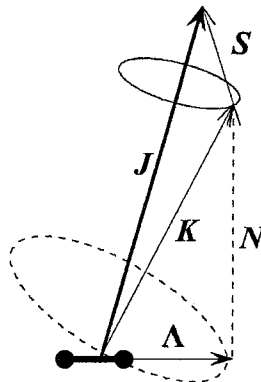
Figure B.2: Diagram of Hund's case (b): Spin vector **S** is weakly (or not) coupled to the internuclear axis. **K** is the total angular momentum apart from spin

Fig. B.2). The nutation of the figure axis, represented by the broken line ellipse, is much faster than the precessions of **K** and **S** about **J**, represented by the solid line ellipse.

Hund's case (c)

In certain cases, particularly for heavy molecules, the interaction between **L** and **S** is stronger than the interaction with the internuclear axis. In this case, Λ and Σ are not defined, but **L** and **S** form a resultant $\mathbf{J_a}$ and the projection of $\mathbf{J_a}$ on the internuclear axis Ω is still a good quantum number. The electronic angular momentum Ω and the angular momentum **N** of nuclear rotation then form the resultant angular momentum **J**. Figure B.3 gives the vector diagram for Hund's case (c).

Hund's case (d)

In Hund's case (d), the coupling between **L** and the internuclear axis is very weak while that between **L** and the axis of rotation is strong. The angular momentum
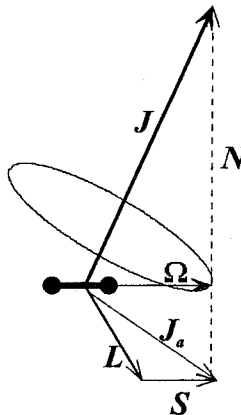
Figure B.3: Diagram of Hund's case (c): The **LS** coupling forms $\mathbf{J_a}$, the projection of which Ω is well defined
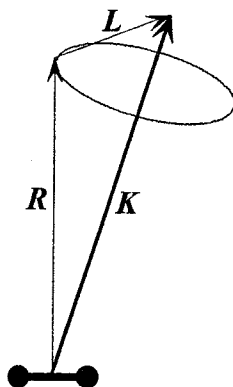
Figure B.4: Diagram of Hund's case (d): **L** is strongly coupled to the rotation axis. The addition of **K** and **S** to form **J** is not shown, since it is of no practical importance

of nuclear rotation which is called **R** here (rather than **N**) is quantized and has

magnitude $\sqrt{R(R+1)}\hbar$. The angular momenta **R** and **L** give the total angular

momentum apart from spin, which is designated by **K** as before (Figure B.4). The

angular momenta **K** and **S** form the total angular momentum **J**. In case (d) the

coupling between **K** and **S** is so small that **S** and therefore also **J** can be disregarded

and we only use **K**.

Hund's case (e)

This case is similar with case (d) except that **L** and **S** are strongly coupled at this

time. As in case (c) **L** and **S** first form a resultant **J**$_\mathbf{a}$, which is then combined with

R to form **J**.

Figure B.5: Diagram of Hund's case (e): **L** and **S** are strongly coupled to form **J**$_\mathbf{a}$, which
is combined with the angular momentum of nuclear rotation **R** to form the resultant **J**. No
practical examples of case (e) have been observed

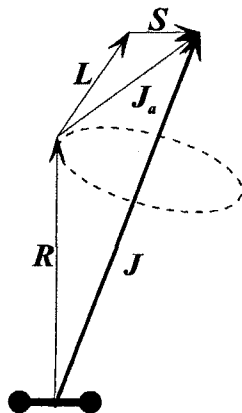# Appendix C

Intensity Calibration

In order to determine the absolute values of the excimer radiation from our lamps, accurate intensity calibration must be performed after each spectrum scan. One calibration method to compare the discharge emission with that of a calibrated broad-band UV source. In our experiments, the calibration was performed with a deuterium lamp (Oriel BJ2775) with a calibrated spectrum, traceable to NIST primary standards, from 160 nm to 400 nm.

Spectral radiance of a standard source is usually calibrated only for a rather limited portion of the source, where its output is nearly homogeneous. The standard spectral irradiance data, P_D, was measured at a distance of 50 cm, which allows us to approximate our standard lamp as a point source. The relative intensity values R_D of the D_2 lamp were measured in our system. The standard source was separated with the spectrometer by a 50 cm long and 0.8 mm ID suprasil tube purged by nitrogen. The relation between P_D and R_D for emission at a wavelength, λ, is as follows:

$$R_D(\lambda) = K(\lambda)P_D(\lambda) \tag{C.1}$$

186

where the factor $K(\lambda)$ represents the effect of transmission rate for the whole light path, including effects of purging, mirror transmission and reflection, and scintillator conversion efficiency. In our range of interest (160 nm - 200 nm), the transmission of the spectrometer varies by only a few percent. The scintillator response is also almost flat over this spectral range [40], so it is a good assumption that K does not depend on the wavelength.

$$R_D(\lambda) = K P_D(\lambda) \qquad (C.2)$$

We approximate our 50 cm $\times$ 0.8 mm i.d. suprasil tube as a series of point sources along the centerline of the bulb. Our experiments at different position along the length of the bulb show that in the section near the tuner, where hot electrons are present, the variation of excimer emission intensities is negligible. Our light collection system for the lamp bulb was the same as that used for the D_2 lamp. We found that maintaining the light path at a pressure of 10^{-3} torr gave the same results as carefully purging the path with ultra-dry nitrogen. We can thus allow that the absolute value $P_E(\lambda)$ and the relative values $R_E(\lambda)$ are related by the same factor K.

$$R_E(\lambda) = K P_E(\lambda) \qquad (C.3)$$

Combining Eq. (C.2) and Eq. (C.3) yields the absolute values of the excimer radiation at a distance R=50 cm.

$$P_E(\lambda) = \frac{P_D}{R_D} R_E(\lambda) \qquad (C.4)$$

We assume that for each point source along the lamp centerline the emission is isotropic, so that the radiation H_E at a distance r is given by

$$H_E(\lambda) = \frac{R^2}{r^2}\frac{P_D}{R_D}R_E(\lambda)$$ (C.5)

Then the total radiant power P_T of the excimer discharge is obtained by integrating over the excimer line profile and the inner area of the bulb to yield:

$$P_T = \int \int_{\lambda_1}^{\lambda_2} H_E(\lambda)d\lambda ds$$ (C.6)

where λ_1 and λ_2 are the lower and upper bounds of the excimer emission. For cylindrical lamps, the details of how to specify solid angle, decomposition of spatial distribution of radiance, and integration to find the total radiated power can be found in the Ph.D dissertation of J. Ametepe [34]

Bibliography

[1] Mary Bellis. "Lightbulbs, Lighting and Lamps". Inventors at About. Retrieved June 1, 2004 from http://inventors.about.com/library/inventors/bllight.htm.

[2] Mary Bellis. "Humphry Davy". Inventors at About. Retrieved June 1, 2004 from http://inventors.about.com/library/inventors/blHumphryDavy.htm.

[3] M. F. Gendre. "Two Centuries of Electric Light Source Innovations". Retrieved June 4, 2004 from http://www.einlightred.tue.nl/lightsources/history /light_history.pdf.

[4] "Diagram and Explanation Of An Incandescent Bulb". Retrieved June 1, 2004 from http://www.bulbs.com/lightingguide/tech_incandescentdiagram.asp.

[5] Philips Lighting B.V. "Philips QL lamp systems". Retrieved June 2, 2004 from http://www.lighting.philips.com/feature/ql/pdf/ql_oem_guide.pdf.

[6] A. L. Schawlow and C. H. Townes. *Physical Review*, 12(6):1940, 1958.

[7] G. E. Moore. *Electronics*, 38(8), 1965.

[8] C. D. Geddes, I. Gryczynski, J. Malicka, Z. Gryczynski, and J. R. Lakowicz. Fluorescence detection gains in sensitivity. *Photonics Spectra*, 38(2):92, 2004.

[9] S. Hartel, S. Tykhonova, M. Haas, and H. Diehl. *Journal of Fluorescence*, 12(3-4):465–479, 2002.

[10] C. A. Brau and J. J. Ewing. *Applied Physics Letters*, 27(8):435, 1975.

[11] W. E. Ernst and F. K. Tittel. *Journal of Applied Physics*, 51(5):2432, 1980.

[12] C. A. Brau and J. J. Ewing. *Journal of Chemical Physics*, 63(11):4640, 1975.

[13] R. Cooper, L. S. Denison, P. Zeglinski, C. R. Roy, and H. Gillis. *Journal of Applied Physics*, 54(6):3053, 1983.

[14] K. Tamagake, D. W. Setser, and J. H. Kolts. *Journal of Chemical Physics*, 74(8):4286, 1981.

[15] J. Tellinghuisen and M. R. Mckeever. *Chemical Physics Letter*, 72(1):94, 1980.

[16] J. E. Velazco and D. W. Setser. *Journal of Chemical Physics*, 62(5):1990, 1975.

[17] M. P. Casassa, M. F. Golde, and A. Kvaran. *Chemical Physics Letter*, 59(1):51, 1978.

[18] J. Y. Zhang and I. W. Boyd. *Journal of Applied Physics*, 80(2):633, 1996.

[19] M. T. Jones, T. D. Dreiling, D. W. Setser, and R. N. McDonald. *Journal of Physical Chemistry*, 89(21):4501, 1985.

[20] Y. Zhao, I. Yourshaw, G. Reiser, C. C. Arnold, and D. M. Neumark. *Journal of Chemical Physics*, 101(8):6538, 1994.

[21] L. Tonks and I. Langmuir. *Physical Review*, 34:876, 1929.

[22] H. V. Boenig. *Plasma Science and Technology*. Cornell University Press Ltd., Ithaca and London, 1982.

[23] A. Von Engel. *Ionized Gases*. Clarendon Press, Oxford, 1965.

[24] M. A. Lieberman and A. J. Lichtenberg. *Principles of Plasma Discharges and Materials Processing*. John Wiley & Sons, Inc., New York, NY, 1994.

[25] B. M. Smirnov and H. R. Reiss. *Physics of Ionized Gases*. John Wiley & Sons, Inc., New York, 2001.

[26] R. C. Davidson. *An Introduction to the physics of nonneutral plasmas*. Addison-Wesley, Redwood City, CA, 1990.

[27] J. Gong. *Journal of Plasma Physics*, 62(1):87–94, 1999.

[28] S. Liu, Y. Yan, J. Mao, and D. M. Manos. *Physical Review E*, 65:036411, 2002.

[29] H. K. Malik. *Journal of Plasma Physics*, 69(1):59–67, 2003.

[30] L. Stafford, J. Margot, and T. W. Johnston. *Journal of Plasma Physics*, 66(5):349–362, 2001.

[31] A. D. MacDonald. *Microwave Breakdown in Gases*. Wiley, New York, 1966.

[32] G. Cohen. Status of uv/eb in north america. Charlotte, NC, May 2004. RadTech.

[33] B. Gellert and U. Kogelschatz. *Applied Physics B: Lasers and Optics*, 52:14, 1991.

[34] J. D. Ametepe. *Studies in Microwave and RF Capacitively Coupled Excimer Lamp*. PhD thesis, College of William and Mary, 1999.

[35] H. Hosono, K. Kajihara, T. Suzuki, Y. Ikuta, L. Skuja, and M. Hirano. *Solid State Communications*, 122:117–120, 2002.

[36] H. Bach and N. Neuroth. *The Properties of Optical Glass*. Springer-Verlag Berlin Heidelberg, New York, 1995.

[37] K. Kajihara, Y. Lkuta, M. Hirano, T. Ichimura, and H. Hosono. *Journal of Chemical Physics*, 115(20):9473, 2001.

[38] C. M. Smith and L. A. Moore. *Journal of Fluorine Chemistry*, 122:81–86, 2003.

[39] R. Payling, D. G. Jones, and A. Bengtson. *Glow Discharge Optical Emission Spectrometry*. JOHN WILEY & SONS, New York, 1997.

[40] N. Kristianpoller and R. A. Knapp. *Applied Optics*, 3(8):915, 1964.

[41] R. Seedorf, H. J. Eichler, and H. Koch. *Applied Optics*, 24(9):1985, 1985.

[42] C. M. VAN ATTA. *Vacuum Science and Engineering*. McGRAW-HILL, New York, 1965.

[43] R. D. Saunders, W. R. Ott, and J. M. Bridges. *Applied Optics*, 17(4):593, 1978.

[44] U. Finkenzeller and D. Labs. *Applied Optics*, 18(23):3938, 1979.

[45] W. R. Ott, K. Behringer, and G. Geires. *Applied Optics*, 14(9):2121, 1975.

[46] J. A. Barker, R. O. Watts, J. K. Lee, T. P. Schafer, and Y. T. Lee. *Journal of Chemical Physics*, 61(8):3081, 1974.

[47] O. Vallee, N. T. Minh, and J. Chapelle. *Journal of Chemical Physics*, 73(6):2784, 1980.

[48] P. Duplaa and F. Spiegelmann. *Journal of Chemical Physics*, 105(4):1500, 1996.

[49] Edward C.M. Chen and Edward S. Chen. *Chemical Physics Letter*, 293:491, 1998.

[50] R. S. Mulliken. *Journal of Chemical Physics*, 52(10):5170, 1970.

[51] C. E. Moore. *Atomic Energy Levels*, volume 27. U.S. Department of Commerce, National Bureau of Standards, Washington, D.C., 1971.

[52] F. Brandi, I. Velchev, W. Hogervorst, and W. Ubachs. *Physical Review A*, 64:032505, 2001.

[53] I. Messing, D. J. Eckstrom, and D. C. Lorents. *Journal of Chemical Physics*, 93(1):34, 1990.

[54] P. Dube, M. J. Kiik, and B. P. Stoicheff. *Journal of Chemical Physics*, 103(18):7708, 1995.

[55] Ch. K. Rhodes. *Excimer Lasers*. Springer-Verlag Berlin Heidelberg, New York, 1979.

[56] K. Wojciechowski and M. Forys. *Radiation Physics and Chemistry*, 54(1):1, 1999.

[57] P. G. Wilkinson and Y. Tanaka. *Journal of the Optical Society of America*, 45(5):344, 1954.

[58] L. T. Specht, S. A. Lawton, and T. A. DeTemple. *Journal of Applied Physics*, 51(1):166, 1980.

[59] W. F. Liu and D. C. Conway. *Journal of Chemical Physics*, 62(8):3070, 1975.

[60] T. D. Bonifield, F. H. K. Rambow, G. K. Walters, M. V. McCusker, D. C. Lorents, and R. A. Gutcheck. *Journal of Chemical Physics*, 72(5):2914, 1980.

[61] H. A. Koehler, L. S. Ferderber, D. L. Redhead, and P. J. Ebert. *Applied Physics Letters*, 21(5):198, 1972.

[62] S. C. Wallace, R. T. Hodgson, and R. W. Dreyfus. *Applied Physics Letters*, 23(1):22, 1973.

[63] A. W. Johnson and J. B. Gerardo. *Journal of Chemical Physics*, 59(4):1738, 1973.

[64] P. Millet, A. Birot, H. Brunet, J. Galy, B. Pons-Germain, and J. L. Teyssier. *Journal of Chemical Physics*, 69(1):92, 1978.

[65] J. W. Keto, R. E. Gleason Jr., T. D. Bonifield, G. K. Walters, and F. K. Soley. *Chemical Physics Letter*, 42(1):125, 1976.

[66] O. Dutuit, M. C. Castex, J. L. Calve, and M. Lavollee. *Journal of Chemical Physics*, 73(7):3107, 1980.

[67] A. El-Habachi and K. H. Schoenbach. *Applied Physics Letters*, 73(7):885, 1998.

[68] J. D. Ametepe, J. Diggs, and D. M. Manos. *Journal of Applied Physics*, 85(11):7505, 1999.

[69] R. E. Gleason, T. D. Bonifield, J. W. Keto, and G. K. Walters. *Journal of Chemical Physics*, 66(4):1589, 1977.

[70] O. Cheshnovsky, B. Raz, and J. Jortner. *Chemical Physics Letter*, 15(4):475, 1972.

[71] K. Tamagake and D. W. Setser. *Journal of Chemical Physics*, 67(10):4370, 1977.

[72] P. C. Tellinghuisen, J. Tellinghuisen, J. A. Coxon, J. E. Velazco, and D. W. Setser. *Journal of Chemical Physics*, 68(11):5187, 1978.

[73] P. J. Hay and T. H. Dunning Jr. *Journal of Chemical Physics*, 66(3):1306, 1977.

[74] J. Tellinghuisen, G. C. Tisone, J. M. Hoffman, and A. K. Hays. *Journal of Chemical Physics*, 64(11):4796, 1976.

[75] Jr. T. H. Dunning and P. J. Hay. *Applied Physics Letters*, 28(11):649, 1976.

[76] M. Krauss. *Journal of Chemical Physics*, 67(4):1712, 1977.

[77] M. F. Golde and B. A. Thrush. *Chemical Physics Letter*, 29:486, 1974.

[78] C. A. Brau and J. J. Ewing. *Journal of Chemical Physics*, 63:4640, 1974.

[79] J. J. Ewing and C. A. Brau. *Physical Review A*, 12(1):129, 1975.

[80] J. E. Velazco, J. H. Kolts, and D. W. Setser. *Journal of Chemical Physics*, 65(9):3468, 1976.

[81] P. J. Hay and T. H. Dunning Jr. *Journal of Chemical Physics*, 69(5):2209, 1978.

[82] I. W. Boyd and J. Y. Zhang. *Nuclear Instruments and Methods in Physics Research B*, 121:349, 1997.

[83] M. F. Golde and A. Kvaran. *Journal of Chemical Physics*, 72(1):434, 1980.

[84] P. Casavecchia, G. He, R. K. Sparks, and Y. T. Lee. *Journal of Chemical Physics*, 77(4):1878, 1982.

[85] M. G. Golde and R. A. Poletti. *Chemical Physics Letter*, 80(1):23, 1981.

[86] J. Y. Zhang and I. W. Boyd. *Applied Physics B: Lasers and Optics*, 71:177, 2000.

[87] J. Tellinghuisen and L. F. Phillips. *Journal of Physical Chemistry*, 90(21):5108, 1986.

[88] V. V. Datsyuk. *Journal of Chemical Physics*, 102(2):799, 1994.

[89] R. Turner. *Physical Review*, 140(2A):A426, 1965.

[90] R. T. Ku, J. T. Verdeyen, B. E. Cherrington, and J. G. Eden. *Physical Review A*, 8(6):3123, 1973.

[91] D. Zhong, D. W. Setser, R. Sobczynski, and W. Gadomskj. *Journal of Chemical Physics*, 105(12):5020, 1996.

[92] G. P. Quigley and W. M. Hughes. *Applied Physics Letters*, 32(10):649, 1978.

[93] T. Oka, K. V. S. Rama Rao, J. L. Redpath, and R. F. Firestone. *Journal of Chemical Physics*, 61(11):4740, 1974.

[94] L. G. Williams and D. R. Crosley. *Physical Review A*, 9(2):622, 1974.

[95] K. L. Randall and D. J. Donaldson. *Chemical Physics*, 211:377, 1996.

[96] P. K. Leichner and R. J. Ericson. *Physical Review A*, 9(1):251, 1974.

[97] J. D. Cook and P. K. Leichner. *Physical Review A*, 31(1):90, 1985.

[98] Y. Salamero, A. Birot, H. Brunet, J. Galy, P. Millet, and J. P. Montagne. *J. Phys. B: Atom. Molec. Phys.*, 12(3):1979, 1979.

[99] R. Turner. *Physical Review*, 158(1):121, 1967.

[100] J. E. Velazco, J. H. Kolts, and D. W. Setser. *Journal of Chemical Physics*, 69(10):4357, 1978.

[101] A. Hiraya, K. Shobatake, R. J. Donovan, and A. Hopkirk. *Journal of Chemical Physics*, 88(1):52, 1988.

[102] R. J. Donovan, B. V. O'Grady, K. Shobatake, and A. Hiraya. *Chemical Physics Letter*, 122(6):612, 1985.

[103] J. Tellinghuisen, A. K. Hays, J. M. Hoffman, and G. C. Tisone. *Journal of Chemical Physics*, 65(11):4473, 1976.

[104] D. T. Radzykewycz and J. Tellinghuisen. *Journal of Chemical Physics*, 105(4):1330, 1996.

[105] B. V. O'Grady and R. J. Donovan. *Chemical Physics Letter*, 122(5):503, 1985.

[106] F. L. Gates. *Journal of General Physiology*, 14:31, 1930.

[107] G. D. Smith. *Numerical Solution of Partial Differential Equations: Finite Difference Method.* Clarendon Press, Oxford, UK, 3 edition, 1985.

[108] K. S. Kunz and R. Luebbers. *The Finite Difference Time Domain Method for Electromagnetics.* CRC Press, Boca Raton, FL, USA, 1993.

[109] A. Taflove. *Computational Electrodynamics: The Finite-Difference Time-Domain Method.* Artech House, Boston, MA, USA, 1995.

[110] A. Taflove and S. Hagness. *Computational Electrodynamics: The Finite-Difference Time-Domain Method.* Artech House, Boston, MA, USA, 2 edition, 2000.

[111] U. van Rienen. *Numerical Methods in Computational Electrodynamics.* Springer Verlag, Berlin, 2001.

[112] E. Gjonaj, T. Lau, and T. Weiland. Conformal modeling of space-charge-limited emission from curved boundaries in particle simulation. In *Proceedings of the 2003 Particle Accelerator Conference*, 2003.

[113] B. Mobus, M. Richter, and G. Ulm. *Physical Review A*, 61:022723, 2000.

[114] D. A. Erwin and J. A. Kunc. *Physical Review A*, 70:022705, 2004.

[115] T. Nedelea and H. M. Urbassek. *Physics of Plasmas*, 9(8):3209, 2002.

[116] A. R. Barakat and R. W. Schunk. *J. Phys. D: Appl. Phys.*, 14(3):421, 1981.

[117] E. Neyts, M. Yan, A. Bogaerts, and R. Gijbels. *Journal of Applied Physics*, 93(9):5025, 2003.

[118] M. J. Frisch, G. W. Trucks, H. B. Schlegel, G. E. Scuseria, M. A. Robb, J. R. Cheeseman, J. A. Montgomery, Jr., T. Vreven, K. N. Kudin, J. C. Burant, J. M. Millam, S. S. Iyengar, J. Tomasi, V. Barone, B. Mennucci, M. Cossi, G. Scalmani, N. Rega, G. A. Petersson, H. Nakatsuji, M. Hada, M. Ehara, K. Toyota, R. Fukuda, J. Hasegawa, M. Ishida, T. Nakajima, Y. Honda, O. Kitao, H. Nakai, M. Klene, X. Li, J. E. Knox, H. P. Hratchian, J. B. Cross, V. Bakken, C. Adamo, J. Jaramillo, R. Gomperts, R. E. Stratmann, O. Yazyev, A. J. Austin, R. Cammi, C. Pomelli, J. W. Ochterski, P. Y. Ayala, K. Morokuma, G. A. Voth, P. Salvador, J. J. Dannenberg, V. G. Zakrzewski, S. Dapprich, A. D. Daniels, M. C. Strain, O. Farkas, D. K. Malick, A. D. Rabuck, K. Raghavachari, J. B. Foresman, J. V. Ortiz, Q. Cui, A. G. Baboul, S. Clifford, J. Cioslowski, B. B. Stefanov, G. Liu, A. Liashenko, P. Piskorz, I. Komaromi, R. L. Martin, D. J. Fox, T. Keith, M. A. Al-Laham, C. Y. Peng, A. Nanayakkara, M. Challacombe, P. M. W. Gill, B. Johnson, W. Chen, M. W. Wong, C. Gonzalez, and J. A. Pople. Gaussian 03, Revision C.02. Gaussian, Inc., Wallingford, CT, 2004.

[119] C. Møller and M. S. Plesset. *Physical Review*, 46:618, 1934.

[120] S. Grimme. *Journal of Chemical Physics*, 118(20):9095, 2003.

[121] J. Olsen, O. Christiansen, H. Koch, and P. Jørgensen. *Journal of Chemical Physics*, 105(12):5082, 1996.

[122] J. Cizek. *Journal of Chemical Physics*, 45(11):4256, 1966.

[123] A. Becke. *Journal of Chemical Physics*, 98(7):5648, 1993.

[124] C. E. Check, T. O. Faust, J. M. Bailey, B. J. Wright, T. M. Gilbert, and L. S. Sunderlin. *Journal of Physical Chemistry*, 105(34):8111, 2001.

[125] A. K. Wilson, D. E. Woon, and K. A. Peterson. *Journal of Chemical Physics*, 110(16):7667, 1999.

[126] W. J. Herhre, L. Radom, P. v.R. Schleyer, and J. A. Pople. *AB Initio Molecular Orbital Theory*. John Wiley & Sons, New York, 1986.

[127] G. Herzberg. *Molecular Spectra and Molecular Structure*. Van Nostrand Reinhold Company Limited, New York, 1950.

[128] M. S. Child. *Semiclassical Mechanics With Molecular Applications*. Oxford University Press, Oxford, England, 1991.

[129] E. C. G. Stueckelberg. *Physical Review*, 42:518, 1932.

[130] J. M. Hollas. *Modern Spectroscopy*. John Wiley & Sons Ltd., Chichester, England, 3rd edition, 1996.

[131] B. P. Straughan and S. Walker. *Spectroscopy*, volume 2. Halsted Press of John Wiley & Sons, Inc, New York, 1976.

[132] R. J. Bieniek and T. J. Streeter. *Physical Review A*, 28(6):3328, 1983.

[133] W. Magnus, F. Oberhettinger, and R. P. Soni. *Formulas and Theorems for the Special Functions of Mathematical Physics*. Springer-Verlag New York Inc, New York, 1966.

[134] D. M. Manos, J. L. Cecchi, C. W. Cheah, and H. F. Dylla. *Thin Solid Films*, 195(1-2):319, 1991.

[135] C. A. Michael and J. Howard. *Review of Scientific Instruments*, 75(10):4180, 2004.

[136] N. K. Podder, III J. A. Johnson, C. T. Raynor, S. D. Loch, C. P. Ballance, and M. S. Pindzola. *Physics of Plasma*, 11(12):5436, 2004.

VITA

Sheng Peng

Sheng Peng was born in a small town, Jianhu, in Jiangsu province of China. He attained his bachelor's degree in Applied Physics in July of 1998 from Tsinghua University in Beijing, China. His graduate program in Physics at the College of William and Mary began in August of 1999. He started his research project in July of 2000 in the Center of Plasma and Photon Processing located in the Applied Research Center beside Thomas Jefferson Lab. In 2000 he married Ping Tang, who is the mother of his beautiful daughter, Eleanor, who was born in Williamsburg, VA. He received his Master of Science degree in Physics from the College of William and Mary in December of 2000. This dissertation was defended on December 17, 2004 at the College of William and Mary. While at William and Mary, he was a member of American Physics Society and Materials Research Society.

197